AN ABSTRACT OF THE THESIS OF

Ten-Yang Yen **for the degree of** **Doctor of Philosophy** **in** **Physics**

presented on **October 6, 1992.**

Title: **Ion Sputtering from Organic Liquid Matrices Bombarded by keV Metal Ions**

Abstract approved: _____

Douglas F. Barofsky

Ion sputtering from organic liquid matrices bombarded by 7-66 keV metal ions has been systematically studied as a function of the properties of the primary ions (species, energy etc.) and of the chemical environment on the target's surface. Yields of deprotonated mononucleotides (dAMP or dGMP) from a glycerol matrix, doped with the surfactant hexadecylpyridinium acetate (HDPA), as a function of stopping power (dE/dX) can be explained by models, such as the cylindrical thermal spike model with $Y=k(dE/dX-S_0)^2$ (S_0=threshold stopping power), that predict particle ejection essentially from the surface. Moreover, yields of deprotonated dAMP or dGMP generated by bombardment with polyatomic ions (Bi_3^{+2}, Bi_2^+, Au_2^+, Au_3^+) exhibit a nonlinear enhancement over those generated by bombardment with monoatomic ions (Au^+, Bi^+). Nonlinear in this case means that the number of ions ejected by a given number of atoms colliding with a liquid matrix at essentially the same point in space and time, as is the case when the atoms are clustered into a single ion, is much greater than that produced by an equal number of atoms impacting individually on the same target at different positions and times. This enhancement can also be explained by, for example, the cylindrical thermal spike model.

Ion Sputtering from Organic Liquid Matrices Bombarded by keV Metal Ions

by

Ten-Yang Yen

A THESIS

submitted to

Oregon State University

in partial fulfillment of

the requirements for the

degree of

Doctor of Philosophy

Completed October 6, 1992

Commencement June 1993

APPROVED:

Redacted for Privacy

Professor of Department of Agricultural Chemistry in charge of major

Redacted for Privacy

Head of Department of Physics

Redacted for Privacy

Dean of Graduate School

Date thesis is presented October 6, 1992

Typed by for Ten-Yang Yen

Acknowledgement

I would like to thank my advisor, Dr. Barofsky, for directing and funding the research presented in this thesis. I would also like to thank Mrs. Lilo Barofsky for preparing the liquid metal ion emitter used in this study.

I thank Ole Jensen and James Pavlovich for careful reading and correction of this thesis.

Finally, I especially thank for my wife, Huei-Mei, for supporting me to get through the difficult time.

Table of Contents

List of Figures

List of Tables

Preface

The objectives of this dissertation study were

1) to experimentally investigate ion sputtering under a variety of bombardment conditions with 7-66 keV primary ions from liquid organic matrices having various chemical environments at their surfaces and

2) to analyze the experimental data in terms of the prevailing theories on the mechanisms that govern sputtering in general and secondary ion emission in particular.

The following results from bombarding matrices of liquid organics with keV metal ions are original:

1) quantitative determination of a disappearance or damage cross section,

2) quantitative measurement of ion yield generated by bombardment with 7-66 keV monoatomic and polyatomic ions,

3) establishment of a quadratic dependence of ion yield on the rate of energy deposition (stopping power) by both monoatomic and polyatomic ion bombardment,

4) quantitative evidence for a stopping power threshold and estimation of its order of magnitude, and

5) quantitative evidence for nonlinear collisional effects produced by bombardment with 22-66 keV polyatomic ions.

The following practical developments resulted from this dissertation study:

1) use of liquid metal ion sources in liquid matrices assisted secondary ion mass spectrometry and

2) procedure for using a surfactant to achieve femtomole detectation limits for mononucleotides in liquid matrix assisted secondary ion mass spectrometry.

Ion Sputtering from Organic Liquid Matrices Bombarded by keV Metal Ions

Chapter 1

Introduction

For the past two decades, mass spectrometry has rapidly developed and has became an important analytical technique for the analysis of biomolecules. Many researchers have contributed to the successful analytical application of mass spectrometry. This success has been dependent on a few pioneers who introduced some remarkable inventions. One of these, particle induced desorption and ionization has become an important ionization technique for the analysis of biomolecules. The parameters governing the ejection and ionization of large biomolecules will be reviewed and addressed in this chapter.

1-1. Historical background

The phenomenon of ejecting particles from the surface of a condensed phase medium (solid or liquid) under energetic particle bombardment is called sputtering. It has a long historical development starting with Thomson[1] in 1910. The ejected particles include photons, electrons, neutral atoms or molecules, and a small fraction of charged ions. These ejected particles are called *secondary particles*. The stages leading to the sputtering of secondary ions are collisions, energy partition, ionization, and ejection.

The mechanisms of secondary particle emission (particularly secondary ions) will be reviewed and discussed later. The mass spectrometric analysis of secondary ions ejected from the condensed phase of an analyte matrix under bombardment by keV particles is conventionally called *secondary ion mass spectrometry* (SIMS).

Before Herzog and Viehboeck[2] developed the fundamental basis for SIMS in 1949, there were only a few works that focused on studying the emission of secondary ions under keV particle bombardment. Some 10 years after their ground breaking efforts, considerable attention was drawn to SIMS for application in the newly emerging semiconductor industry. Intuitively, it is not surprising that atomic or small molecular ions are ejected away from the surface of metallic or semiconductor materials under keV particle bombardment. However, it is a relatively complicated problem to quantitatively predict the number of ejected secondary ions.

It is difficult to generate intact molecular ions from nonvolatile organic compounds by conventional ionization techniques, such as the electron impact ionization (EI). Therefore, the ejection of ions corresponding to large, intact, thermally labile organic molecules is one of the most surprising results to have emerged from research in particle induced desorption and ionization. The first investigation of particle induced desorption of nonvolatile biomolecules was published in 1974 by Macfarlane and co-workers[3]. They employed 100 MeV energetic ^{252}Cf nuclear fission fragments to generate secondary ions from intact amino acids. This technique is termed *plasma*

desorption mass spectrometry (PDMS). In this manuscript, intact molecular ions will usually mean protonated ions $(M+H)^+$, deprotonated ions $(M-H)^-$, cations $(M+Me)^+$, and anions $(M-Me)^-$, where M is the intact molecule of an organic analyte, H is a hydrogen atom, and Me is a metal atom.

Soon after Macfarlane's initial report, Benninghoven[4] showed that similar secondary ion spectra from amino acids could be produced by using keV Ar^+ ion bombardment under so called static conditions. The difference between dynamic-SIMS, where the primary ion current density is near 10^{-6} A/cm^2, and static-SIMS, where the primary ion current density is smaller than 10^{-8} A/cm^2, will be discussed in the following chapters. The main consideration for applying the static-SIMS technique is to limit the current intensity of incident primary particles, in order to limit destruction of the organic molecules in the solid substrate by the particle bombardment. The molecules that sit behind the topmost layer along the trajectory of incident particles are also damaged, either by direct collision with an incident particle, or by excitation induced decomposition from energy deposited indirectly during the transit of an incident particle. As a result, each incident energetic particle generates a considerable damage area where no molecules survive intact. It is essential to restrict the current intensity of primary particles in order to get enough time to collect the spectra. The limited primary particle current requires that a higher transmission mass analyzer, for instance a time-of-flight tube be employed with the static-SIMS method. Although the static-SIMS technique has numerous shortcomings in analytical applications, it well suited for

studying a monolayer or submonolayer of organic molecules adsorbed on a solid substrate since the limited primary ion current maintains a well preserved, undamaged surface.

In 1981, Barber et al.[5] invented *fast atom bombardment mass spectrometry* (FABMS) by employing a neutral beams of keV atoms in the dynamic-SIMS mode to bombard an organic analyte compound mixed with liquid glycerol. The basic mechanism for ejecting secondary ions in FABMS is no different from SIMS. The novel invention of FABMS is to introduce the analyte compound in a liquid matrix instead of directly depositing the analyte compound onto a solid substrate. The secondary ion signal from a liquid matrix lasts longer than from a solid substrate, so that FABMS can be performed with a lower transmission mass analyzer, such as a double sector mass spectrometer. This has made FABMS one of the most widespread analytical techniques in the field of mass spectrometric analysis of biomolecules. The use of neutral beams in FABMS misled some researchers into thinking that it was responsible for avoiding the charging-up problem observed in samples subjected to ion beam bombardment. However, there is also a charging-up problem when a keV neutral beam is employed to bombard a sample in a liquid matrix. The secondary ion spectra show similar results; sometimes in fact, the secondary ion intensity generated by bombardment with keV ions is even stronger than by bombardment with keV neutral beams[6]. Based on these observations, FABMS is sometimes referred as liquid-SIMS. In this paper, we will adopt the term liquid-SIMS instead of FABMS.

Today, the improvements in electronics and computer interfaces, as well as mass spectrometer ion optics, have made the analysis of biomolecules by particle induced desorption and ionization (PDMS, SIMS, liquid SIMS) common practice and, consequently there has been a rapidly increase in their use. However, ultimate success in analyzing a biomolecule is still dependent on the production of molecular ions and structurally significant fragment ions. This success is, in turn, dependent on gaining a better understanding the mechanisms of secondary ion emission .

1-2. Parameters governing secondary ion emission

From the experimental point of view, mechanistic studies of secondary ion emission are based on secondary ion yield measurements. The secondary ion yield is defined as the number of ejected secondary ions divided by the number of incident particles.

The emission of secondary ions from the surface of a target is influenced by two major factors: the primary particles and the chemical environment at the surface of target. The former entails the properties of the incident particles; the latter involves the chemical nature of the analyte, the chemical nature of the substrate or matrix that supports the analyte, and the procedure of sample preparation. Schronk et al.[7], and Eicke et al.[41] showed that the appearance of secondary ion spectra and intensity of secondary ion species are strongly dependent on the procedure of sample preparation.

In general, there are five different methods of sample preparation: direct deposition with a microsyringe, electrospraying[8], spin casting[9], ultra high vacuum (UHV) molecular beam deposition[10], and solution in a liquid matrix method[5]. The first three methods are based on the same initial preparation stage, viz. preparing the sample in a liquid solution and applying to a solid substrate. The characteristics of these methods have been reviewed by Sundqvist[11]. We will not go in detail, but it is worthwhile to point out that the critical factor for the successful analysis of biomolecules is to choose the sample backing substrate properly. Nafion[12], mylar film[13], and nitrocellulose film[14] have been reported as good backing substrates for the analysis of large biomolecules. UHV molecular beam deposition is a high purity sample preparation method. It has a disadvantage in that only relatively small molecules, such as amino acids, can be evaporated without thermal degradation. This method is particularly well suited for studying physical or chemical adsorption between the analyte molecule and the solid substrate[15,16]. Over all, the most widely employed method of sample preparation for analytical applications of biomolecules is to mix analyte with a liquid matrix. All the liquid matrices have some basic properties in common: they must have very low vapor pressure and they must be water soluble. Glycerol is one of the most effective matrix liquids. The physical properties of several useful matrices have been reviewed by Cook et al.[17].

In order to understand the mechanism of secondary ion emission, the systematic measurement of secondary ion yield is necessary. Ideally, this requires that one

parameter at a time be changed while keeping all the others unchanged. The properties of primary particles can be separated into the following parameters: energy, charge state, mass (including monoatomic, and polyatomic particles), and incident angle relative to the target normal. To separate the effects of these parameters from the influence of the chemical environment at the surface of target is difficult due to the complexity of analyte-matrix interactions. Our quantitative understanding of these interactions is very limited.

1-3. Influence of primary particles on secondary ion emission

Many experiments have been carried out with incident MeV ions generated by an accelerator to study the influence of primary particles on secondary ion emission. Della-Negra et al.[18] reported that the yield of deprotonated phenylalanine $(M-H)^-$ increases with primary ion velocity in the range of 0.4 cm/ns (roughly double the Bohr velocity) to 1 cm/ns followed by a decrease in the higher projectile velocity region. But velocity is not the single best parameter for studying the secondary ion yield; the rate at which energy is deposited from projectile to target per unit distance traveled, the stopping power dE/dX, is probably the single best meaningful parameter. It is plausible that the secondary ion yield is connected with the stopping power based on the kinetic energy transferred from the incident particle to the condensed phase target. The calculation of stopping power from first principles is complicated; it will be taken up in the next chapter. Simply speaking, the stopping power can be divided into two

regimes: the nuclear stopping and the electronic stopping power. For relatively slow keV primary particles, nuclear stopping power is the dominant process; for fast MeV primary particles, the electronic stopping is the dominant process. The division between slow and fast is approximately the Bohr velocity, 0.22 cm/ns. Large numbers of measurements of organic secondary ion yield as a function of stopping power have been published[19-24a]. Håkansson et al.[20] showed that the molecular ion yield $(M)^+$ of ergosterol electrosprayed onto an Al backing is proportional to the square of the electronic stopping power under a variety of MeV ion bombardment experiments. Albers et al.[21] reported that the yield of protonated valine $(M+H)^+$ electrosprayed onto Al foils is roughly proportional to the square of the electronic stopping power when the velocity of primary O or S ions are more than 0.2 cm/ns, and is proportional to nuclear stopping power when the velocity of primary O or S ions is below 0.2 cm/ns. Hunt et al.[22] found that the deprotonated ion yield $(M-H)^-$ of valine electrosprayed onto a stainless steel backing or onto an aluminized Mylar film is proportional to the square of the electronic stopping power under 0.4 to 3.5 MeV Xe^+, Kr^+, and Ar^+ ion bombardment. However, in their observation, the deprotonated ion yield of valine under bombardment with ions having hundreds keV is still dependent on the electronic stopping power; that is different from Albers's observation. Brandl et al.[23] studied valine deposited by vacuum evaporation on an Au-Mylar foil under bombardment with MeV ions; they showed that the yields of protonated valine $(M+H)^+$ and of deprotonated valine $(M-H)^-$ are nearly proportional to the square of the electronic stopping power less a certain threshold value. Not all the molecular ion yields of biomolecules are governed

by such a simple quadratic dependence on the electronic stopping power under MeV ion bombardment; the ion yield of large molecules, such as bovine insulin, has been shown[24] to be directly proportional to the electronic stopping power in the higher electronic excitation region. In a recent paper, Barros et al.[24a] also observed deviation from a square dependence; they found that the yields of protonated phenylalanine and of deprotonated phenylalanine evaporated onto aluminized carbon film shows a cubic dependence on the electronic stopping power.

So far, we have reviewed experimental observations of secondary ion yield from organic solids as a function of stopping power, mainly the electronic stopping power, under fast ion bombardment (hundreds of keV to tens of MeV). Thousands of experiments have been carried out with slow keV particle bombardment for analytical applications. However, very few systematic studies of secondary ion yield measurements have been done. Ens[25] reported that the yields of protonated alanine $(M+H)^+$ bombarded by 1 to 14 keV Li^+, Na^+, K^+, and Cs^+ is directly related to the nuclear stopping power of these primary ions. Blain et al.[26] showed that the yield of deprotonated phenylalanine $(M-H)^-$ is dependent on the square of the velocity of keV Au^+ primary ions.

Evidence for the relationship between stopping power and the mechanism of secondary ion emission comes from the neutral yield of sputtered polycrystalline metals and semiconductors under bombardment with keV primary ions. It is found that the

neutral yield of analyte is linearly proportional to the nuclear stopping power of the incident projectile. A theoretical model has been derived by Peter Sigmund[27] and is well known as the "atomic collision cascade theory"; so far, it is still the only model that can quantitatively predict the sputtering neutral yield generated from polycrystalline metals and semiconductors by bombardment with keV incident ions. Neutral sputtering yield measurements from organic molecules is not an easy experiment; as a result, very little data is available. Experiments have been done by measuring the total sputtering yield form an organic liquid[28,29] (glycerol) and an organic solid[30] (leucine). The former were performed with slow keV primary ions, and the latter which showed the yield as being proportional to the cube of the electronic stopping power, were produced with MeV primary ions. Johnson et al.[31] have proposed a "pressure pulse model" to interpret these results from MeV particle bombardment, but there is no other data to support this model.

The charge state of the incident particles is another important parameter in the mechanism of secondary ion emission under fast MeV ion bombardment. According to theory, the electronic stopping power of high velocity heavy ions is nearly proportional to the square of the atomic number of the incident particles. This offers another means for exploiting the relationship between secondary ion yield and the electronic stopping power of an incident ion. The dependence of the secondary ion yield on the charge state of MeV primary particles has been reported by Della-Negra et al.[32], and by Brunelle et al.[33]. The charge state dependence on the secondary ion yield apparently

varies with the identity of secondary ions. We will not dwell on this effect in this paper because we are mainly studying ion sputtering caused by slow keV incident particles. As a result, the effect of charge state related to the electronic stopping power is not as important as in the case of nuclear stopping power.

From experimental observations[21,23,25], the secondary molecular ion yield of an organic solid varies with the incident monoatomic particle species. This is no surprise, since the stopping power also varies with the incident particle species. The secondary ion yield as a function of stopping power has been reviewed previously, and some of the general trend is understood. An abnormal phenomenon, however, is that the number of secondary atomic or molecular ions generated by polyatomic ion bombardment is greatly enhanced over that generated by monoatomic ion bombardment. Johar et al.[34] reported that the neutral yields of Au, Ag, and Pt sputtered with 10-250 keV polyatomic ions of P, As, Sb, and Bi are considerably greater than the yields predicted by "atomic collision cascade theory"[27]. Salehpour et al.[35] showed that the deprotonated ion $(M-H)^-$ yield of valine produced by bombardment with 600 keV - 3.7 MeV polyatomic C_2^+, O_2^+, CO_2^+, CH^+, CH_3^+, CF^+, CF_3^+, $C_3F_5^+$, and $C_4F_7^+$ is enhanced in a nonlinear fashion over that produced by bombardment with monoatomic C^+ and O^+ ions. Schweikert et al.[36] and Brunelle et al.[37] found that the yield of deprotonated phenylalanine sputtered with tens of keV CsI cluster ions and with polyatomic Au ions shows a similar nonlinear effect.

The last property of primary particles that is important for sputtering is the angle between the incident particle and the normal of the sample surface. The yield of protonated phenylalanine $(M+H)^+$ as a function of incident angle has been reported by Della-Negra et al.[38] to obeyed the inverse of cosine rule. However, experimental results for the electronic sputtering yield of condensed O^2 bombarded by MeV He ions was found to have a $(\text{cosine})^{-1.6}$ angular dependence[39].

1-4. Influence of chemical environment at the surface of the target on secondary ion emission

From secondary ion spectra, it has been shown that species and charge states of the emitted secondary ions are strongly dependent on the chemical environment at the surface of the analyte matrix[7,41]. As we mentioned before, this chemical environment depends strongly on the procedure of sample preparation.

It is very difficult to classify the parameters involved in describing the chemical nature of an analyte and its interaction with the substrate or the matrix due to the number and complexity of possible interactions. In the case of UHV molecular beam sample deposition of a submonolayer or monolayer of amino acid onto a very clean metal substrate under bombardment with keV Ar^+ ions, it has been shown that the protonated and deprotonated ion yield of amino acid is related to the binding strength between analyte molecules and different substrates, such as Au, Ag, Cu, and Ni.

However, these experiments with UHV molecular beam depositions are the exception when it comes to interpreting the results; it is not as simple for the other sample preparation methods.

Eicke et al.[40,41] reported that, when amino acid solutions are directly deposited onto a solid substrate, secondary molecular ion emission under 3 keV Ar^+ bombardment is strongly influenced by the sample preparation condition, especially by additives, and by substrates. . They found that by adding an appropriate acid (1.0M HCl or 0.005M HI); the yield of protonated leucine or cytosine $(M+H)^+$ is increased; on the other hand, the yield of deprotonated ion $(M-H)^-$ is decreased. Roepstorff et al.[42] showed that, under MeV ion bombardment, the secondary ion yield of porcine insulin (MW=5778) adsorbed onto a nitrocellulose film is about twice as strong as that obtained when the insulin is electrosprayed onto an aluminum backing film. Moreover, their studies of molecular ion yield as a function of the electronic stopping power of different primary ions clearly indicate that the molecular ion yield of insulin adsorbed on a nitrocellulose film varies slower with electronic stopping power than the molecular ion yield of insulin electrosprayed onto an aluminum film. Comparison of some peptide samples and their substrates relative to secondary molecular ion yield resulting from bombardment with 12keV Ar^+ ions was reported by Leyen et al.[43]. They observed that the secondary molecular ion yield of peptides adsorbed on a Au, or a Ag substrate is stronger than when the analyte is adsorbed on another substrate, such as Cu, nitrocellulose, or glycerol.

In practice, the preparation of samples mixed with liquid matrices is the most widely used method for the analysis of biomolecules. One reason for the popularity of samples prepared with liquid matrices over those with solid substrates is that the molecular ion's signal in the case of a liquid matrix usually lasts for tens of minutes without significant reduction under high current bombardment. Due to the behavior of organic compounds in a solvent, such as glycerol, understanding the mechanism of ion formation in a liquid matrix under particle bombardment poses a complex problem. It is important to ask how and where the useful molecular ions are formed.

From the sputtering theory, we know that the atoms and molecules near the surface have the greatest likelihood of being ejected intact out of the surface during energetic particle bombardment. The maximum effective depth from which secondary ions can be ejected out of a surface is a few tens of Å for keV incident particles[44] and about 300 Å for 45.5 MeV incident ^{127}I ions[45]; therefore, the composition at the surface of a target plays a strong role in determining the kind of secondary ions that can be ejected under bombardment with energetic particles. Ion formation at the surface of the liquid matrix is mostly controlled by solution chemistry[46]. Whether ions are formed in solution or in the gas phase is still debated, but there are many results that support "the precursor model"[47] as the dominant process if not the exclusive process. This model proposes that the molecular ions are preformed at the surface of target and are ejected as secondary ions after particle bombardment. A comparison of secondary ion spectra generated by fast MeV particle bombardment with those generated by slow keV particle

bombardment shows very little difference except the intensity of the secondary ions is higher with Mev particles bombardment[25]. This result also supports "the precursor model".

It appears, therefore, that the critical point in generating useful ions from a liquid matrix by particle bombardment is that the ions be preformed and reside at the surface. Among the many parameters of solution chemistry, it has been found that the surface activity of an analyte is one of the most important because it relates the total amount of useful analyte available for ejection out of the surface. Ligon and Dorn[48] have reported a striking 1000-fold enhancement in the deprotonated ion intensity of Adenosine triphosphate (ATP) by adding a surfactant (0.001M hexadecylpyridinium acetate) to increase the surface activity of ATP in a glycerol matrix.

In summary, the secondary emission of a molecular ion is strongly dependent on the energy deposited from an incident particle and on the chemical environment at the surface of the target. There are numerous experimental observations that show how the secondary molecular ion yields of organic molecules vary with keV or MeV incident particles as well as with different solid substrates. However, the influence of primary particles on secondary ion emission of organic compounds from liquid matrices, particularly glycerol, has not been addressed. We have investigated a system[48] that allows us to have some degree of control over the surface concentration of analyte in a liquid matrix. This is especially important for studies of this sort, because it provides

a system that avoids some of complicated interactions between analyte (solute) and matrix (solvent). Moreover, this system allows us to study the role of primary particles in the mechanism of secondary ion emission with a reasonably defined surface condition; this is important since the mechanism of secondary ion emission from the surface of a liquid matrix is different than that from the bulk of a liquid matrix.

Chapter 2

Theoretical

2-1. Stopping power

Stopping power (***dE/dX***) is the rate at which a primary particle deposits its kinetic energy in the target medium per unit length of travel in that medium. Disregarding the details of the secondary ion emission processes, secondary particles, including ions, are ejected from the surface of a target medium into vacuum as an ultimate consequence of a primary particle's kinetic energy being dissipated in that medium. It is, therefore, important to understand the energy deposition processes of particle bombardment.

Consider a simple physical system in which an incident ion (mass M_1, atomic number Z_1) with a velocity v collides with an atom (mass M_2, atomic number Z_2) in a monoatomically composed target. The kinetic energy of the incoming ion is ultimately converted into kinetic energy of the target atoms either through elastic collisions (nuclear stopping) or through electronic excitations (electronic stopping). If the incoming ion passes very close to the nucleus of a target atom, then the interactive force between the incoming ion and the target atom is Coulombic. The scattering process is described by the Rutherford formula. When the incident ion passes far away from the target atom,

then the interaction is through a screened Coulombic force. For a fast ion interacting with a condensed state target, kinetic energy transformed via electronic excitation is dominant over that transformed via elastic collisions. However, when a slow ion interacts with a condensed state target, the multiple processes of ion-atom collisions become most important. According to Lindhard's calculation[49], the electronic stopping is dominant mode of energy deposition for $v > Z_1^{1.5} V_B$ whereas nuclear stopping is dominant mode of energy deposition for $v < 0.1\ Z_1^{1.5} V_B$ where v is the velocity of incident primary ion and V_B, the Bohr velocity, is equal to 0.218 cm/ns.

2-1A. Nuclear stopping power

Formulas for the nuclear stopping power have been derived by Lindhard et al.[50], Wilson et al.[51], and Ziegler[52]. All of the expressions incorporate the classical scattering model to account for the exchange of energy in ion-atom collisions, and all of them handle electronic excitation as an independent parameter. The assumption is that there is only a minor correlation between nuclear stopping and electronic stopping. Generally speaking, nuclear stopping refers to the process of transferring kinetic energy from the incident ion to the target atom. It mainly depends on the masses, atomic numbers of the incoming ion and the target atom as well as the initial energy of the incoming ion. As the incident ion passes through the target and loses part of its energy, the target atoms that are near the path of the incident ion absorb some its energy and may recoil from their position.

For a two body scattering process, the incident ion (mass M_1, atomic number Z_1) with a velocity $\mathbf{v}_0$ and an initial energy E_0 in the tens of keV range collides with a stationary target atom (mass M_2, Atomic number Z_2). We can change the laboratory frame into the simple center-of-mass system depicted in Figure 2-1. Now the incoming ion with a velocity $\mathbf{v}_0$-$\mathbf{v}_c$ collides with a moving target atom with a velocity $\mathbf{v}_c$ in the opposite direction. Relative to collision path, the incident ion and the target atom are scattered out into angles θ and ϕ respectively after the collision. P, the impact parameter is the vertical distance between the incident ion and the target atom prior to collision. This is a typical two particle collision problem in classical dynamics; detailed treatments can be found in many textbooks[53]. The result is that the kinetic energy transferred from the incident ion to the target atom, T, is given by

$$T = \frac{4M_1M_2}{(M_1+M_2)^2} E_0 \sin^2\frac{\theta}{2} \tag{2-1}$$

E_0 is the initial energy of the incident ion in the laboratory frame ($E_0 = (1/2)\, M_1\mathbf{v}_0^2$) and θ is the scattering angle given by

$$\theta = \pi - 2\int_{r_{min}}^{\infty} \frac{Pdr}{r^2\left[1-\frac{V(r)}{E_c}-\frac{P^2}{r^2}\right]^{\frac{1}{2}}} \tag{2-2}$$

where $V(r)$ is the central force potential, E_c is the energy of the particle in the center-of-mass system ($E_c=[M_1M_2/2(M_1+M_2)]\mathbf{v}_0^2$), and r_{min} is the turning point (the closest

Figure 2-1: Two body scattering processes in center-of-mass system

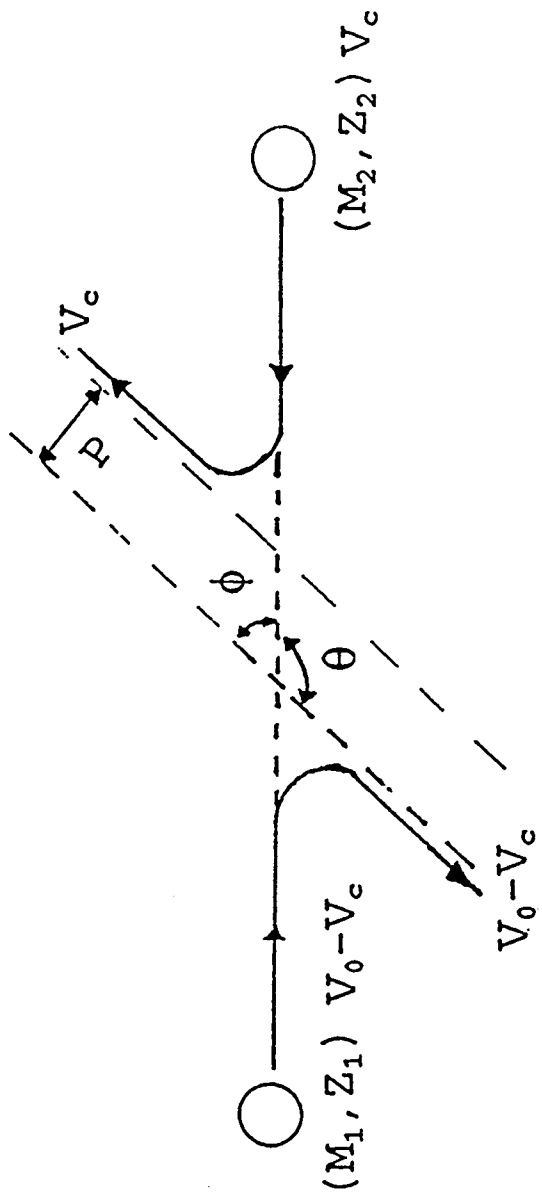

distance between the incoming ion and the target atom).

The differential cross section $\sigma(\theta)$ is defined by

$$\sigma(\theta) = \frac{-P}{\sin\theta}\frac{dP}{d\theta} \tag{2-3}$$

The nuclear stopping power $(dE/dX)_n$ can be expressed as

$$\left(\frac{dE}{dX}\right)_n = N\int_0^{T_m} T\,\sigma(T)\,dT \tag{2-4}$$

where $T_m = [4M_1M_2/(M_1+M_2)^2]E_0 = \alpha E_0$ and $\sigma(T)$[51], the energy transfer differential cross section, is given by

$$\sigma(T) = \frac{4\pi}{\alpha E_0}\sigma(\theta) \tag{2-5}$$

$V(r)$ needs to be determined before we can actually calculate the nuclear stopping power $(dE/dX)_n$. If $V(r)$ is a pure Coulombic interactive force, $V(r) = (Z_1Z_2/r)e^2$, then the scattering process is given by the Rutherford formula. As we mentioned earlier, the interactive force is a Coulombic force when the velocity of the incoming ion is fast. In this case, the nuclear stopping power is relatively small compared to the electronic stopping power. However, as the velocity decreases relative to $(0.1 \bullet Z_1 \bullet V_B)$, the nuclear stopping power becomes increasingly important, and the interactive force is given by a screening Coulombic expression.

For the 5-70 keV incident ions employed in our studies, the nuclear stopping power is dominant in the energy deposition processes. In general, the screening Coulombic potential is given by

$$V(r) = \frac{Z_1 Z_2}{r} e^2 \ \phi(r) \tag{2-6}$$

where $\phi(r)$ is the screening Coulombic function. In order to evaluate the nuclear stopping power, Lindhard et al.[50] have used a Thomas-Fermi treatment to get a power form of $\phi(r)$. In short, they solve for the nuclear stopping power $(dE/dX)_n$ by introducing two dimensionless terms: the reduced energy ε and the reduced nuclear stopping cross section $s_n(\varepsilon)$:

$$s_n(\varepsilon) = \frac{\varepsilon}{E_0 \pi a^2 \alpha N} \left(\frac{dE}{dX}\right)_n \tag{2-7}$$

where the screening length, $a = 0.53*0.88853*(Z_1^{2/3}+Z_2^{2/3})^{-1/2}$ Å , N is the number density of target atoms expressed in atoms/cm^3, and $\varepsilon = (aM_2E_0)/[(M_1+M_2)Z_1Z_2e^2]$. Once $s_n(\varepsilon)$ is determined, then the stopping power can be calculated from equation 7.

Solving for the reduced nuclear stopping cross section $s_n(\varepsilon)$ from first principles is not straightforward and will not be treated here in detail. Instead, we adopt the numerical solution for $s_n(\varepsilon)$ given by Wilson et al.[51] (the rationale for this will be given in chapter 5).

$$s_n(\varepsilon) = \frac{\ln(1+\varepsilon)}{2(\varepsilon + A\varepsilon^B)} \tag{2-8}$$

For the Thomas-Fermi screening Coulombic potential, A is equal to 0.10396, and B is equal to 0.50793. There is an important continuity requirement for $s_n(\varepsilon)$; namely, for $\varepsilon >> 1$, the Coulombic scattering form of $s_n(\varepsilon)$ must approach $(ln\varepsilon)/2\varepsilon$.

In practical calculations[54], the reduced energy ε can be calculated from:

$$\varepsilon = 32.5 \frac{M_2}{Z_1 Z_2 (M_1+M_2)(Z_1^{\frac{2}{3}}+Z_2^{\frac{2}{3}})^{\frac{1}{2}}} E_0 \tag{2-9}$$

where E_0 is the initial energy of the incident ions expressed in keV. Furthermore, if we define the nuclear stopping cross section S_n as

$$S_n = \frac{1}{N}\left(\frac{dE}{dX}\right)_n \tag{2-10}$$

we can get the following practical formulas for S_n:

$$S_n = 8.4746 \frac{Z_1 Z_2}{(Z_1^{\frac{2}{3}}+Z_2^{\frac{2}{3}})^{\frac{1}{2}}} \frac{M_1}{M_1+M_2} s_n(\varepsilon) \left[\frac{eV*cm^2}{10^{15} atom}\right], \tag{2-11}$$

$$S_n = \frac{8.4746}{1.66\ M_2} \frac{Z_1 Z_2}{(Z_1^{\frac{2}{3}}+Z_2^{\frac{2}{3}})^{\frac{1}{2}}} \frac{M_1}{M_1+M_2} s_n(\varepsilon) \left[\frac{MeV*cm^2}{mg}\right]. \tag{2-12}$$

The equation 2-12 is obtained from equation 2-11 by a simple transformation of units.

2-1B. Electronic stopping power

Calculation of electronic stopping power is based on the assumption that the interaction of the incident ion and the target atom can be treated as a particle interacting with a free electron gas of a given average density. The calculation is more complicated than the calculation of the nuclear stopping power because the electronic stopping power varies with the velocity of the incident ion. Ziegler[52] has reviewed the general concepts as well as the specific calculation of the electronic stopping power for the incident ions with an energy to mass ratio smaller than 10 MeV/amu. The velocity of the incident ions are smaller than $0.218 * Z_1^{2/3}$ cm/ns in the experiments described in this thesis. For this velocity regime, Lindhard[55] has shown that the electronic stopping cross section S_e per atom can be expressed as

$$S_e = 8\pi Z_1^{\frac{1}{6}} e^2 a \frac{Z_1 Z_2}{Z} \frac{V}{V_B} \qquad (2\text{-}13)$$

where $Z = (Z_1^{2/3} + Z_2^{2/3})^{3/2}$, $V_B = 0.218$ (cm/ns), and a is given in the footnote of equation 2-7.

The electronic stopping cross section S_e can be further converted to the following practical formula:

$$S_e = \frac{19.181}{1.66}\frac{Z_1^{\frac{1}{6}} Z_1 Z_2}{M_2 \; Z}\frac{V}{V_B}\left[\frac{MeV*cm^2}{mg}\right]. \qquad (2\text{-}14)$$

2-1C. Total stopping power of a multicomponent target

From equations 2-11, 2-12, and 2-14, we can write the total stopping power S as equal to the sum of the nuclear stopping cross section and the electronic stopping cross section:

$$S = S_n + S_e \qquad (2\text{-}15)$$

Equation 2-15 is the total stopping cross section of a single component target. For a complex target of organic compounds, we need to apply Bragg's law[56] to calculate the total stopping cross section S_T:

$$S_T = \sum_i N_i S_i \qquad (2\text{-}16)$$

where N_i is the relative abundance of the i'th component in the compound and S_i is the total stopping cross section of the i'th component in the compound.

Bragg's law does not take into account the effects of chemical bonding state or of physical state (solid, liquid or gas). However, Thwaites[57] reviewed several experimental observations and he found that the experimental data show 5-10% deviation from Bragg's law at most. Based on this evidence, we have employed Bragg's

law to directly calculate the stopping power of the compounds that we used in our studies. We have calculated the nuclear stopping cross section, the electronic stopping cross section, and the total stopping cross section of glycerol ($C_3H_8O_3$), deoxyadenosine monophosphate (dAMP, $C_{10}H_{14}O_6N_5P$), and hexadecylpyridinium acetate (surfactant, $C_{23}H_{41}O_2N$) for different species of primary ions; our results are presented in Figures 2-2, 2-3, and 2-4 respectively. The energy range of the primary ions in all of the figures is from 1 to 1000 keV. We are particularly interested in the region from 5 to 70 keV, which corresponds to the energy range of our liquid metal primary ion gun. In this region, we find that the electronic stopping cross section contributes less than 20% to the total stopping cross section for all the compounds. It is interesting to note that the stopping cross section for glycerol and the surfactant are essentially identical and they are significantly larger than the stopping cross section of dAMP.

2-2. Secondary ion emission

"The precursor model" of secondary ion formation[47] is based on collective observations from SIMS, liquid-SIMS, PDMS, and *laser desorption mass spectrometry*[58] (LDMS). This model proposes that the secondary ions are preformed, that is, formed before they are ejected by energetic particle (keV or MeV) or photon bombardment. This is a plausible assumption, because SIMS, liquid-SIMS, PDMS, and LDMS generate very similar secondary ion spectra. The fundamental hypotheses in "the precursor model" are: 1) ions are formed at or near the surface of the target before particle

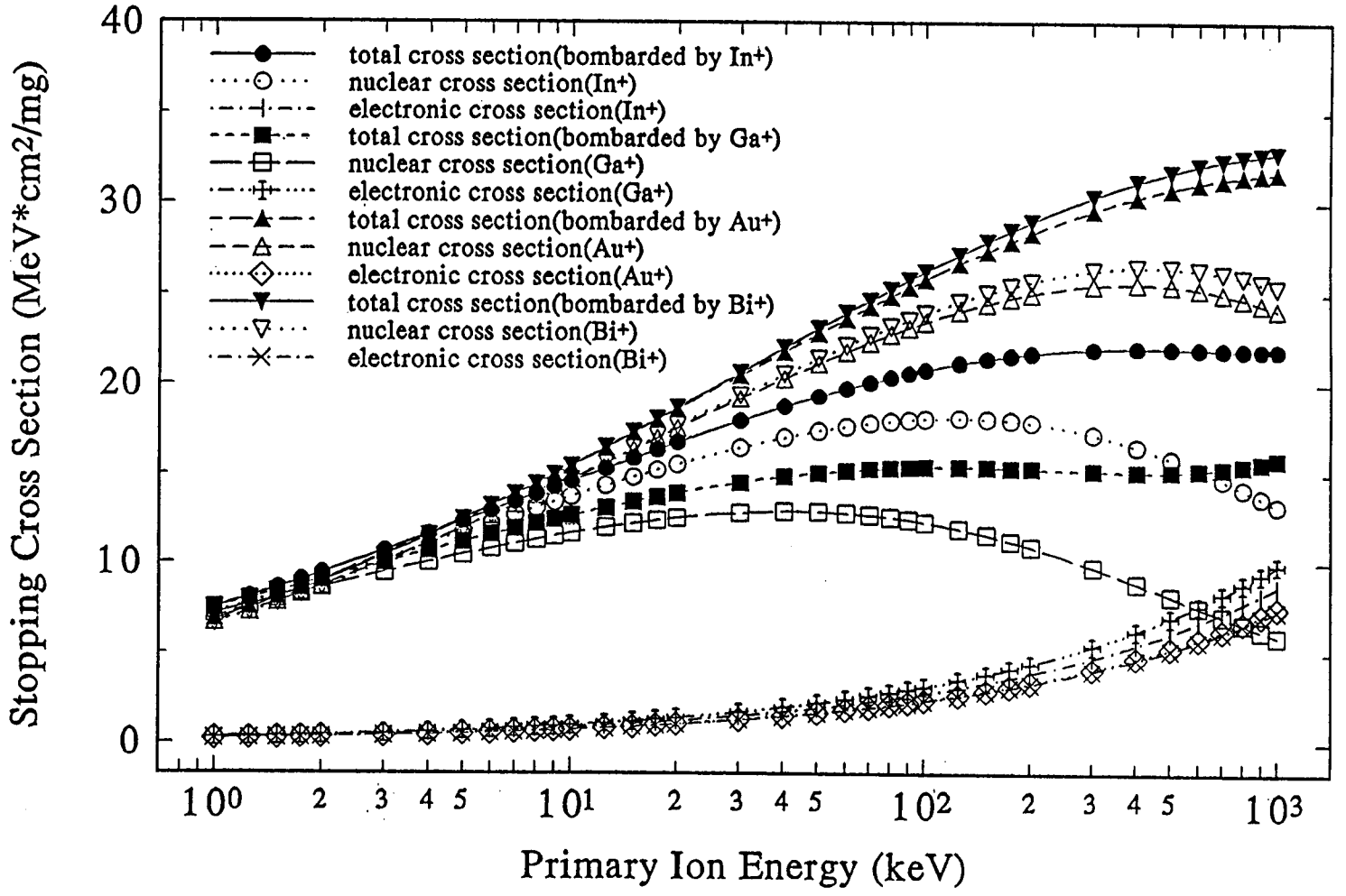

Figure 2-2: Stopping cross section of glycerol

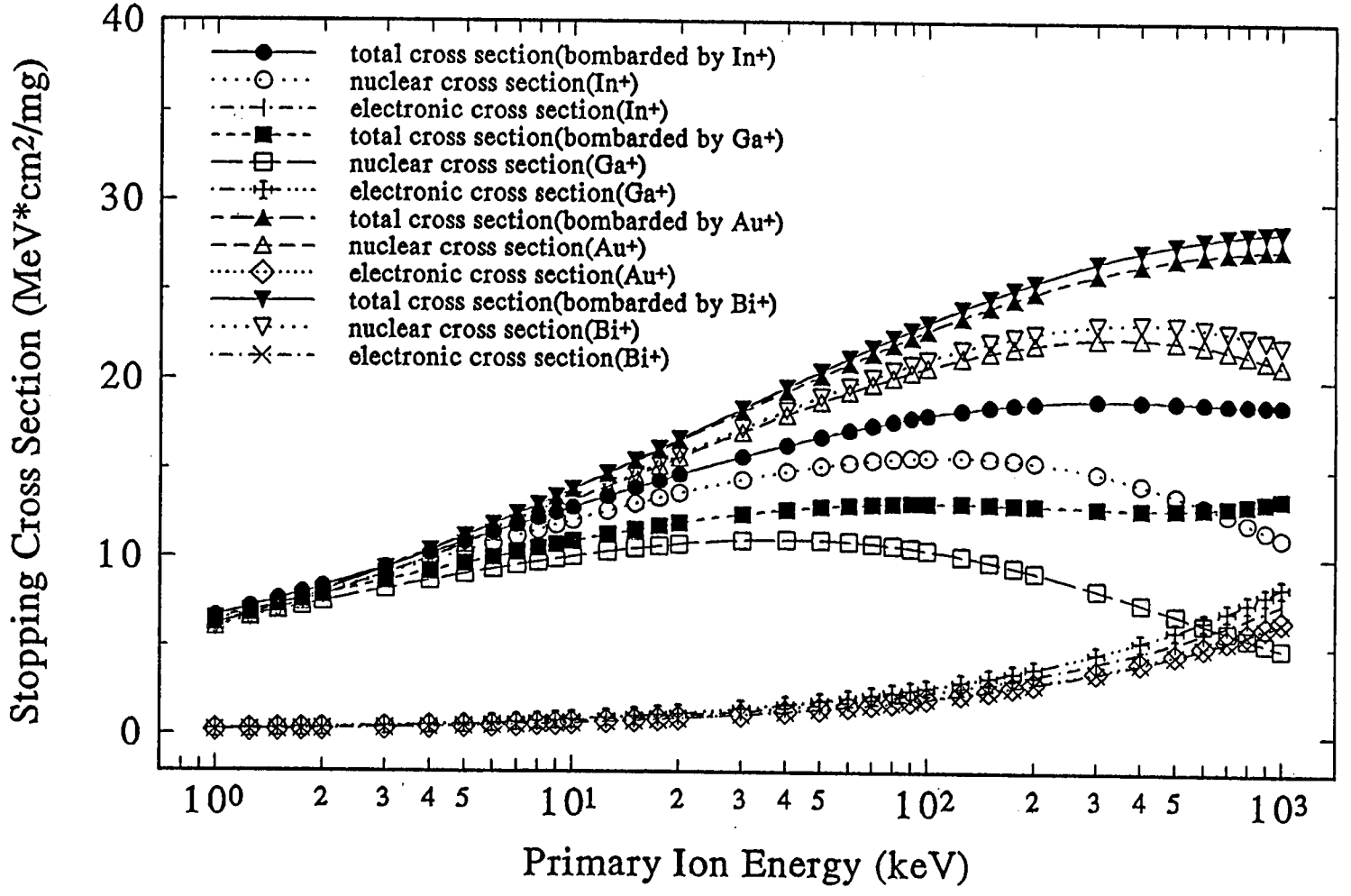

Figure 2-3: Stopping cross section of dAMP

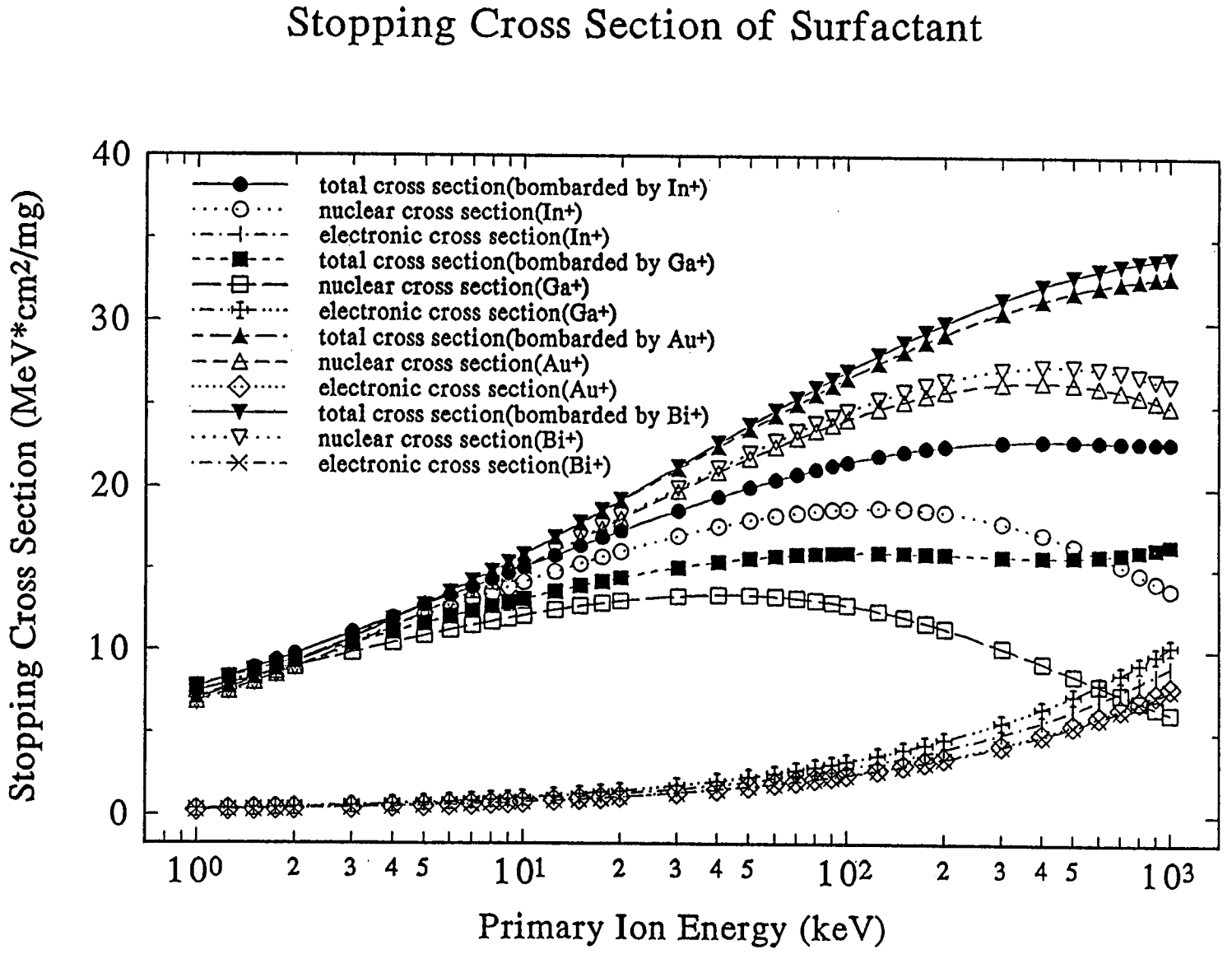

Figure 2-4: Stopping cross section of surfactant (HDPA)

bombardment, 2) kinetic energy is transferred quickly from the incident particle to the ions existing at the surface in order to avoid fragmentation, 3) the average charge at the surface tends to be conserved, and 4) there exists a certain area where the energy transferred is so high that only fragmented ions are ejected.

As stated above, "the precursor model" accounts only qualitatively for secondary ion emission; it does not predict the number of secondary ions emitted in a given experimental situation. Nonetheless, this model contains the important concept that it is possible to explain the mechanism of secondary ion emission from organic compounds on the basis of an energizing mechanism instigated by particle bombardment and, furthermore, that the chemical environment at the surface of the sample is independent of the energizing mechanism and can be treated as a complex surface binding state.

As we discussed previously, the energizing mechanism under keV and MeV particle bombardment can be divided into two processes: elastic collisions (nuclear stopping) and electronic excitation (electronic stopping). Nuclear stopping is dominant in the energy regime of low keV incident ions while electronic stopping is dominant in the energy regime of high MeV incident ions. When MeV incident ions interact with a condensed state target, about half of the net energy deposited from the incident ion goes into electron-hole pair generation and the other half goes into vibrational and phonon excitations[59] (heat). In contrast, the energy transferred from the low keV primary ions to a condensed state target is mainly deposited elastically into atomic or

molecular motions. It is interesting that, despite strikingly different pathways for energy deposition, both MeV ion and keV ion bombardment generate similar secondary ion spectra from the organic compounds. In describing their pressure pulse model, Johnson et al.[31] pointed out that the energy deposition either by elastic collisions or by electronic excitations, can generate an energized volume along the projectile track from which the atoms or molecules located therein can be ejected into vacuum. Elastic collisions can directly produce the necessary atomic or molecular motions, but electronic excitations can not directly generate such motions. Several mechanisms, e.g. repulsive decay of excited and ionized molecules[60], Coulombic repulsion[61] between ionized atoms, and molecular expansion from the vibrational excitation produced by the secondary electrons[62], have been proposed to explain how the electronic energy is transferred into atomic or molecular motions in this energized volume. The physical interpretation of secondary ion emission from MeV particle bombardment is different than that from low keV particle bombardment. We will only focus on the energizing mechanism of low keV primary particles.

2-2A. Atomic collision cascades and thermal spikes

The energizing mechanism of elastic collisions caused by keV incident particles can be separated into two regimes: low density energy deposition *(linear cascade)*, and the high density energy deposition *(spike* or *dense cascade*). The theory of neutral sputtering yield in the linear cascade regime has been developed by Sigmund[27] as the

well known "atomic collision cascade theory". The basic argument of this theory is that the density of the collisions is low enough to allow each collision to be described by a binary event that follows the Boltzmann transport equation. The sputtering neutral yield is determined by 1) converting the energy deposition of the incident particle into a number of low energy recoil atoms, 2) determining how many atoms come to the surface, and 3) selecting those that have enough energy to overcome the surface binding force. Over all, the sputtering yield Y is given by

$$Y = \Lambda F_D \quad ; \tag{2-17}$$

$$F_D = \beta \left(\frac{dE}{dX}\right)_n \quad ; \tag{2-18}$$

$$\Lambda = \frac{\Gamma_m}{8(1-2m)} \frac{1}{NC_m U^{1-2m}} \quad . \tag{2-19}$$

The stopping power at the surface of the target, F_D, differs from the bulk stopping power, $(dE/dX)_n$, by a fractional factor β, which according to Sigmund[27] should be a complex function of the mass ratio M_1/M_2, incident angle θ, and energy of the primary ion (E_0), that approaches unity as the primary particle penetrate from the surface region into bulk. Λ is a material parameter, U is the planar surface potential; N is the number density of target material (atoms/cm^3). Γ_m and C_m are constants that depend on a cross

section parameter m that is in turn determined by the target material and the energy of the incident particle[27].

The successful prediction of sputtering yield from "the atomic collision cascade theory" strongly depends on how accurately the nuclear stopping power is known. Experimental values for the sputtering yield of copper bombarded by krypton ions given in reference 63 show that the predicted yield resulting from Wilson's Kr-C nuclear stopping power[51] is most accurate in the low keV region, but that the nuclear stopping power obtained from a Thomas-Fermi potential (equation 2-8) is most accurate at the high keV region. The electronic stopping power is subject to considerable error in the keV energy region; however, electronic stopping contributes less than 20% to the total stopping power in this energy range so the error contribution due to electronic stopping is relatively small. "The atomic collision cascade theory" has successfully predicted the neutral sputtering yield from polycrystalline metal and semiconductor bombarded by low keV primary ion. However it does not apply to the sputtering yield generated by heavy ions or by molecular ion bombardment with a heavy target in the 10 keV to 1 MeV energy region. The abnormally high yields obtained in these cases deviate greatly from the predictions of "the atomic collision cascade theory" and are proposed to be due to spike effects[44,63,64].

A spike is a local volume where all the atoms or molecules are set in motion essentially instantly by the high rate of energy deposition. Since the collisions in a

spike are so violent, the Boltzmann transport theory can not be applied to describe the individual collision events as in the case of linear cascades. It is generally accepted that the mechanism of spike phenomena are adequately accounted for by "the shockwave model"[65,66] and "the thermal spike model"[67,68,69,70]. Since in this dissertation we are going to report an ion sputtering from liquid matrices and this seems best explained by "the thermal spike model", we will limit most of our discussion to "the thermal spike model".

"The thermal spike model" allow us to directly calculate the sputtering yield from three parameters: the energy deposition, the target material's thermal conductivity, and the surface sublimation energy. The main assumptions of this model are that the heat conduction equation (equation 2-20) can be employed to describe energy partitioning and time evolution in the spike volume and that the heat source is a function of the energy deposition (the stopping power):

$$\nabla\kappa \, \nabla T(x,t) = C \frac{\partial T(x,t)}{\partial t} \qquad (2\text{-}20)$$

where $T(x,t)$ is the spike temperature distribution at position x and time t; κ is the thermal conductivity of the target, and C is the heat capacity per unit volume of the target.

The physical basis for using the equation of heat conduction rests on the idea that when a sufficiently large amount of energy is deposited into a small volume, the atoms or molecules located in this volume are all set into motion before any significant energy dissipation has occurred. After a certain time ($\sim 10^{-11}$s)[63], the kinetic energy and the electronic excitation energy of those moving particles may approach a Maxwell-Boltzmann distribution. This means that a localized temperature equilibrium condition exists in the spike volume and that the heat conduction equation can be employed to calculate the temperature distribution of the spike volume.

For a cylindrical spike, the heat source of the spike at $t=0$ is equal to $\varepsilon\delta^2(x)$; where ε is the energy deposition per unit length, $\delta^2(x)$ is a two dimensional delta function. Vineyard[67] solved the heat equation using $\varepsilon\delta^2(x)$ as the heat source; he obtained the following solution for the temperature distribution $T(x,t)$:

$$T(x,t) = \frac{\varepsilon}{4\pi\kappa t} e^{\frac{-Cx^2}{4\kappa t}} \qquad (2\text{-}21)$$

where κ and C are assumed to be independent of the temperature and t is time. Vineyard further proposed that the sputtering yield can be calculated from a activated rate process. This activated rate process is governed by the rate of the target atoms flowing into the new lattice sites. If the flow rate of those atoms is given by an Arrhenius-like equation $\Psi = A\, e^{(-Q/T)}$, then the sputtering yield Y can be expressed as

$$Y = \int_0^{\infty} 2\pi x\, dx \int_0^{\infty} \Psi\, dt \tag{2-22}$$

If A and Q are independent of the temperature, then we can solve equation 2-22 to obtain the following expression for the sputtering yield Y:

$$Y = \frac{A\varepsilon}{8\pi\kappa C Q^2} \tag{2-23}$$

If κ and C are temperature dependent and can expressed as

$$\begin{cases} \kappa = \kappa_0 T^{n-1} \\ C = C_0 T^{n-1} \end{cases} \tag{2-24}$$

then solving equation 2-22 yields Y in the following form:

$$Y = \frac{n^2 A\varepsilon^2\, \Gamma(2n)}{8\pi\kappa_0 C_0 Q^{2n}} \tag{2-25}$$

where $\Gamma(2n)$ is a gamma function.

Johnson et al.[69] generalized the results of Vineyard, and they proposed that the sputtering of the target atoms is caused by evaporation from the transiently heated surface. The evaporation flux Φ can be written as

$$\Phi = \frac{CP}{(2\pi MkT)^{\frac{1}{2}}} \tag{2-26}$$

where P is the equilibrium vapor pressure ($P = P_0\, e^{(-U/T)}$) and U is the surface sublimation energy. For $\kappa = \kappa_0 T^{m-1}$, $C = C_0 T^{n-1}$, and the heat source $\varepsilon = f(dE/dX)$ where f is a constant. Substituting these expressions into equation 2-22 (replace Ψ in equation 2-22 with Φ) results in the following formula for the sputtering yield Y:

$$Y = \frac{mn^2 P_0 [f(\frac{dE}{dx})]^2}{8\pi(\kappa_0 U^m)(C_0 U^n)(2\pi MkU)^{\frac{1}{2}}} I \tag{2-27}$$

where I is a gamma function of n, m, U, and T.

Sigmund et al.[70] solved the sputtering yield (equation 2-22) using a nongaussian form of the temperature distribution function and an evaporation flux function $\Phi = N (k/2\pi M)^{1/2}\, e^{(-U/kT)}$. They obtained

$$Y = 0.036*24*(0.219)^2 \left(\frac{F_D}{U}\right)^2 g\left(\frac{U}{kT_0}\right) \tag{2-28}$$

where $\mathbf{F_D}$ is the stopping power at the surface of target given in equation 2-18; $g(U/kT_0)$ is the complex function shown in equation 2-29, and T_0 is the initial core temperature at $t=t_0$ in a cylindrical spike heated by F_D ($T_0 = F_D/2\pi NR^2$, where R is the initial width of the spike).

$$g(\xi) = (1+\xi-\xi^2)e^{(-\xi)} + \xi^3\int_{\xi}^{\infty}\frac{e^{-t}}{t}dt, \quad \xi = \frac{U}{kT_0} \tag{2-29}$$

For a small ξ, $g(\xi)$ is reduced to $g(\xi)\approx$ **1-($3\xi^2/2$)**, and thus for $T_0 >> U$, Y becomes proportional to the square of the stopping power (dE/dX) as was also the case for Johnson et al.'s expression (equation 2-27).

In summary, "the thermal spike model" leads to the primary result that if the energy deposition is high (high T_0) then the sputtering yield is proportional to the square of the stopping power.

Chapter 3

Experimental

3-1. Ion source and Wien filter

The primary ion source in our instrumental setup is single-lens liquid metal ion (LMI) column built by FEI company[71]. The LMI column is capable of producing a stable, positive metal ion beam with an intensity from 0.1 nA to 3 nA. The ions produced by the LMI column can be accelerated from 5 to 27 kV. Typically, the LMI column is operated with a 25 keV, 1 nA beam focused into a spot of 10-20 μm diameter at a 30 cm working distance (distance from the output of ion gun to the target). The LMI beam can be rastered; therefore, the system can be operated in a scanning ion microscope mode to produce an image of the target by collecting the secondary electrons or ions at the detector of the mass analyzer and using the signal generated to modulate the brightness of a video monitor scanned synchronously with the LMI beam. Figure 3-1 shows the principle of the ion microscope. Because the LMI column has a focused beam and a rastering capability, we are able to aim the beam onto microscopically small samples.

The LMI column can produce ions from a variety of metals, viz. Ga, In, Sn, Au, SiAu, and Bi. SiAu and Bi emitters are particularly interesting because they generate

Figure 3-1: Principle of ion microscope

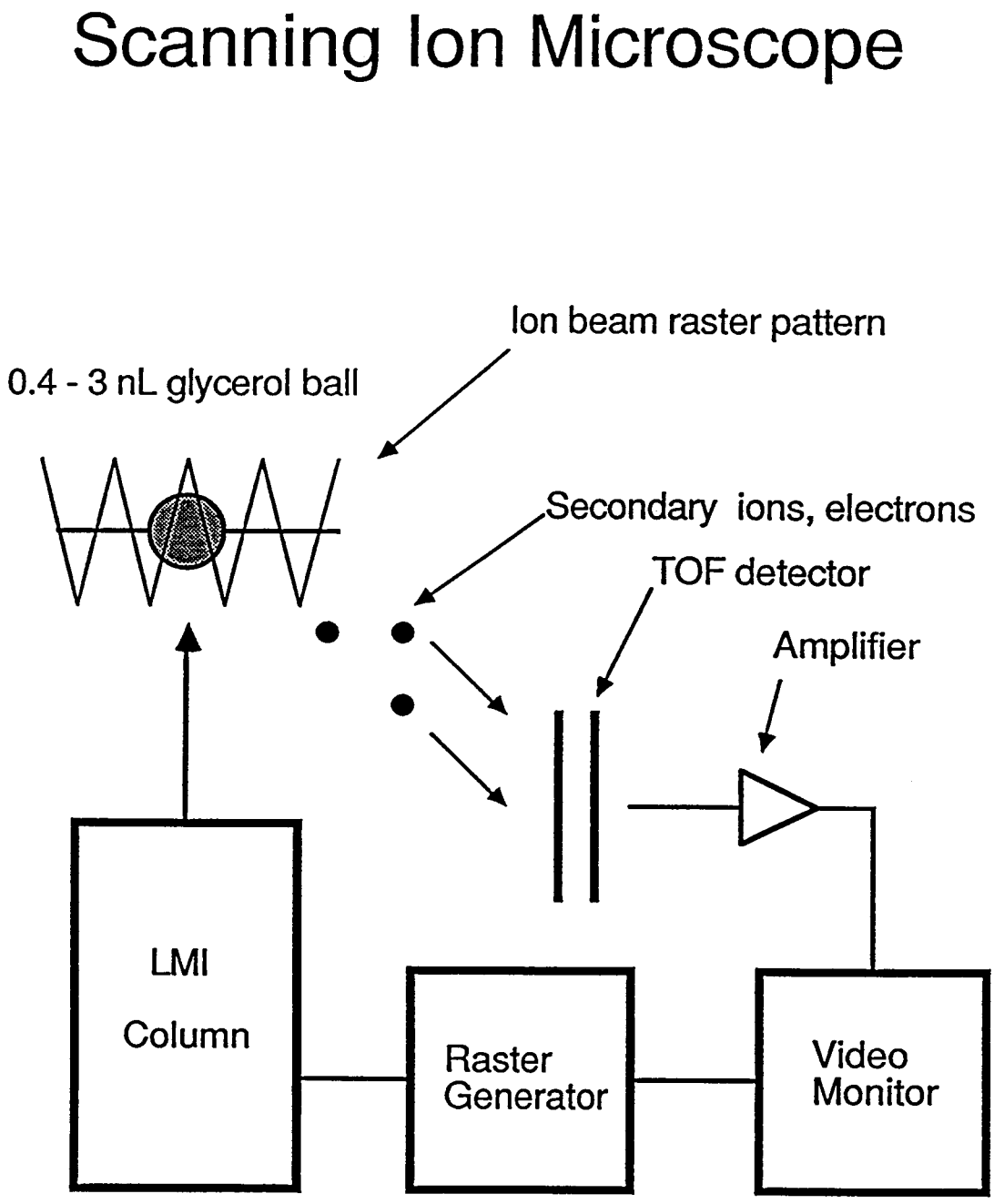

cluster ions. Figure 3-2 shows that the secondary electron spectrum produced a 25 keV Bi ion beam is repeatedly swept (1.2 kHz) across a 75 μm tungsten wire; the secondary electrons are accelerated with a static voltage of 2 kV. Since each Bi ion species has a different velocity the secondary electron spectrum consist of a series of peaks, each of which corresponds to an impact on the sample wire after a sweep pulse is fired at a set of deflection plates. Bi^+ is the lightest and thus arrives first at the target wire followed by Bi_3^{+2}, etc. Figure 3-3 shows the secondary electron spectrum generated by a SiAu emitter.

In order to study the mechanism of secondary ion emission under the influence of different primary ion species, a Wien filter[73] is used to disperse the different ions according to their velocity. Figure 3-4 shows the instrumental layout. The Wien filter is positioned between two sets of deflection plates. After exiting the Wien filter, primary ions pass through a 4 mm diameter aperture. This aperture has two functions: one is to provide a differential pumping isolation and the other is to select the different species of ions that emerges undeviated from the Wien filter. Figure 3-5 shows secondary electron spectra of a Bi ion beam without and with the Wien filter on. The upper spectrum in Figure 3-5 is the same as in Figure 3-3; the middle spectrum in Figure 3-5 shows the spectrum produced with the Wien Filter tuned to Bi^+; and the bottom spectrum in Figure 3-5 shows the spectrum with the Wien filter tuned to Bi_3^{+2}. The upper, middle, and bottom spectra of Figure 3-6 show the isolated secondary electron spectra of Bi_2^+, Bi_3^+, and Bi_4^+ respectively. From Figure 3-5 and Figure 3-6,

Figure 3-2: Secondary electron spectrum from 75 μm tungsten wire bombarded by 25 keV Bi ion beam

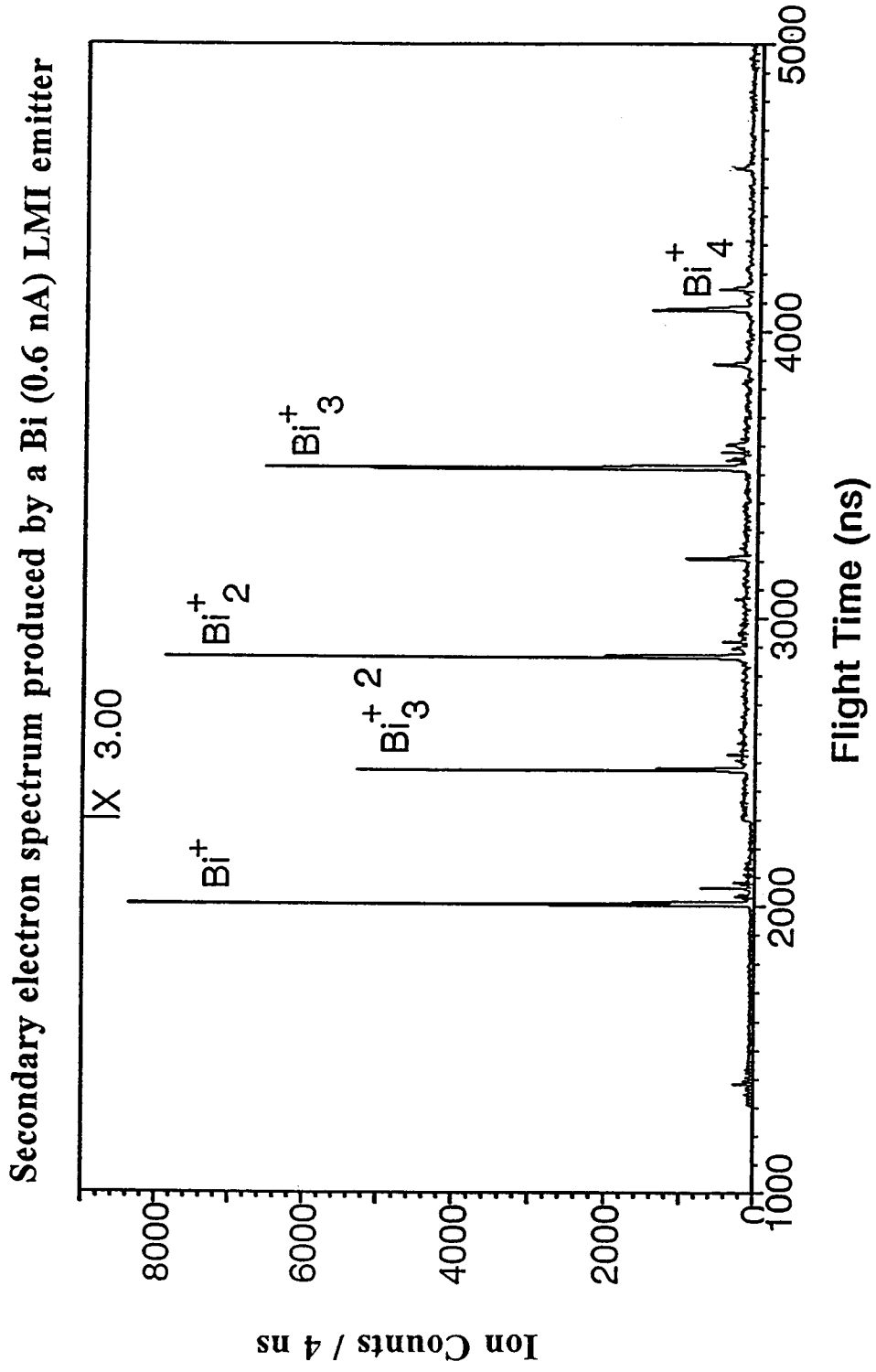

Figure 3-3: Secondary electron spectrum from 75 μm tungsten wire bombarded by 25 keV SiAu ion beam

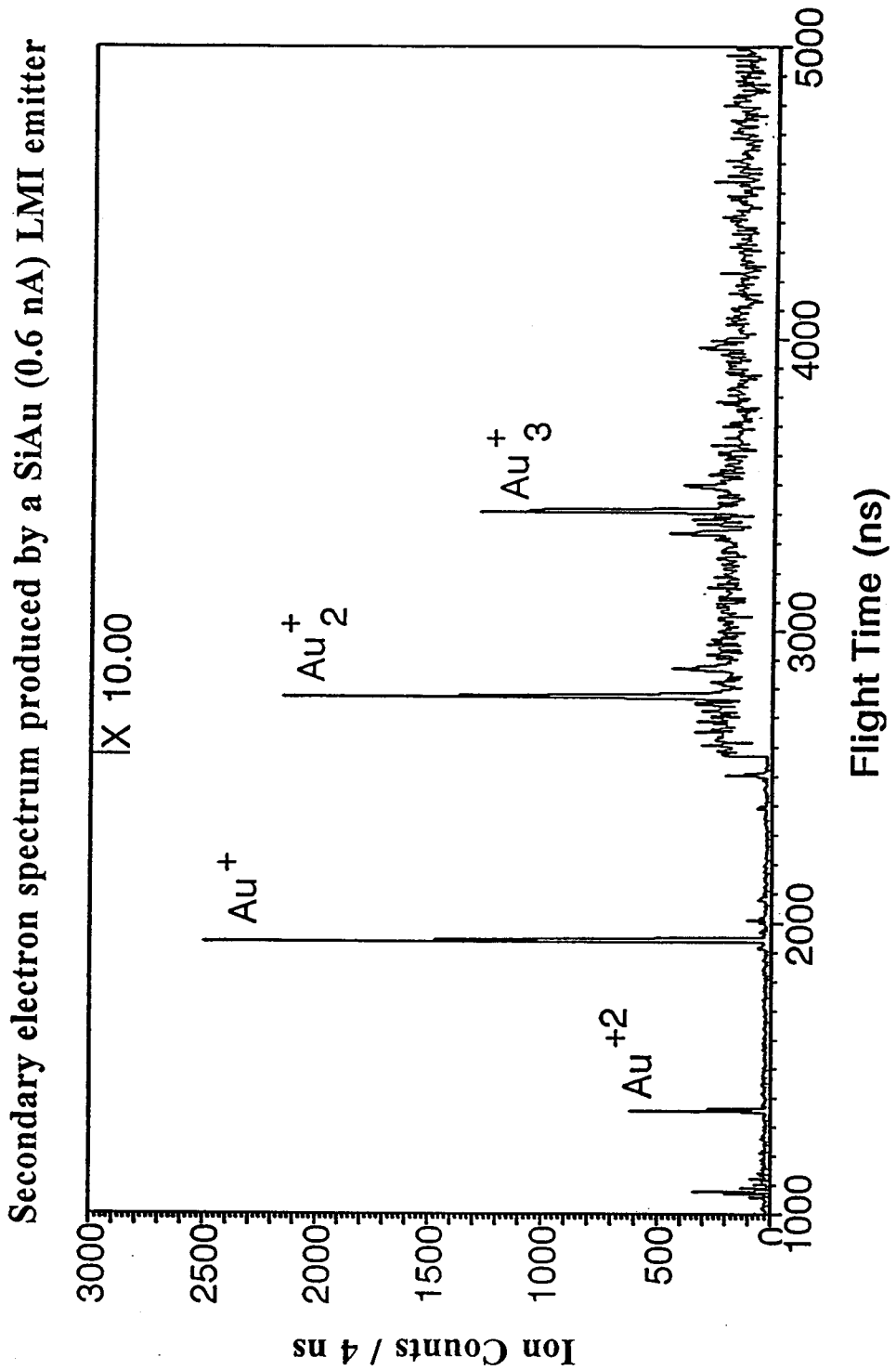

Primary Ion Column:

1) Liquid metal ion column
2) Deflection plates
3) Wien filter
4) Deflection plates
5) Aperture (4mm)

Secondary Ion Column (time-of-flight analyzer)

6) Faraday cup
7) Sample support
8) Acceleration grids
9) Flight tube
10) 90° ion mirror
11) 1st detector
12) 2nd detector
13,14) Diffusion pump

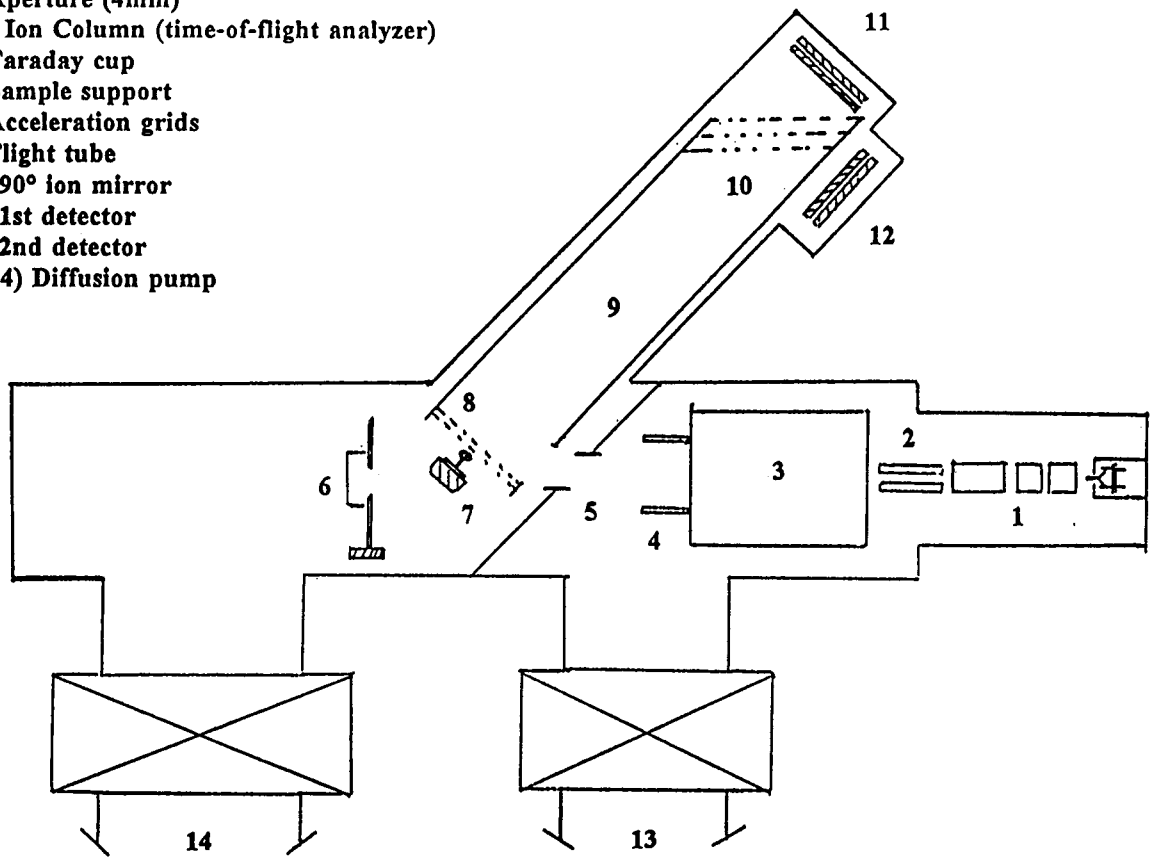

Figure 3-4: Instrumental layout

Figure 3-5: Secondary electron spectrum bombarded by Bi(25 keV) ion beam (upper) and isolated secondary electron spectra of Bi^+ (middle), Bi_3^{+2} (bottom)

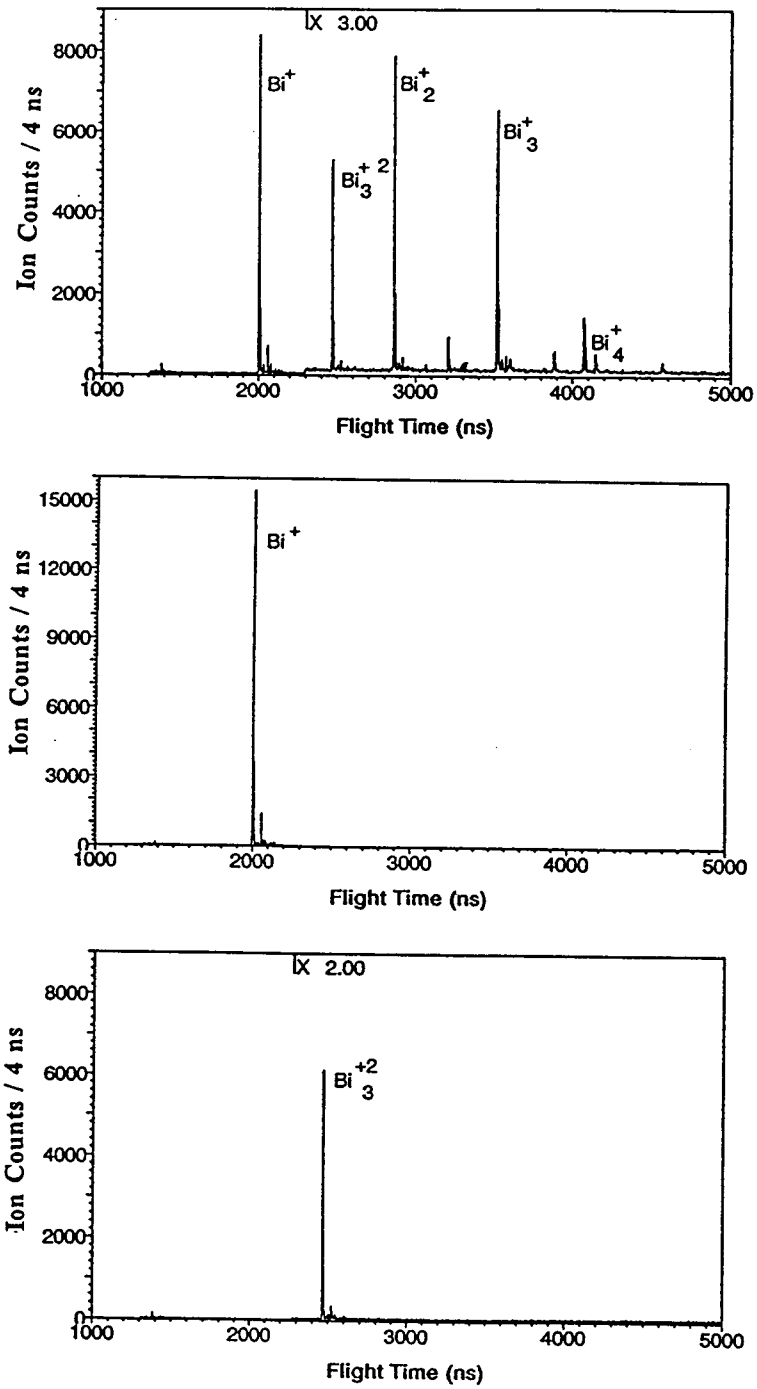

Figure 3-6: Isolated secondary electron spectrum of Bi_2^+ (upper), Bi_3^+ (middle), and Bi_4^+ (bottom)

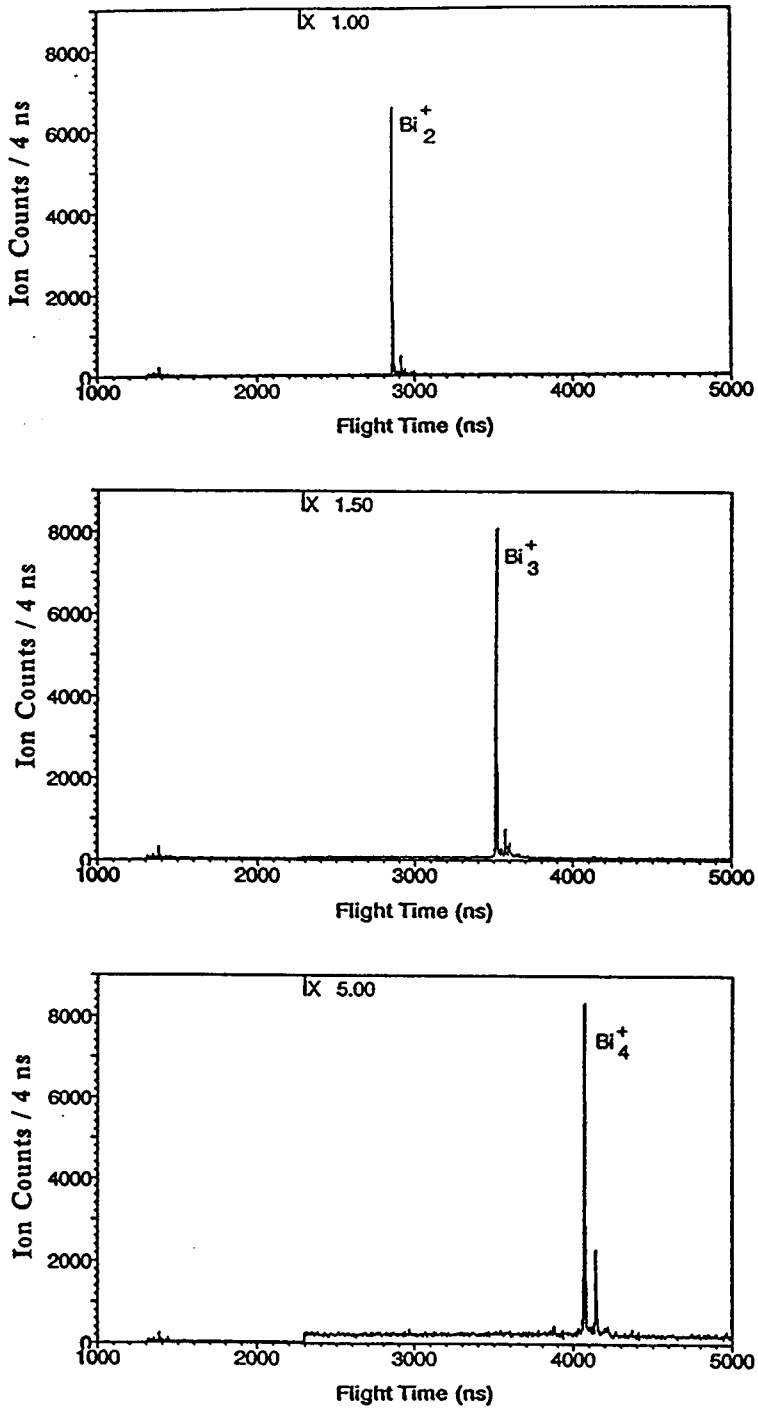

it is clear that the ion beam from the Bi emitter is well dispersed by the Wien filter. A similar set of spectra for Au is shown in Figure 3-7 and Figure 3-8.

3-2. Sample preparation

All the analyte samples were purchased from Aldrich or Sigma chemical company and were used as received. The compounds used in this study are listed in Table 1.

Two different methods were used to prepare samples before loading them into the mass analyzer. The first one was to dissolve the analyte in water solution at same concentration in the range of 1 ng/μL to 1 μg/μL then, using a microsyringe, to draw out 0.2 μl of the solution and add it to a 3 nL ball of liquid matrix (e.g. glycerol) suspended on a tungsten wire (25 μm diameter). The water is evaporated almost entirely by letting the sample ball sit in the air about half an hour. The size of sample ball after this time is nearly the same as the size of the original ball of pure matrix liquid.

The second sample preparation method is to make a water solution of the sample with a concentration from 0.05 M to 0.01 M and then to mix this solution with a 4 to 9 times larger volume of liquid matrix. A 3 nL ball of this analyte/matrix mixture is then transferred to the sample support wire of the sample holder. In general, the final

Figure 3-7: Secondary electron spectrum bombarded by SiAu(25 keV) ion beam (upper) and isolated secondary electron spectra of Au^+(middle), Au^+ (bottom)

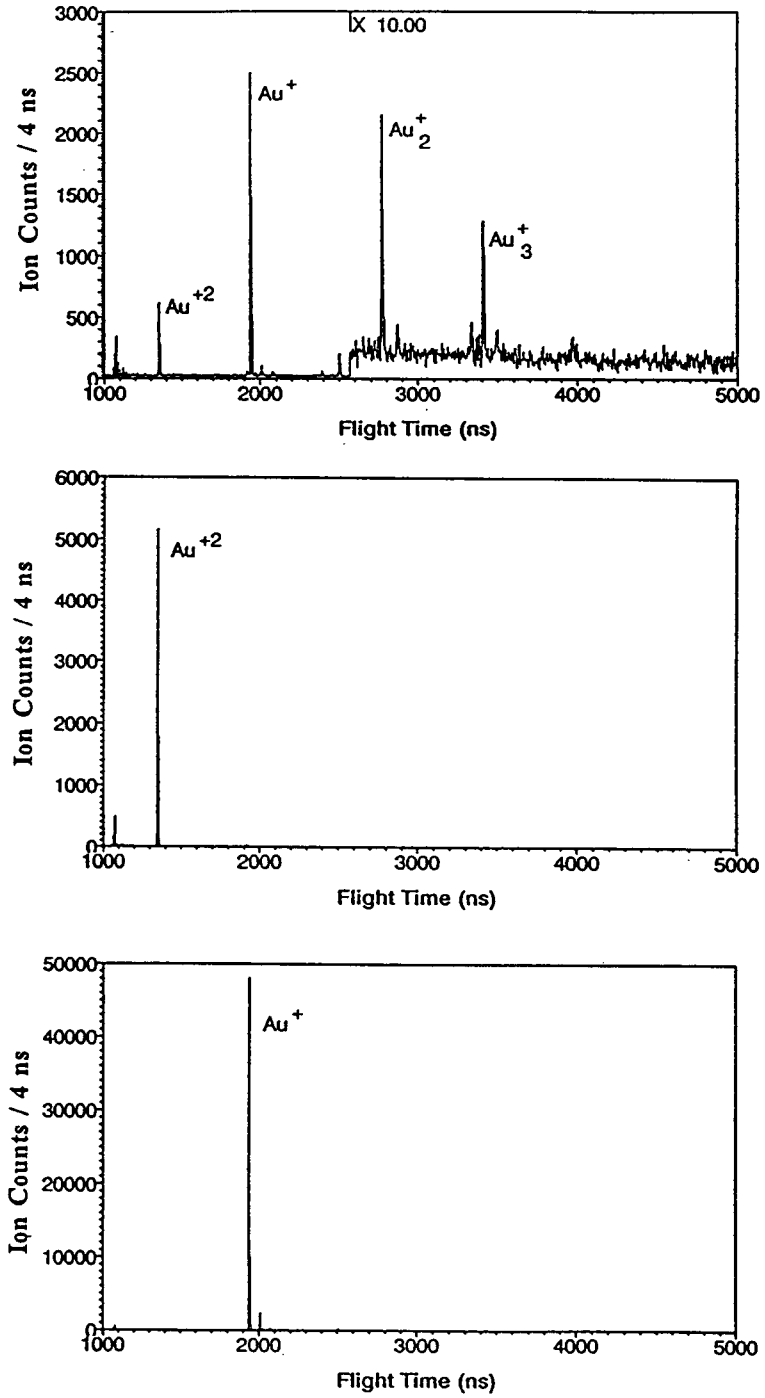

Figure 3-8: Isolated secondary electron spectrum of Au_2^+(upper), Au_3^+(bottom)

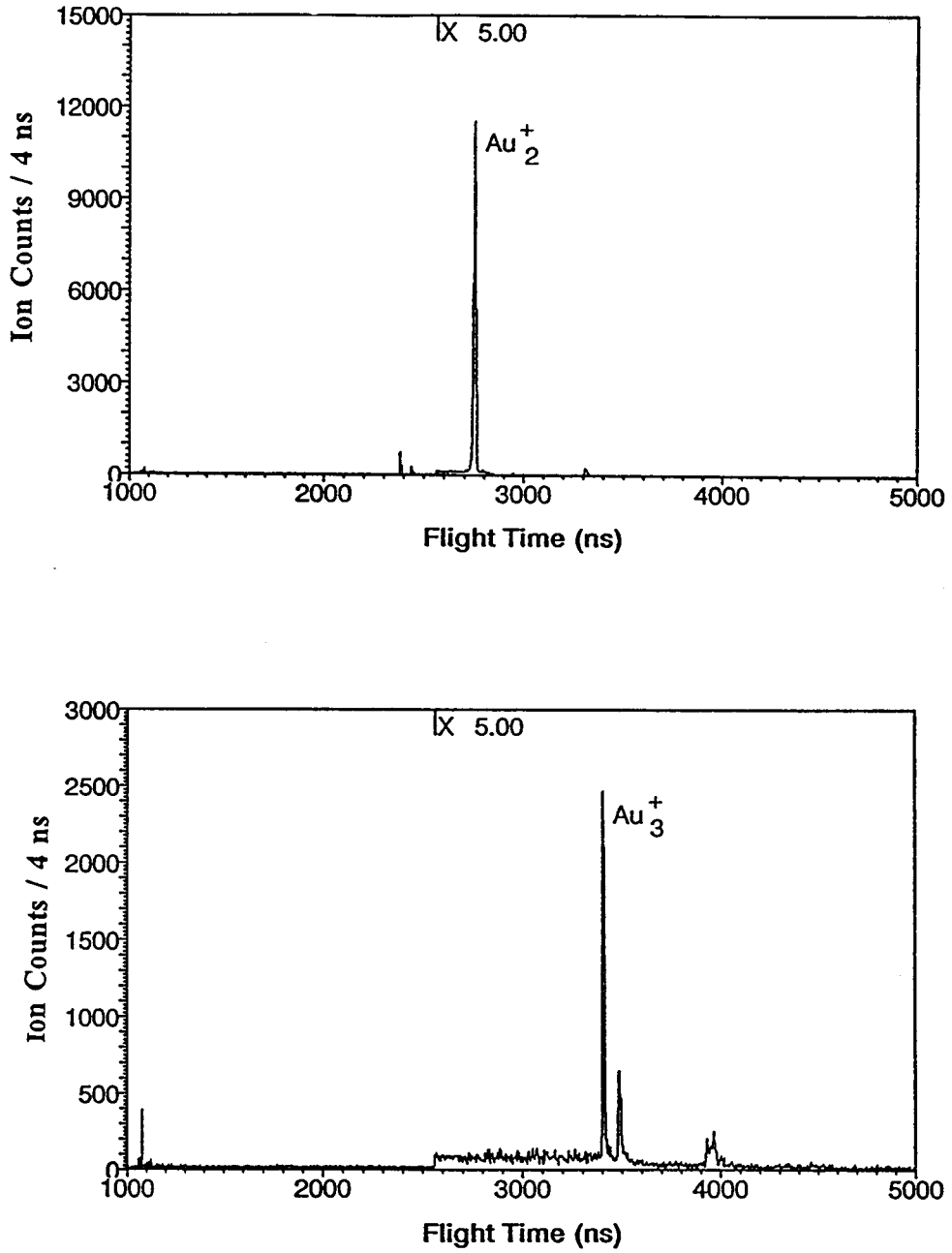

Table 1: Compounds used in experiments

Compound	Contents
ionic compound	CsI
amino acids	alanine, cysteine, tryptophan, leucine
peptides	met-enkephalin, gramicidin S, gramicidin D, melittin
nucleosides	deoxyadenosine(dA), deoxyguanosine(dG), deoxycytidine(dC), thymidine(T)
nucleotides	deoxyadenosine monophosphate(dAMP), deoxyguanosine monophosphate(dGMP), deoxycytidine monophosphate(dCMP), thymidine monophosphate(TMP)
matrices	glycerol, thioglycerol
surfactant	hexadecylpyridinium acetate(HDPA)

concentration of analyte in the liquid matrix ranges from 0.01 M to 0.001 M; however, it can be further diluted to 10 μM.

We have not found any significant differences in the secondary ion spectra generated from either of these two sample preparation methods. The total sample contained in a 3nL ball is between tens of picomoles to tens of femtomoles.

Figure 3-9 shows a diagram of a sample holder base. Small volume (~ 3 nL) of glycerol, either pure pr mixed with analyte, are transferred (~ 160 μm diameter sample ball) to the 25 μm sample support wire of the base using an etched tungsten wire (Figure 3-9). It is essential that the sample balls all have the same diameter since, as will be described in the section on secondary ion production, the diameter of the target ball determines the dose of primary ions striking it. Therefore, the sample balls are loaded onto sample support wire under a microscope to ensure that each experiment is performed with sample balls of essentially the same diameter. Via this method, variation in the diameter of the sample balls can be held to less than 5 %. After loading the sample ball onto the sample holder base, the probe is introduced into the ion source of the time-of-flight mass analyzer through a vacuum lock.

The most important compounds employed in this study are the mononucleotides from a matrix of hexadecylpyridinium acetate (HDPA), surfactant, in glycerol. This system affords us a degree of control over the surface of the target under particle

Figure 3-9: Sample holder unit

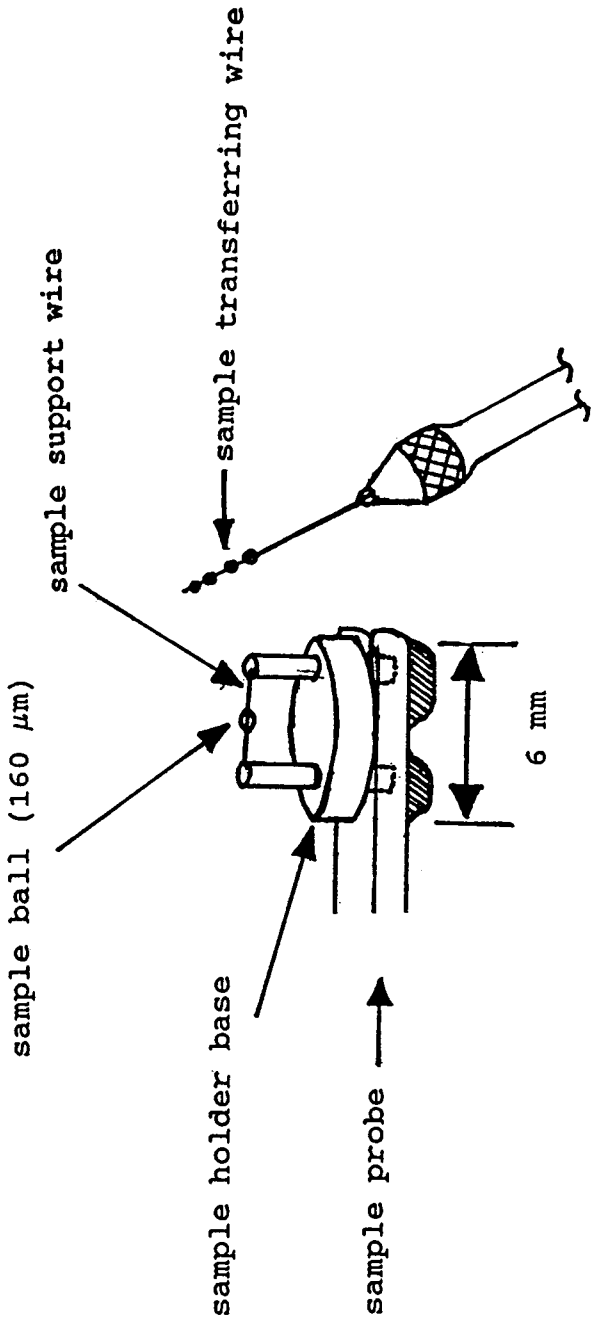

bombardment. The preparation method of HDPA has been reported by Ligon et al.[48] and will not be shown in detail. Matrix of HDPA in glycerol is prepared from a water solution of HDPA mixed with glycerol to a final concentration range from 0.01 to 100 mM of HDPA in glycerol. After a water solution of mononucleotides is mixed with this matrix (0.01 to 100 mM HDPA in glycerol) the concentration of mononucleotides range from 0.01 to 1 mM. The diameter of sample balls have been further reduced into an half of the original diameter (80 μm) in order to approach the lowest detection limit. The volume of a 80 μm diameter sample ball is about 0.4 nL.

So far we have discussed the preparation of samples in a liquid matrix. CsI is a compound which can be easily prepared either in a liquid matrix or as a solid deposit. For solid phase deposition, a 50% methanol/water solution of saturated CsI is prepared and is loaded onto a 25 μm wire attached to a sample holder base. Care is taken to keep the size of the CsI deposit about the same size as the liquid matrix sample ball after the methanol and water have evaporated.

3-3. Time-of-flight mass analyzer

The schematic diagram of our linear time-of-flight mass analyzer is shown in Figure 3-10. This is modeled after the design of Tang et al.[74]. A linear time-of-flight mass spectrometer has features, such as high transmission (near 50% transmission), simultaneous detection of all ions, unlimited mass range, and a physically simple

Figure 3-10: Schematic diagram of the time-of-flight mass analyzer

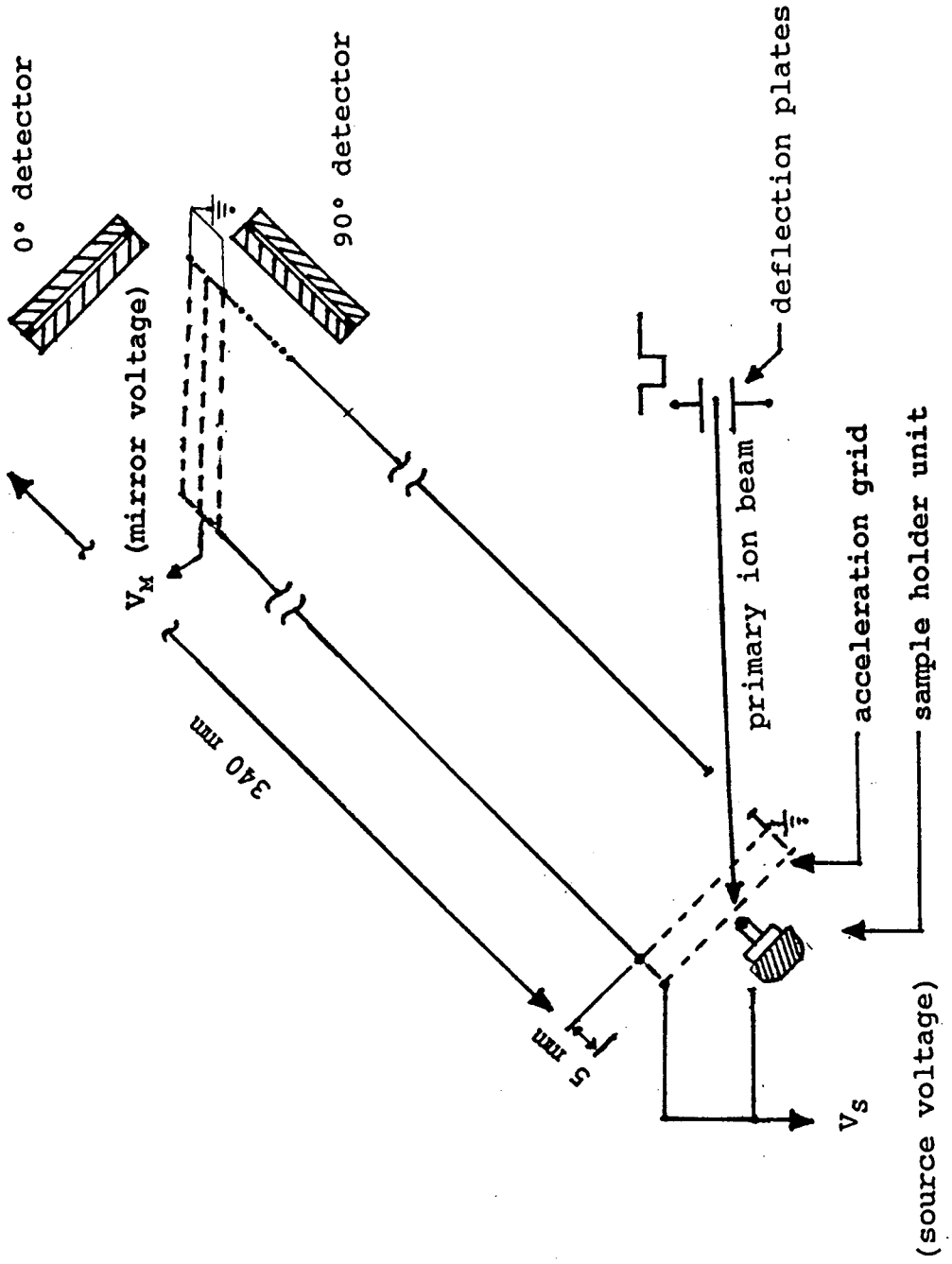

structure that can be easily machined that are well suited to secondary ion yield measurements.

The flight tube is composed of a high voltage source region, 5 mm long and a electrical field free region, 34 cm long. Near the end of the flight tube, there is an ion mirror, tilted 45° with respect to the mass spectrometer's axis, that can be used to deflect the charged particles 90° into an off axis detector. The mirror can be used to study the decomposition of metastable ions into charged fragments (daughter ion) and neutral fragments during flight in the field free region of the analyzer tube. Two detectors are employed in the time-of-flight mass spectrometer. One of them (0° detector) is located after the ion mirror to detect neutral particles when the ion mirror is activated or secondary ions when the mirror is not activated. The other detector (90° detector) is located to detect the deflected charged particles when the ion mirror is activated. Details of ion detection will be discussed later.

During operation, a series of ion pulses generated by the primary ion column (Figure 3-4) are directed at the sample, through the source grids (grounding grid and acceleration grid) at a angle of 45° with respect to the axis of the secondary ion flight tube. The ion pulses arrive at a frequency of 1.2 kHz. A static high voltage V_S is applied to the sample holder unit and the acceleration grids by a stable 0-10 kV DC power supplier (Fluke Company). In most of our experiments, V_S was fixed at 6 kV for the positive ion detection mode and at -6 kV for the negative ion detection mode.

Calculation of a secondary ion's flight time will be discussed in the section 3-6. In order to ensure a high transmission of secondary ions as well as a homogeneous electrical field distributions, 90% transmission nickel mesh (40 μm diameter wires and 760 μm spacing) purchased from Bukbee-Mears Company, are used for the all of the grids in the instrument.

The background pressure in the flight tube is kept at 2×10^{-7} torr. When the liquid matrix is loaded into the system, the pressure rises up to 2×10^{-6} torr. The sample probe inlet system utilizes a vacuum lock to minimized loss of vacuum when the sample probe is introduced into the mass analyzer.

3-4. Secondary electron or ion production

Pulses of secondary electrons or ions are generated by sweeping the primary ion beam across a tungsten wire or a target ball (liquid matrix with analyte) suspended on tungsten wire. A pair of defection plates connected to a pulse generator is used to deflect the primary ion beam up and down across the sample target. This procedure, which allows only a limited primary ions to impinge on the target per sweep cycle, provides two advantages: 1) radiation damage to the surface of the target is minimized, and 2) the chance of generating two or more ions with the same mass to charge ratio in a given sweep cycle is substantially reduced. This latter features is particularly important for secondary ion yield measurements that rely on single ion counting methods

for detection and recording. Two ions with the same mass to charge ratio would also have the same velocity in the flight tube; therefore, they would arrive at the detector at the same time and be recorded as one signal. This would be a miscount of secondary ion yield.

A pulsed ion beam produces less radiation damage on the surface of the sample and this factor must be taken into consideration in any form of sputtering experiment. A quantitative discussion of the destructive effects due to bombarding the surface of a organic matrix follows.

Consider a monolayer or submonolayer of organic analyte adsorbed onto a solid matrix as shown in Figure 3-11. An incoming energetic ion strikes the surface of the analyte, and generates an energized area from which analyte is sputtered or damaged as a result of the energy transferred to the matrix by the primary ion. This energized area can no longer yield an intact analyte ion. If coverage of the surface by the analyte is indicated by $\theta(t)$ and the constant flux of the primary ions is δ (number of ions striking the surface/per unit time/per area), we can obtain an expression for $\theta(t)$ as:

$$\frac{d\theta(t)}{dt} = -\sigma\delta\,\theta(t) \quad ; \tag{3-1}$$

$$\theta(t) = \theta_0 e^{-\sigma\delta t} \quad . \tag{3-2}$$

Figure 3-11: Disappearance cross section

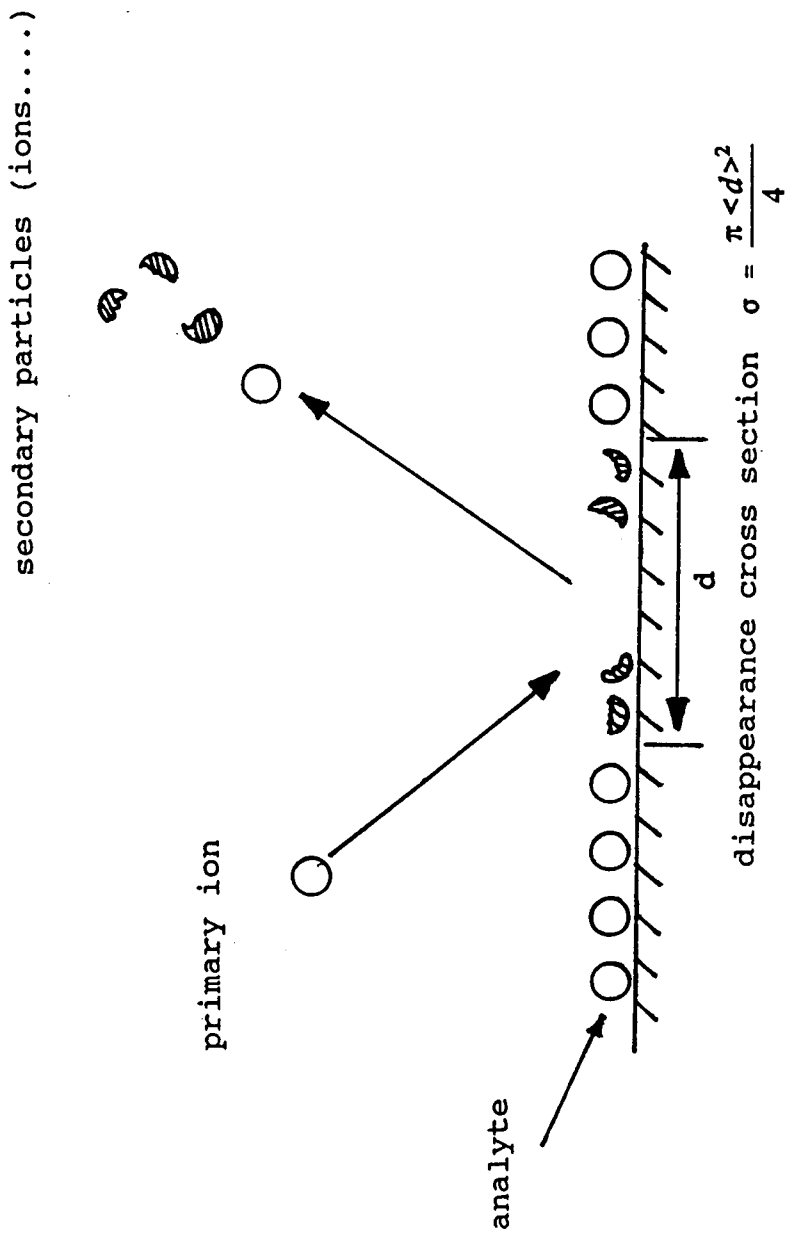

where θ_0 is the original surface coverage before ion bombardment (θ_0=1, for a monolayer of analyte) and σ is the disappearance cross section (the average area damaged per incoming ion) of the analyte in cm^2.

If the ionization probability of organic analyte is not changed with time, then the sputtering ion yield of an analyte as a function of time in a given surface coverage can be expressed as:

$$Y(t) = Y_0\,\theta(t) = Y_0\,\theta_0 e^{-\sigma\delta t} \qquad (3\text{-}3)$$

where Y_0 is the sputtering ion yield of a monolayer of analyte.

Based on the surface coverage function $\theta(t)$, we can quantitatively define two distinct operational modes for secondary ion mass spectrometry: 1) static, $\sigma\delta t \ll 1$, and 2) dynamic, $\sigma\delta t \gg 1$. It is clean that in the static mode $\theta(t)$ is almost constant over time; whereas, in the dynamic mode $\theta(t)$ changes rapidly.

The flux δ multiplied by the time t of ion bombardment is equal to the dose of incoming ions. In our experiments, the total number of start pulses given to a typical sample (160μm diameter) was normally fixed at 300,000 for each secondary ion spectrum. For an ion beam with a 1 nA intensity and sweep time across the ionization zone of 12 ns, δt is equal to 5.72×10^{11} ions/cm^2. The magnitude of the disappearance cross section σ is dependent on the analyte's identity and the of primary ion's energy.

Salehpour et al.[77] have reported that the disappearance cross section of molecular valine ion bombarded by 90 MeV $^{127}I^{14+}$ is about 6.8 x 10^{-13} cm^2. Benninghoven[76] reported that σ of some organic analytes (peptides, nucleotides) on a solid matrix bombarded with the keV primary ions is equal on the average to 5 x 10^{-14} cm^2.

In practice, we control δt in our experiments and measure the secondary ion yield $Y(t)$ of the analyte under investigation (we measure the relative yield not the absolute yield and details of these will be discuss in section 5-1.). The ion beam intensity is measured with a Faraday cup connected to an electrometer (model 600A, Keithley Company) that is floating at 50 V to prevent secondary electrons from escaping the cup. The following expression for the disappearance cross section of the analyte is obtained directly from equation 3-3 :

$$\sigma = \frac{\ln[Y(t_1)] - \ln[Y(t_2)]}{\delta(t_2 - t_1)} \quad , t_2 > t_1, \tag{3-4}$$

where t_1, and t_2 are two different times. We have measured the disappearance cross section of the analyte (mononucleotides) from a matrix of hexadecylpyridinium acetate in glycerol and results will be shown in section 4-7.

3-5. Ion detection, and data acquisition

3-5A. Ion detection

The particle detector used in this study consists of a pair of 25 mm diameter

microchannel plates (Galileo Electro-Optics Corporation) separated by a 200 μm thick stainless ring. The detector assembly is shown schematically in Figure 3-12. Two 90 % transmission grids, spaced 5 mm apart, are mounted 5 mm in front of the detector assembly. These grids can be used: 1) to postaccelerate the secondary ions in order to gain detection efficiency, and 2) to retard the secondary ions in order to analyze their axial velocity distribution. For the former usage, G_2 (Figure 3-12) is grounded and a postacceleration voltage V_P (floating) is applied to the detector; the polarity of V_P is opposite to the charge of the ions being detected. For the later usage, a retarding voltage V_R (> V_S, the acceleration voltage) is applied to G_2 to allow ions with a specific axial velocity (relative to the flight tube) to passing through to the detector.

The microchannel plates each contain a large numbers ($\approx 10^5$) of small channels (10 μm diameter) biased 12° with respect to the surface normal. Each microchannel plate has a particle gain of about 6×10^3 with 900 V applied across the plate. By joining a pair of microchannel plates with their channels at opposite bias (Figure 3-12), a so called the chevron assembly, the gain can be doubled and the ions feedback can be suppressed thereby improving the signal to noise ratio. The structure and operational theory of microchannel plates has been reported in detail by Wiza[78]. Briefly, when a secondary ion impinges on the wall of a channel in the top plate of the chevron assembly, it produces an electron shower that further excites a large number of channels in the bottom plate of the chevron assembly. The electrons are collected on anode C. This produces a voltage pulse, ~1 ns in duration, that passes through a 500 pF capacitor,

Figure 3-12: Detector assembly

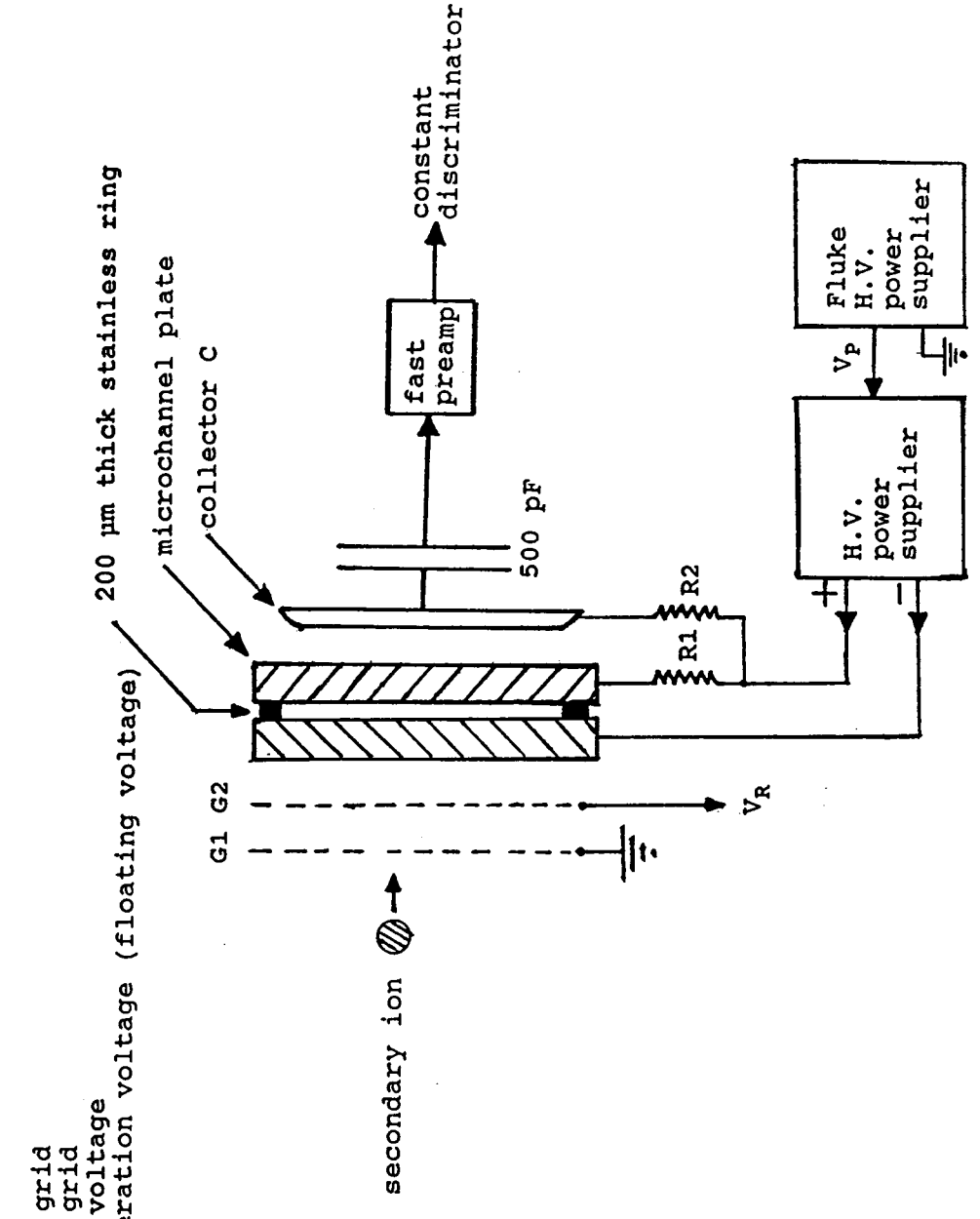

which can be floating at 20 kV without breakdown, and is amplified by a factor of 10 with a fast preamplifier (model 9305, EG&G Ortec Company).

The detection efficiency of a chevron plate varies with the identity, and energy of the impinging particle. The critical factor for particles of the size used in this study is the probability of generating secondary electrons from the wall of channel of the microchannel plate when a energetic particle strikes it. Ions with heavier mass but slower velocity normally produce fewer secondary electrons than lighter, faster ions. Beuhler et al.[79] have shown that secondary electron emission induced by 10^6 to 10^7 cm/s water clusters striking the surface of a copper electrode is strongly dependent on the velocity of the water cluster ions. They also found that almost no electrons can be detected when the velocity of the incident water cluster ions falls below 10^6 cm/s. Our measurements of the detection efficiency of deprotonated dGMP (deoxyguanosine monophosphate), $(M-H)^-$, as a function of velocity are shown in Figure 3-13. The relative yield in this figure is defined as the intensity of deprotonated dGMP in given velocity divided by the maximum intensity of deprotonated dGMP (where V_S=6kV, V_P=-6kV in Figure 3-12).

We need to point out another critical factor for detecting negative secondary ions in our instrument. A given channel in a microchannel plate has a dead time about 20 ms after it has been fired; this is the time required for replenishing the charge in the wall of channel. The dead time is determined by the channel's RC constant, where R

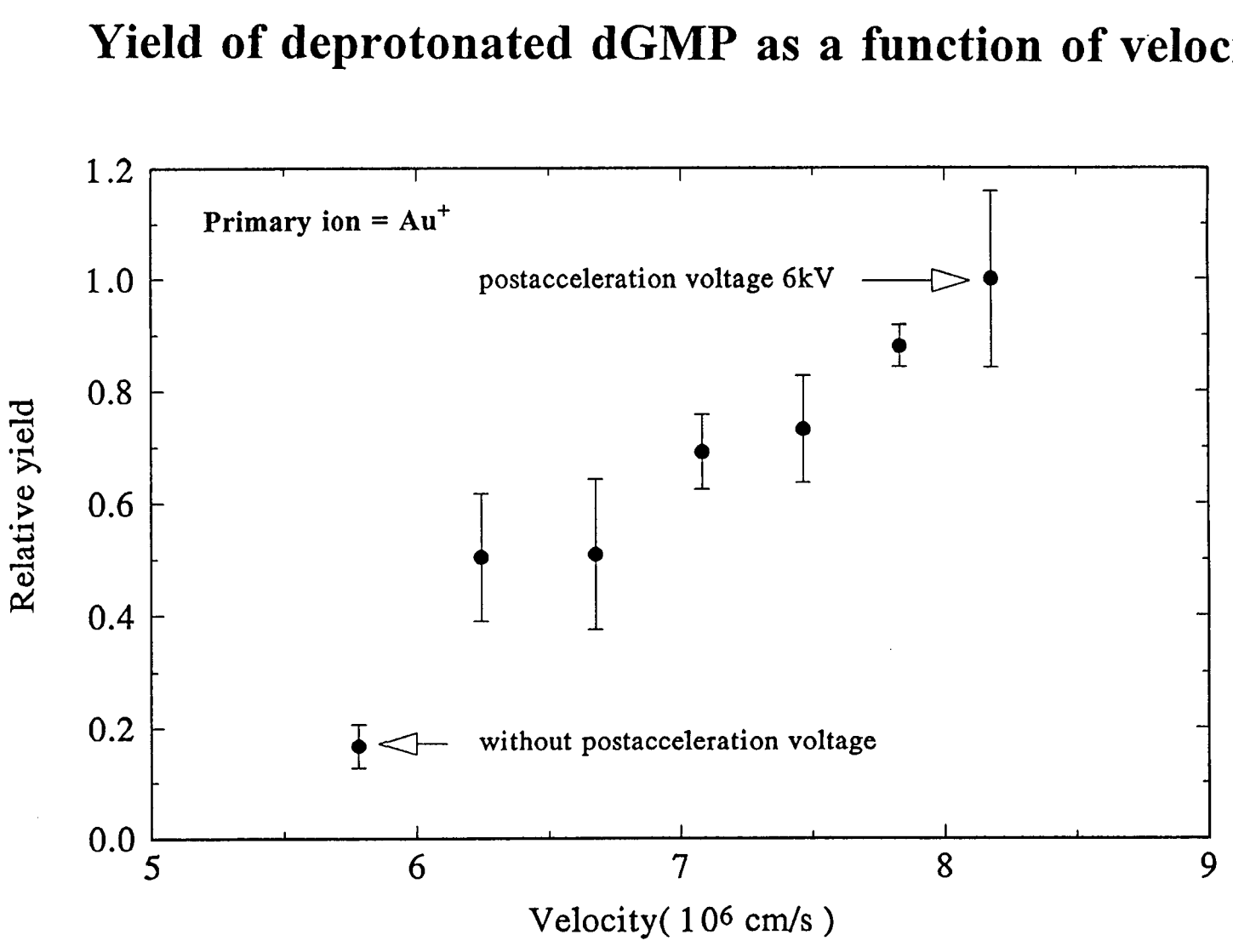

Figure 3-13: Yield of deprotonated dGMP as a function of velocity

is the internal resistance and C is the internal capacitance of the channel. During its recovery, no particle can be detected in the channel. When we operate our mass spectrometer in the negative ion mode, a large number of secondary electrons as well as a small number of negative secondary ions are produced at the target. The electrons run down the flight tube faster than the negative ions and trigger a large number of channels in the detector about 0.3-20 μs before the negative ions start to arrive at the detector. When the ions strike those channels that have been fired by electrons (and there is a high probability that this will happen), they are not detected. Therefore, the detection efficiency is very low in the negative secondary ion detection mode. In order to overcome this problem, a small pair of magnets was installed in the electrical field free region of the flight tube right after the source's grounding grid; these magnets deflect the electrons emerging from the ion source but have little effect on the secondary ions. This prevents the secondary electrons from saturating the detector and greatly increases the detection efficiency for the negative secondary ions.

3-5B. Data acquisition

A diagram of the data acquisition system is shown in Figure 3-14. The pulse generator (model 114A, Systron Donner Inc.) produces a pulse to deflect the ion beam up and down across the sample zone; it also generates a synchronous signal to trigger the #1 gate and delay generator (model 416, EG&G Ortec Company). After being triggered by the falling edge of the input pulse, the gate and delay (adjustable from 10

Figure 3-14: Data acquisition system

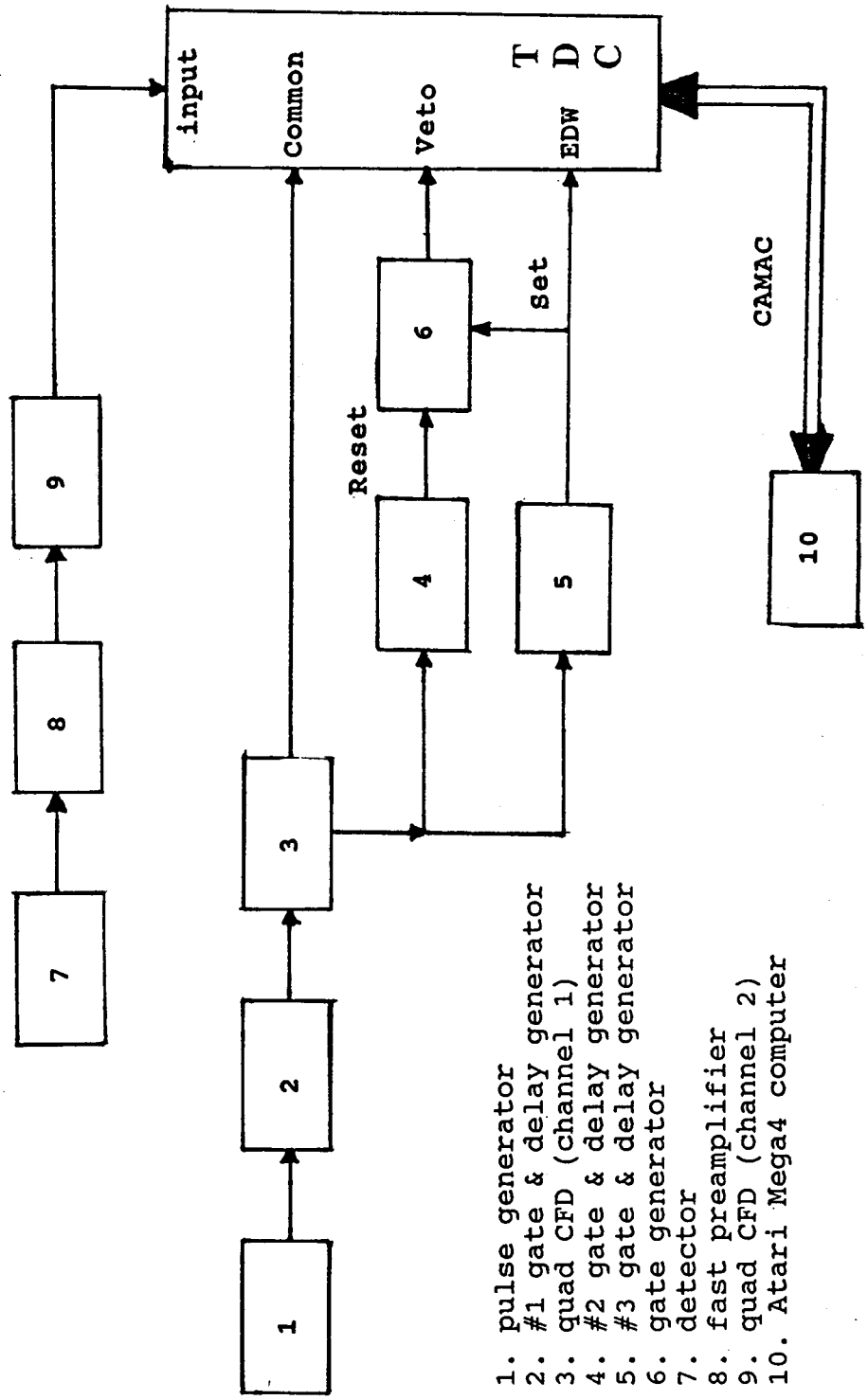

ns to 110 μs) generator sends a NIM logic output pulse (-0.6 V into 50 Ω, rise time ≤ 10 ns) with a 10 ns delay to trigger the first channel of a quad constant factor discriminator, quad CFD (model 7174, Entertec Company). Each channel of the quad CFD has four output connectors so that it can send four synchronous signals after being triggered by the input signal. The first channel of quad CFD does not serve as a signal level discriminator in this application but rather as a synchronous signal generator with these outputs. One of these three signals goes to the common connector of a time-to-digital converter, TDC (model 4208, LeCroy Company), to start its internal clock; the other two output signals are connected with the #2 and #3 gate and delay generators to produce properly delayed output signals for setting and resetting a gate generator (model GG-1, Paulus Engineering Company). The gate generator sets a veto period in the TDC that disables the input signals. The #3 gate and delay generator also triggers an end of window (EDW) signal in the TDC to stop its internal clock.

The LeCroy 4208 TDC is a standard CAMAC (computer automated measurement and control) module that can record 8 individual time events either from separated signals delivered in parallel to its 8 input terminals or from sequential inputs delivered to the number 1 input terminal that, in turn, is connected in series with the other input terminals. In our experimental arrangement, we employ the latter method to collect a sequence of secondary ion signals. The Lecroy TDC has an 8.3 ms recording time period and a maximum resolution of 1 ns.

A detailed of diagram of the pulse logic employed is shown in Figure 3-15. The pulse generator produce a 50 μs pulse (-20 V amplitude, 1.25 kHz repetition rate) that initializes the system for data acquisition. After the common terminal of TDC accepts an input signal from channel 1 of the quad CFD, the TDC starts its internal clock. At this stage the TDC could record times triggered by event signals delivered to its input connector (the number 1 input terminator); however, a NIM input signal from the gate generator to the veto terminal of the TDC is set to disable the TDC from registering any input signals for a time period of 0 to 3 μs. This veto period is used to increase recording efficiency for collecting the secondary ions generated by bombardment with cluster ions, such as Bi^+_2, Bi^+_3. When these primary ions are used, the background signals from low mass secondary ions generated by other species of primary ions, which are not blocked by the isolation aperture (Figure 3-4) and strike the grids in the source region, are so strong that they can saturate all 8 inputs of the TDC. A proper veto period can prevent the TDC from registering those background signals. After the veto signal is turned off (rest), input signals to the TDC are registered, the #3 gate and delay generator sends a signal to the EDW terminal of the TDC stopping the internal clock after 32 μs and also sends a signal to the CAMAC control bus to tell the computer that the TDC is ready to transfer its data to the computer. The computer accepts this signal then starts to process and store the TDC's data.

An Atari Mega4 computer (Atari Corporation) is employed to control data acquisition. This computer is connected with a CAMAC bus controller (model 1311,

Figure 3-15: Diagram of pulse logic

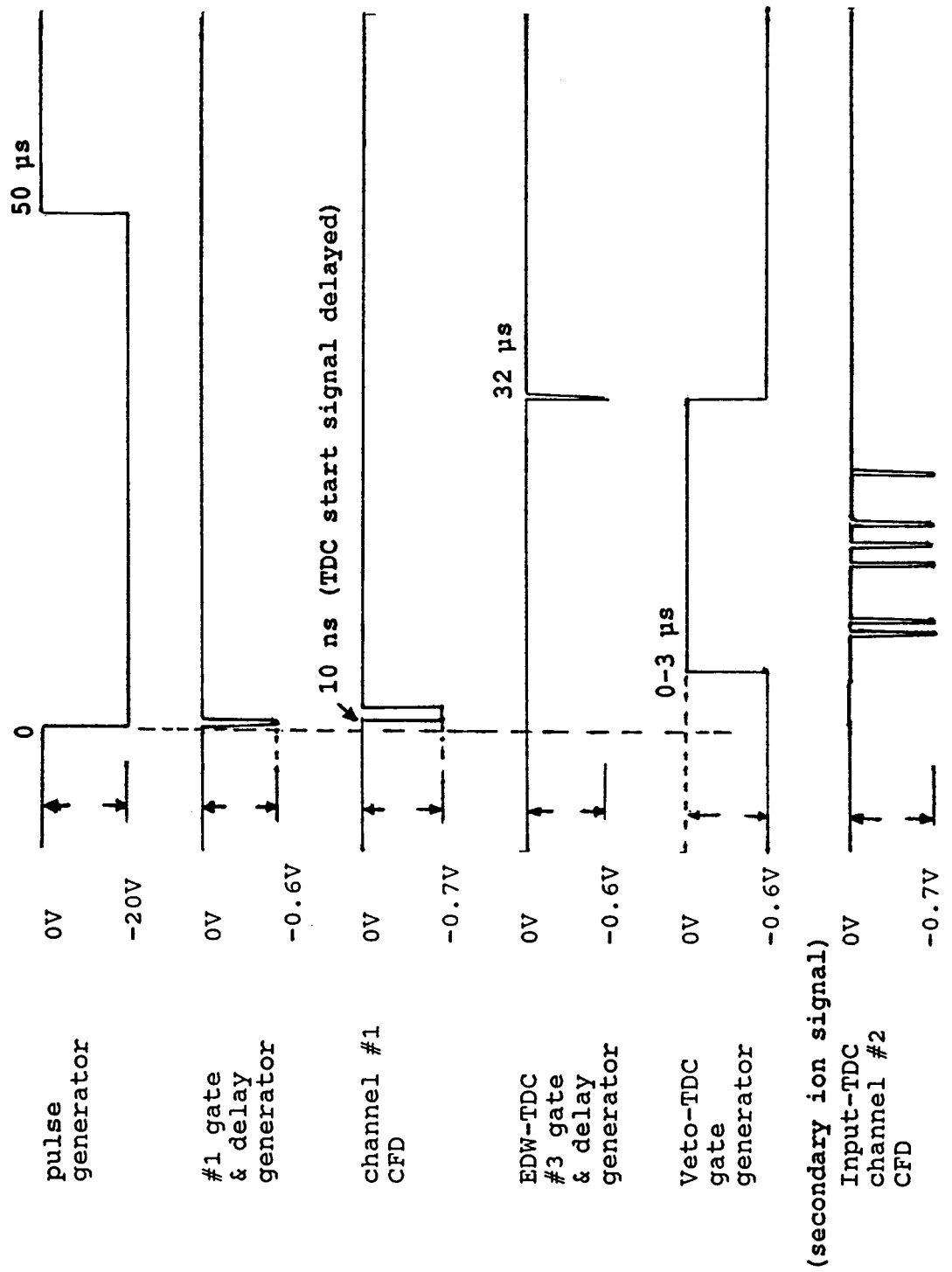

Bi Ra Company) to control the TDC and transfers the ion event data (the time of arrival of the ions striking the detector) stored in the TDC's memory. The software program used for acquisition processing, and analysis of the time-of-flight mass spectra is TOFMA program written by Dr. W. Ens[80]. The TOFMA program can be set to record for a prescribed number of start pulses in order to exactly control the primary ion dose used to generate each secondary ion spectrum.

3-6. Flight time of secondary particles

Secondary ions or electrons generated by keV particle bombardment are accelerated in the source region by a static voltage V_S. After entering the field free region (Figure 3-16), they maintain a constant velocity as they traverse the flight tube. Before these ions strike the chevron detector, they are accelerated by a static postacceleration voltage V_P. The physical dimensions of the linear time-of-flight mass spectrometer are shown in Figure 3-16. Flight times for ion reflected in the ion mirror will not be treated in this dissertation.

The relationship between the flight time t_1 of a secondary ion with mass m and acted on by a constant electrical force $F=qV_S/l_1$ in the source region and its flight distance l_1 is given by the expression

$$l_1 = \frac{1}{2}at_1^2 \qquad (3\text{-}5)$$

Figure 3-16: Physical dimensions of flight tube

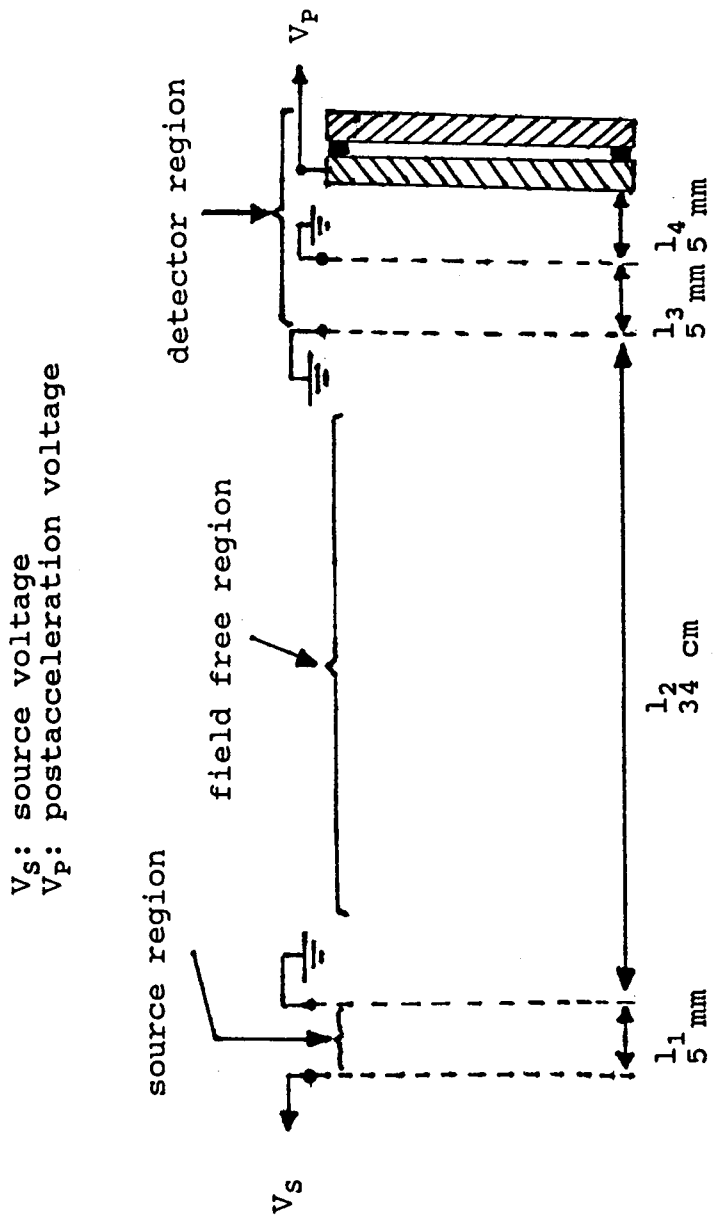

The acceleration, a, obtains from Newton's second law: $a=F/m=qV_S/ml_1$ where q is the charge state of ion. Solving equation (3-5) for t_1, yields

$$t_1 = \sqrt{\frac{2l_1}{a}} = l_1\sqrt{\frac{2m}{qV_s}} \tag{3-6}$$

After an ion passes through the grounding grid that terminates the source region, it has a velocity $v_0=(2qV_s/m)^{1/2}$. The flight time t_2 of ion passing through the electrical field free regions l_2 and l_3 is given by

$$t_2 = \frac{l_2+l_3}{v_0} = (l_2+l_3)\sqrt{\frac{m}{2qV_s}} \tag{3-7}$$

The flight time t_3 of ion passing through the postacceleration region by in front of the detector assembly is given by

$$l_4 = v_0t_3+\frac{1}{2}at_3^2 \tag{3-8}$$

Solving equation 3-8 and substituting, $a=qV_p/ml_4$ and $v_0=(2qV_s/m)^{1/2}$ yields the following for t_3:

$$t_3 = l_4\left(\sqrt{\frac{2m}{qV_p}(1+\frac{V_s}{V_p})} - \sqrt{\frac{2m}{qV_p}(\frac{V_s}{V_p})}\right) \tag{3-9}$$

where V_p is the postacceleration voltage.

The total flight time t of an ion from the ionization zone to the detector is given to the first order by

$$t = t_1+t_2+t_3 \tag{3-10}$$

For $l_2 \gg l_1$, l_3, and l_4, the expression for the total flight time t simplifies to

$$t \approx t_2 \approx l_2\sqrt{\frac{m}{2qV_s}} \tag{3-11}$$

In practice, the TOFMA program transforms the flight time spectra into mass to charge ratio spectra by using peaks of known mass to charge as calibration standards. Equation 3-11 for the flight time of an ion can be written as

$$t = A\sqrt{\frac{m}{q}} + B \tag{3-12}$$

where A and B are constants that can be determined by selecting two known peaks from the flight time spectra and giving their exact mass to charge ratio to the TOFMA

program. Figure 3-17 shows the same electron spectrum of Bi given in Figure 3-2, but with the horizontal axis calibrated in terms of mass to charge.

3-7. Secondary ion yield measurements

In section 1-2, we defined the secondary ion yield as the number of ejected secondary ions divided by the number of incident particles. In practice, only a certain fraction of ejected secondary ions can be detected. This is mainly determined by the transmission efficiency of the mass analyzer and the detection efficiency of the chevron plates. The detected secondary ion yield (Y) is given by :

$$Y = Y_0 \cdot f \cdot D \tag{3-13}$$

where Y_0 is the secondary ion yield of each sputtering event; f is the transmission coefficient of the time-of-flight mass spectrometer; and D is the detection coefficient of the chevron plates. The primary contribution to f is that only a certain fraction of the secondary ions generated from the surface of a spherical target ball can reach the detector; the other off-axis ions collide with the wall of the flight tube. Transmission of grids and stray electric fields also contribute significantly to f, but these contributions remain constant for a fixed geometry (The final important factor that influences f is the decrease in the size of the target balls over time due to evaporation losses. These effects will be discusses for various analyte matrix systems in Chapter 4. We minimize them in our ion yield experiments by limiting our recording times to 2 min or less.).

Figure 3-17: Secondary electron spectrum of Bi

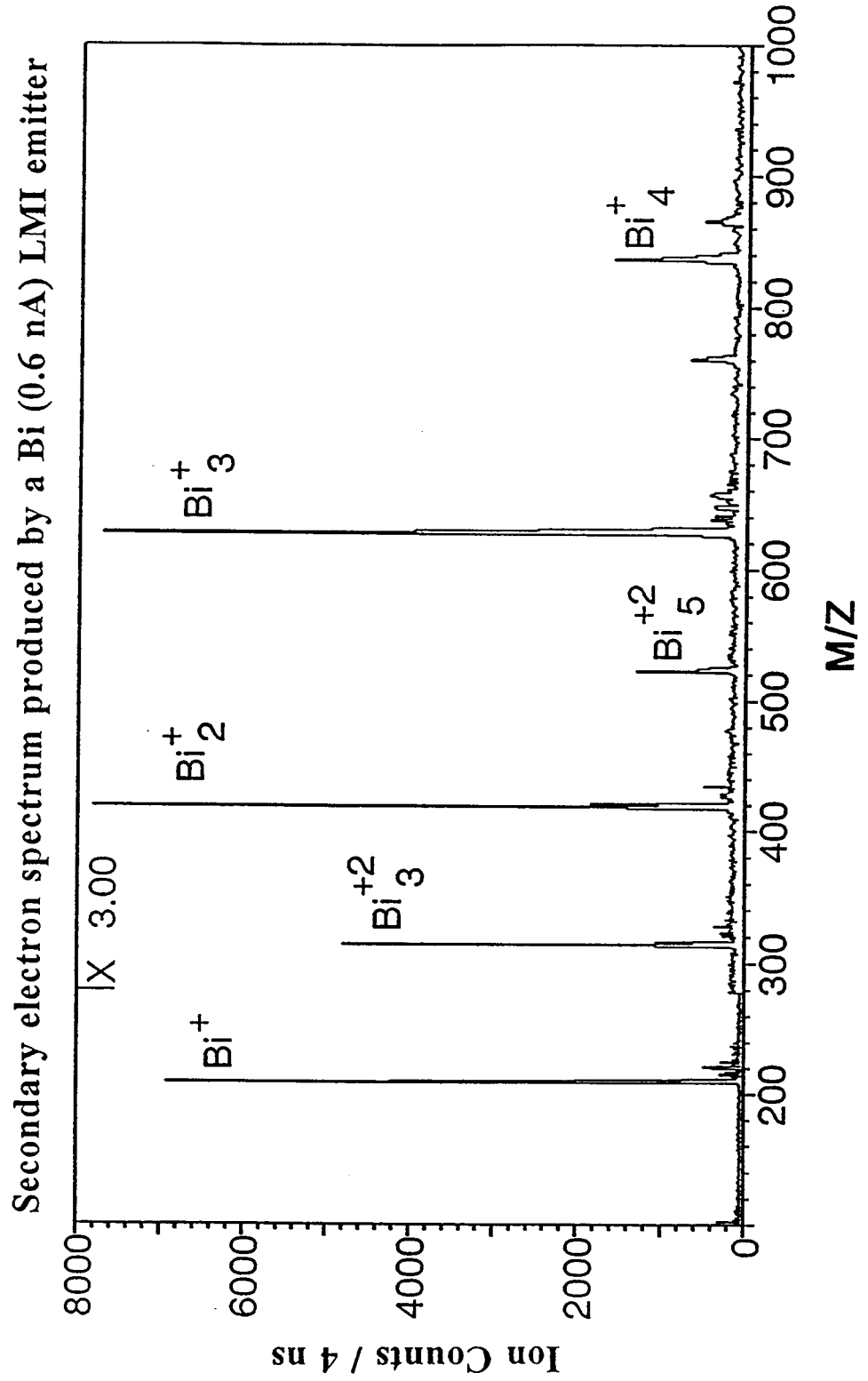

If the values of f and D can be determined then Y_0 can be estimated directly. The problem is that we can not determine universal values for f and D by experiments, for example, D varies with the mass of the detected particle and is different for each detector. We can, however, maintain f and D constant throughout the course of a series of measurements. Thus, instead of trying to determine the absolute secondary ion yield, Y_0, we can express all the data for some fixed f and D in relative terms by dividing the number of ions collected for each secondary ion species by the number of ions collected for some pre-selected secondary ion species. This quantity, which is proportional to Y_0, we will call the relative secondary ion yield, Y_R. Using the ion microscope, we can keep the diameter and the position of the target balls the same in each experiment and, in this way, keep f constant within acceptable experimental limits. For a given species and a given detector, D should vary only slowly over a period of time that is long compared to the time required to make a consistent series of measurements, e.g. 3 weeks.

As we mentioned in chapter 1, a systematic study of secondary ion yield requires ideally that one parameter at a time be changed while keeping all of the others unchanged. In our apparatus we can vary within certain limits the following properties of the primary particles: kinetic energy, charge state, mass, and incident angle of relative to the target normal. Unfortunately, the energy and the incident angle of the primary ions are not independent parameters in our experimental arrangement. A positive primary metal ion with a charge Zq accelerated by a voltage V_B in the ion gun has an

initial energy ZqV_B as it enters the secondary ion source region. Normally, the secondary ion source voltage, V_S, in our experiments is set at ±6kV, and thus, the primary ion is accelerated or decelerated in the secondary ion source region in accordance with the polarity of V_S. Since the primary ion approaches the grounded entrance grid to the secondary ion source at an angle of 45° relative to the target normal, it will be deflected off its initial path as it passes between the secondary ion source grids. The final energy of the primary ion, E_F, as it impinges on the target is given by

$$E_F = Zq(V_B - V_S) \tag{3-14}$$

, and for a primary ion initially incident at 45°, the final incident angle of the primary ion relative to the target normal is given by

$$\theta = \tan^{-1}\sqrt{\frac{V_B}{V_B - 2V_S}} \tag{3-15}$$

Figure 3-18 shows θ plotted as a function of primary ion energy for V_S=±6kV; the range of primary ion energy, 10-30 keV, is characteristic of our apparatus. From this Figure, we clearly see that as we measure the secondary ion yield as a function of the primary ion energy, we unavoidably change the incident angle of the primary ion. In order to correct for this interaction, we convert all experimental values of secondary ion yield to their corresponding values with the relation at normal incidence in accordance $Y(\theta) = Y_0(0°)(\cos\theta)^{-n}$, ($n$ = 1). Use of this inverse cosine dependency is based on the yields of deprotonated phenylalanine measured by Della-Negra et al.[38] (More recent observations by these same investigators[92] suggest that inverse cosine correction may

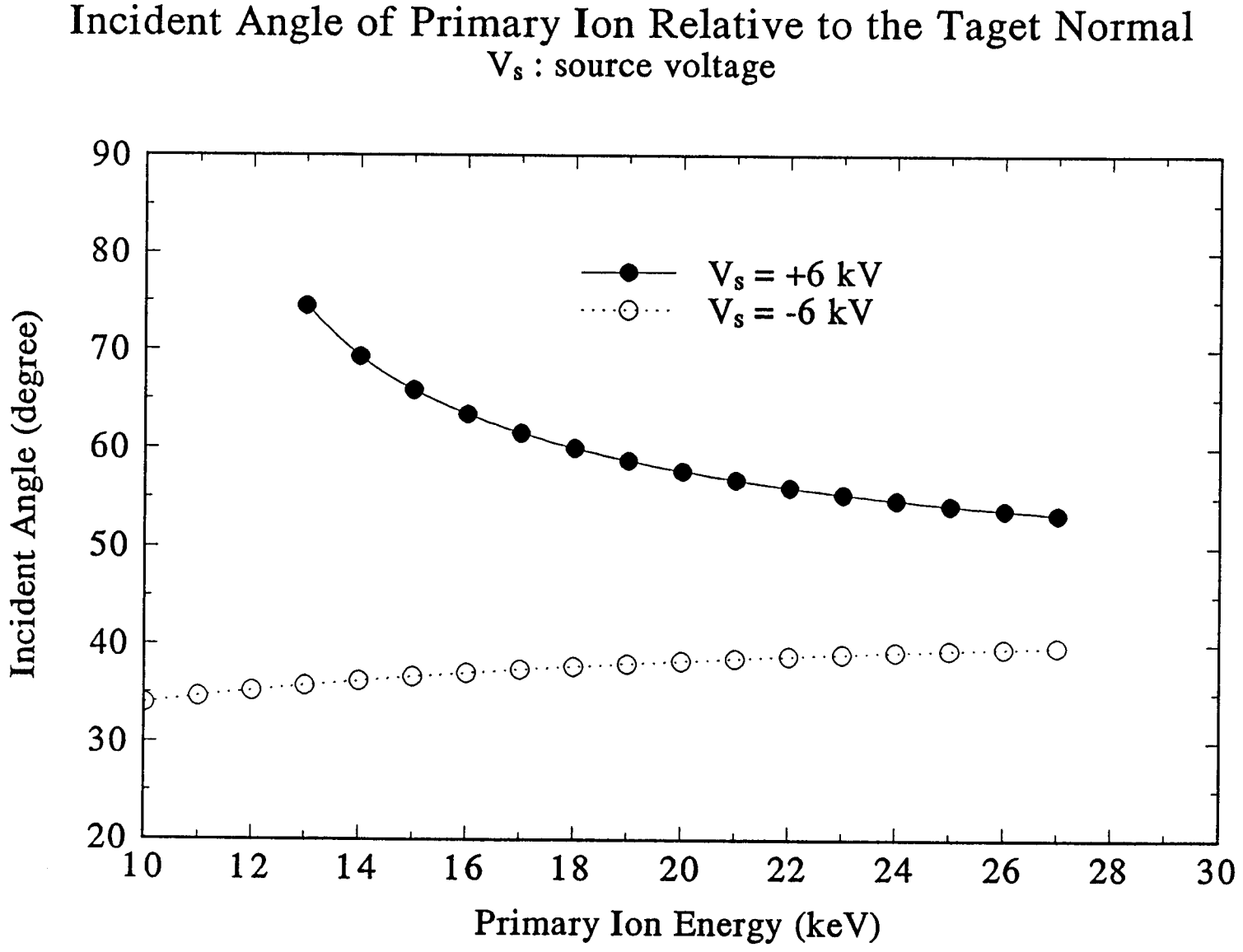

Figure 3-18: Incident angle as a function of primary ion energy

be to a high power (**n**>1).). When θ<45° (V_S=-6kV), the maximum correction factor for the angle of incidence in the primary ion energy range from 10keV to 27keV is only about 7%. For θ<45° (V_S=6kV) , this correction factor is very large, for instance, $Y(75°)= 2.5\ Y(50°)$. All of our measurements on dAMP and dGMP were performed in the negative ion mode (small correction) whereas our measurements on HDPA cation were performed in the positive ion mode (large correction).

Chapter 4

Results

4-1. Performance of the time-of-flight mass analyzer

Construction of our time-of-flight mass spectrometer began in 1988, and it was tested early in 1990. The novel features of this instrument have been discussed in chapter 3. The instrument's performance characteristics and the results obtained off it will be presented in this chapter.

In general, the performance of every type of mass analyzer can be described by three characteristics: mass range, sensitivity, and mass resolution. An ideal mass analyzer has a unlimited mass range, the ability to ionize, transport, and detect very few ions and a high mass resolving power. However, this ideal mass spectrometer does not exist yet. A time-of-flight mass analyzer has an unlimited mass range and a high sensitivity but a poor mass resolution.

4-1A. Mass range and sensitivity

Figure 4-1 shows the positive secondary ion spectrum of CsI in a glycerol matrix produced by bombardment with a 25 keV beam of In^+. This spectrum shows the cluster

Figure 4-1: Positive ion spectrum of CsI

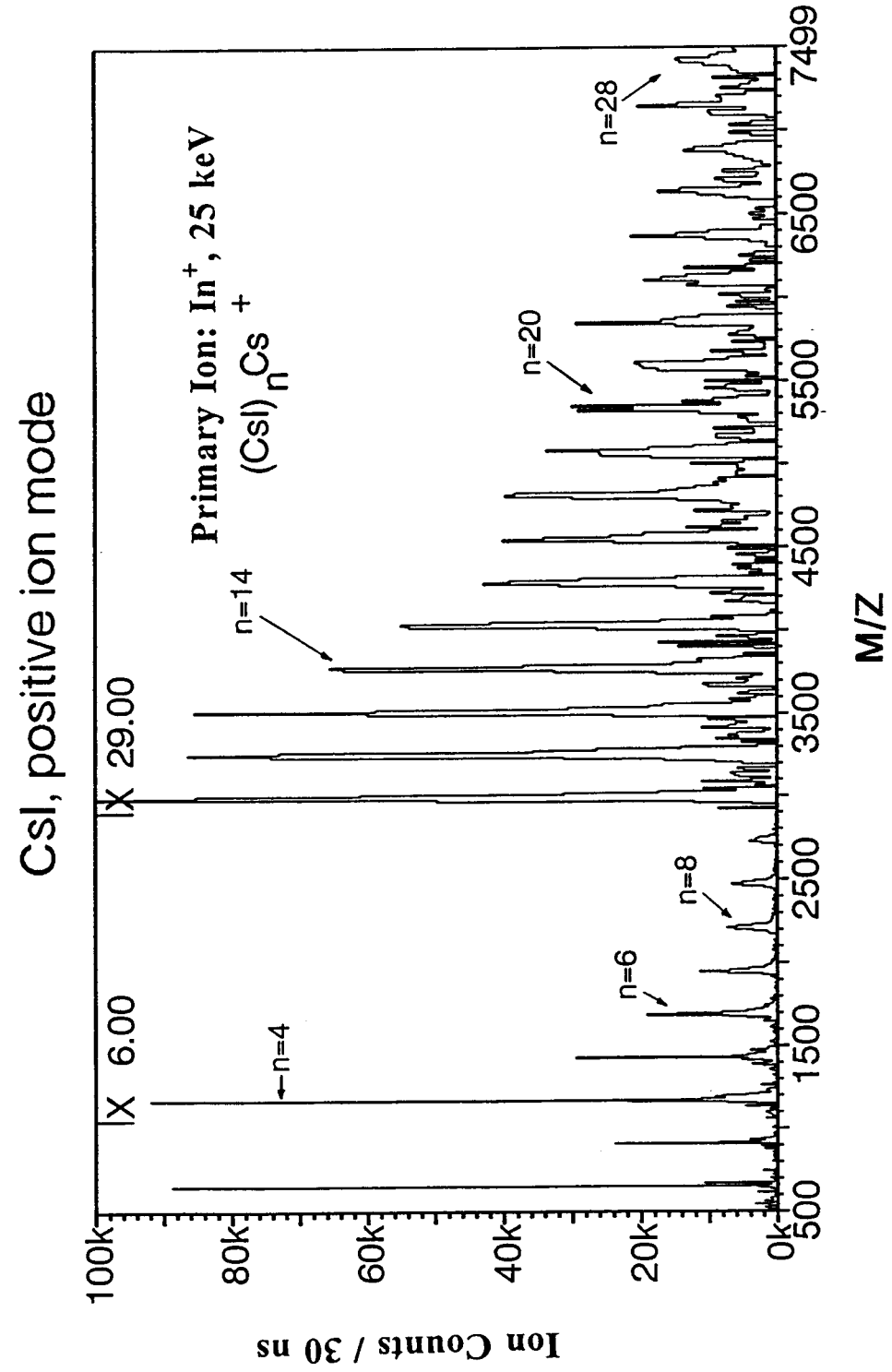

ions $(CsI)_nCs^+$ with n from 2 to 28. The mass to charge ratio of $(CsI)_{28}Cs^+$ is 7407 daltons. It is the highest mass to charge ratio produced and detected to date in our instrument.

Figure 4-2 shows the positive secondary ion spectrum of 50 fmol of gramicidin S (MW=1141.5) in a thioglycerol:glycerol (1:1) matrix (0.2 μL of a 0.287 ng/μL aqueous solution of Gramicidin S mixed with 3nL of thioglycerol:glycerol (1:1, v:v)) generated by bombardment with 25 keV In^+. This spectrum gives an indication of our time-of-flight mass analyzer's sensitivity. However, not all analytes can be detected in the femtomole range. Some of peptides, such as met-enkephalin, gramicidin D, and melittin, can only be detected in the low picomole range. The sensitivity is strongly dependent on ionization efficiency and on detection efficiency. The former is primarily a matter of matrix chemistry under particle bombardment. The latter is principally a matter of secondary electron production at the detector. As we have shown with dGMP (MW=347) in Figure 3-13, we can increase detection efficiency by increasing the kinetic energy of the secondary ions before they impact on the detector. This effect is more prominent for a larger analyte. Figure 4-3(a) shows the positive secondary ion spectrum of gramicidin S with 5kV acceleration voltage, and Figure 4-3(b) shows the positive secondary ion spectrum of gramicidin S with 7kV acceleration voltage. Figure 4-3(c) shows the positive secondary ion spectrum of gramicidin S with 7kV acceleration voltage and 6kV postacceleration voltage. The intensity of protonated gramicidin S, $(M+H)^+$, in Figure 4-3(c) is enhanced 40-fold over that in Figure 4-3(a).

Figure 4-2: Positive ion spectrum of gramicidin S (50 fmol)

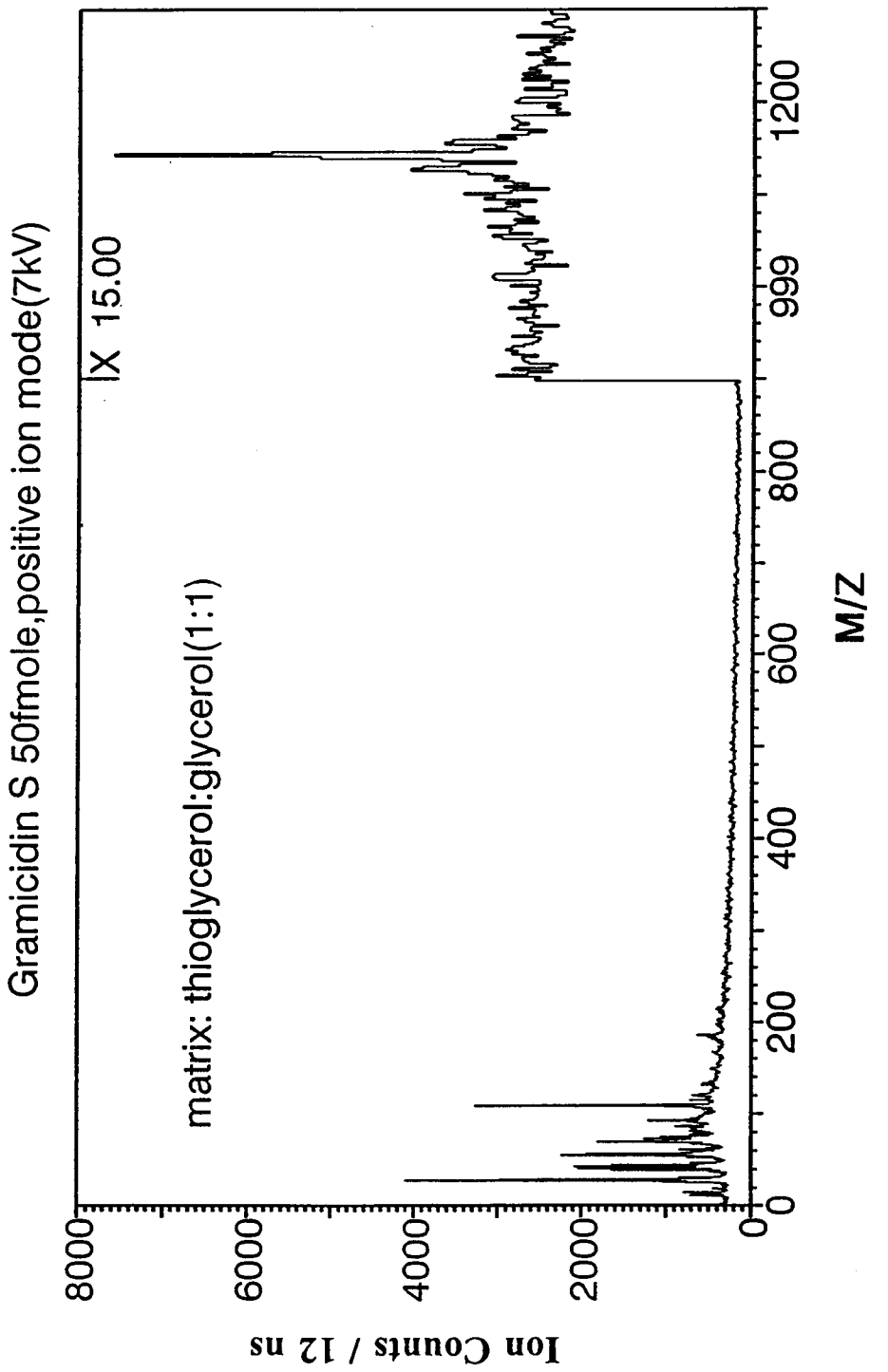

Figure 4-3: Positive ion spectrum of gramicidin S with a different internal energy: 5 keV(a), 7keV(b), and 13 keV(c)

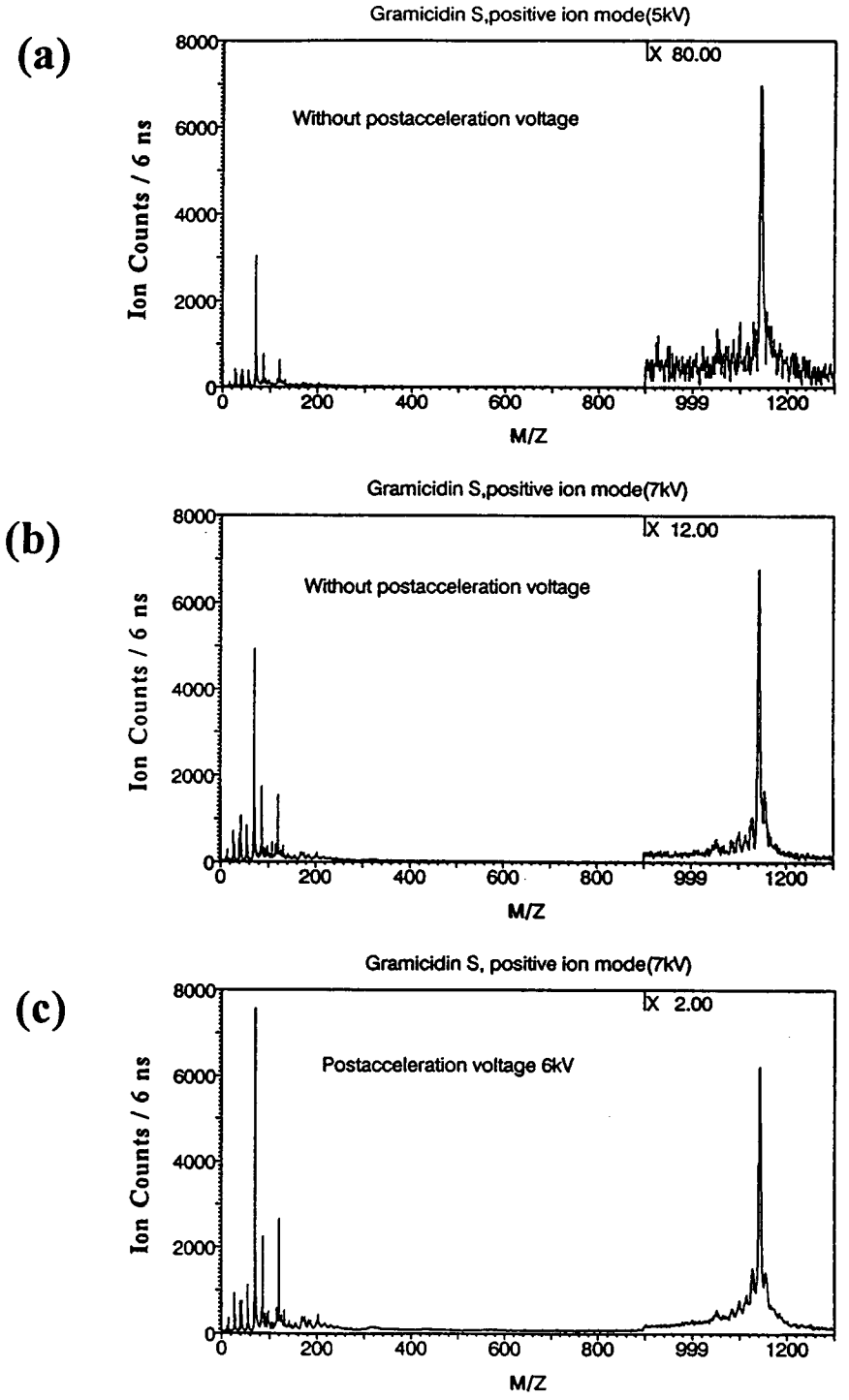

4-1B. Mass resolution

The mass resolution of a mass spectrometer is defined as $\Delta m/m$, where m is the mass of the analyzed species and Δm is some measure of the width (frequently full width at half maximum, FWHM) of the corresponding mass peak. We will use the FWHM definition in this work. The FWHM in a time-of-flight instrument is determined essentially by three factors: the time duration of the primary ion pulse, the initial axial energy spread of the secondary ion species in question, and the metastable decomposition of the secondary ion species in the electrical field free flight tube.

From equation 3-12, we know the relationship between flight time, the mass to charge ratio, and the acceleration voltage of a given secondary ion. Using differential calculus on equation 3-12, it is easily shown that the mass resolution is given by:

$$\frac{\Delta m}{m} = \frac{2\Delta t_{total}}{t} \tag{4-1}$$

where t is the total flight time of the ion in question. For a simple linear time-of-flight instrument equation 4-1 becomes

$$\frac{\Delta m}{m} = \sqrt{4\left(\frac{\Delta t_p}{t}\right)^2 + \left(\frac{\Delta \varepsilon}{E_s}\right)} \tag{4-2}$$

where Δt_p is the duration of the primary ion pulse, E_s is the kinetic energy of the

secondary ion [$E_s = qV_s = 1/2\ m(L/t)^2$], and $\Delta\varepsilon$ is the initial energy spread of the secondary ions.

In principle, the time for the primary ion pulse to sweep across a 160 μm diameter target ball should be approximately 12 ns. However, not all of the secondary ions generated from the surface of the target ball can be detected. Figure 4-4 shows the secondary ion image produced from a 160 diameter target ball. Figures 4-4(a) and 4-4(c) show the positive and the negative secondary ion images with low magnification, respectively whereas Figures 4-4(b) and 4-4(d) show the same images respectively with high magnification. From the intensity of the secondary ion images, it is clear that the secondary ions generated from the bottom part of the target ball, where the image is dim, are unlikely to reach the detector. If we estimate that the secondary ions can be detected from 50% of the total area of the target ball, Δt_p is about 6 ns.

For $(CsI)Cs^+$ (flight time ~ 8000 ns), therefore, $2\Delta t_p / t \approx 12/8000$ (= 3/2000). For a upper bound of 10 eV for the initial axial energy spread and a 6kV accelerating voltage $\Delta\varepsilon/E_S = 10/6000$ (= 1/600). Hence, the theoretical mass resolution for $(CsI)Cs^+$ is $[(1/600)^2 + (3/2000)^2]^{1/2}$ ~ 1/450 (we do not consider the metastable decay in this case.). Figure 4-5 shows that the experimental FWHM of the $(CsI)Cs^+$ peak is 10 ns. Thus, the experimental mass resolution is (from equation 4-1) 20/8000 = 1/400.

Figure 4-4: Secondary ion images from a 160 μm diameter of target ball: positive ion (a) and (b), negative ion (c) and (d)

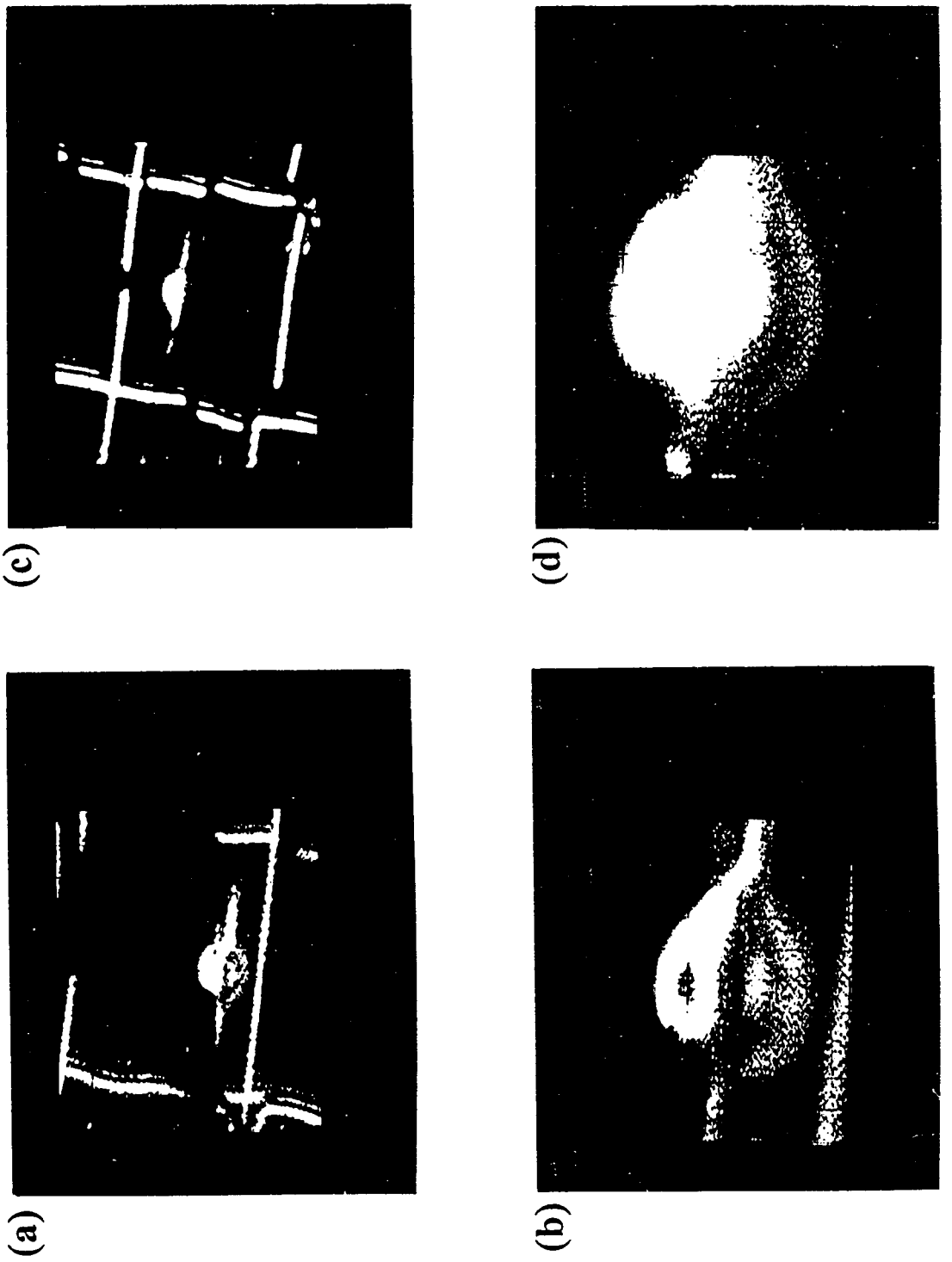

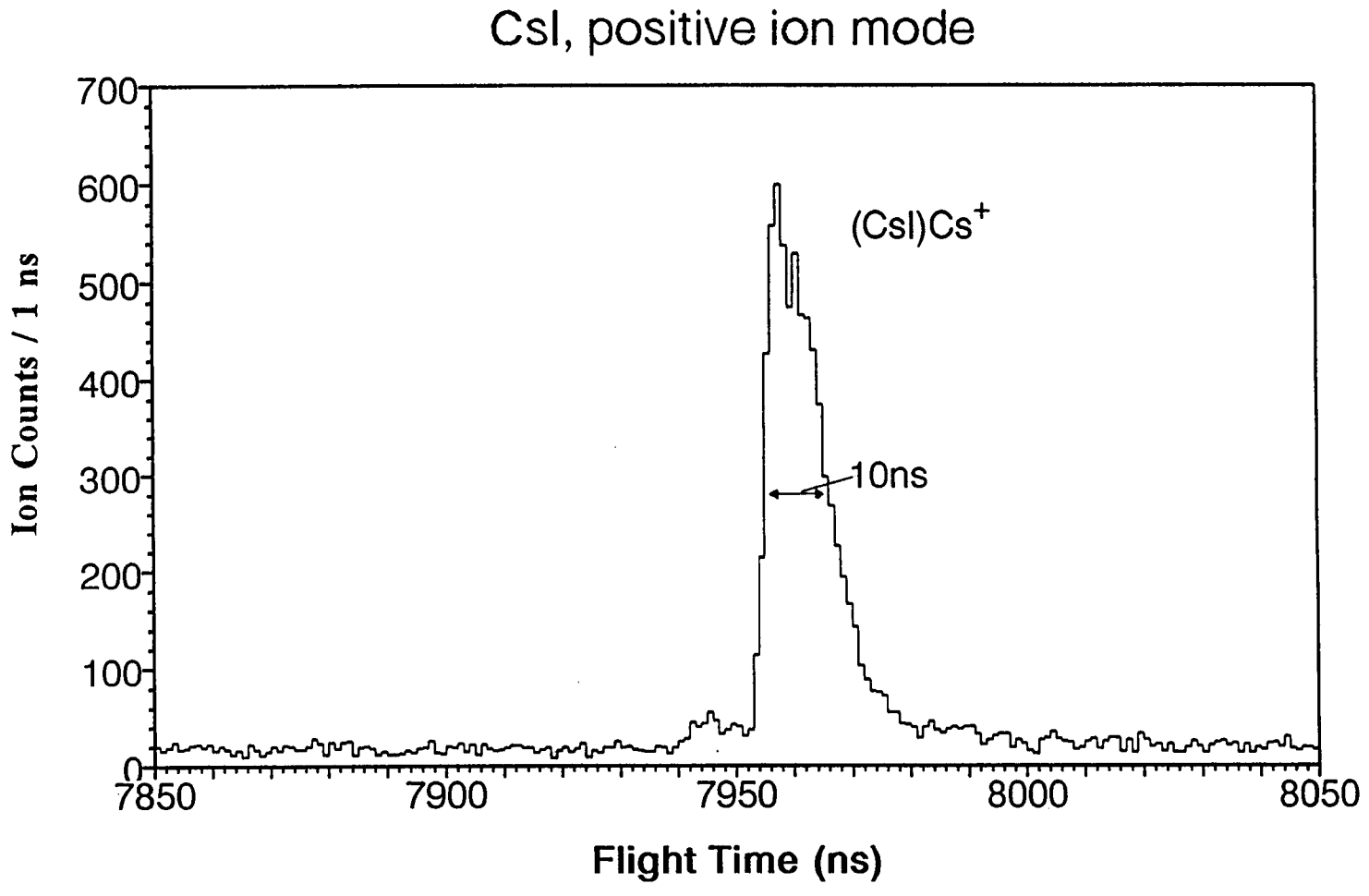

Figure 4-5: FWHM of $(CsI)Cs^+$

The metastable decay of an ion contributes to broaden the ion's peak in two ways: one is from the kinetic energy released during the decomposition; two is from the fact that the neutral decay products arrive at the detector later than the corresponding charged decay products or the stable parent ions because these latter species are postaccelerated just prior to striking the detector. Ens[25] has discussed some of the theoretical considerations of the metastable decay in his Ph.D. thesis. Figure 4-6 shows some general features of the metastable decay of 5 pmol of gramicidin S in glycerol. Figure 4-6(a) shows the positive secondary ion spectrum of gramicidin S bombarded by 25 keV In^+, in the 0° detector with the 90° ion mirror turned off. Figure 4-6(b) which was recorded on the 0° detector with the 90° ion mirror on, shows that the intensity of neutral particles from the decay of protonated gramicidin S is about 1/11 the intensity of the sum of the decayed and the undecayed secondary ions. Figure 4-6(c) shows the ion spectrum of gramicidin S in the 90° detector with the 90° ion mirror on. A quantitative comparison between the nondecayed protonated gramicidin S and its neutral decay products is difficult since it requires two identical detectors. In this dissertation, we will not focus on metastable phenomena; the question of sensitivity is a more important consideration for our study of secondary ion emission.

4-2. Secondary ion spectra of liquid matrices

In this section, we are going to present some of the qualitative features of the secondary ion spectra from the liquid matrices bombarded by different species of

Figure 4-6: Positive ion spectrum of gramicidin S : without activated ion mirror (a), neutral particles detected from 0° detector (b), and reflected ions detected from 90° detector (c)

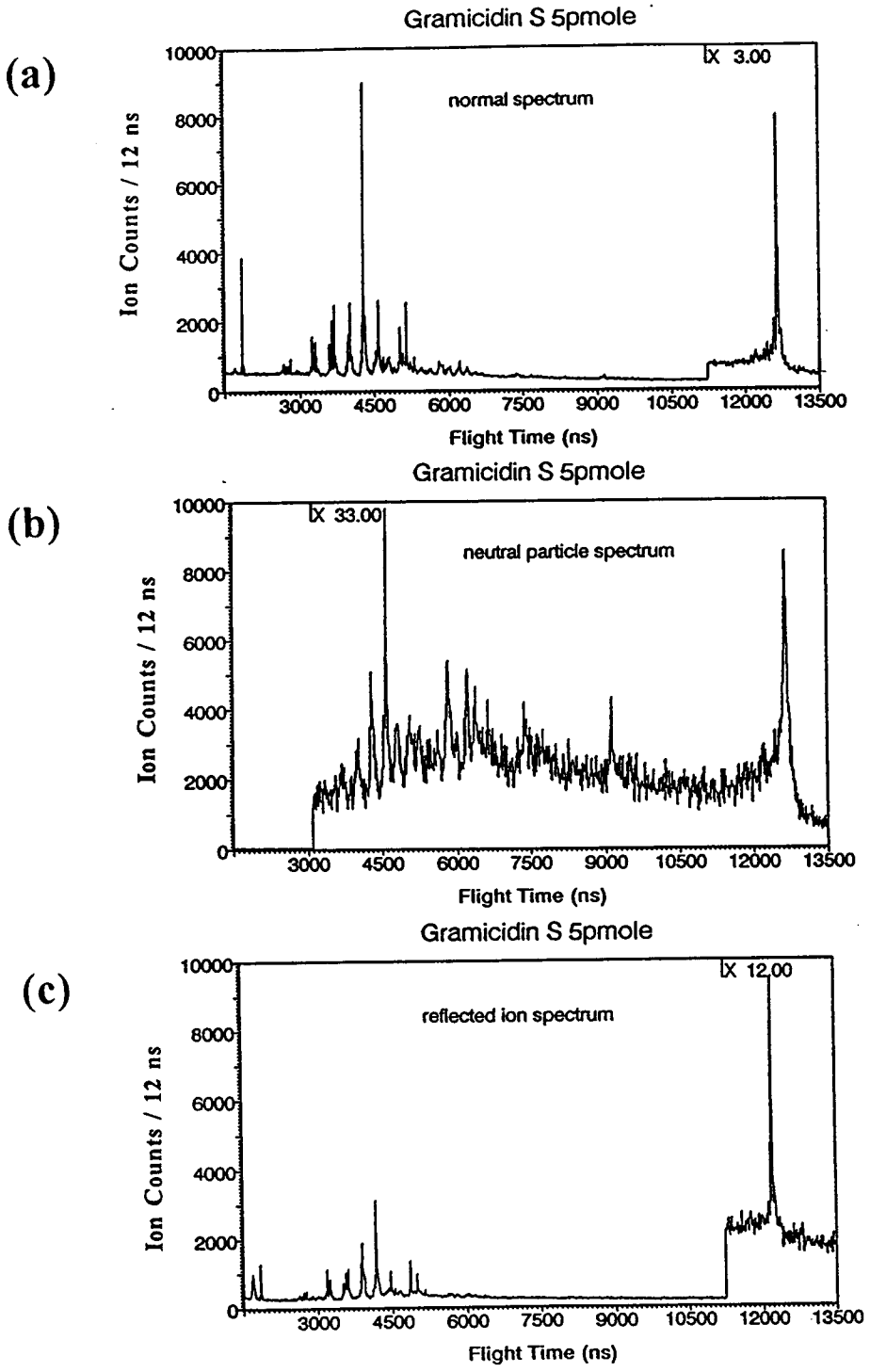

primary ions Figure 4-7 (a) and (b) show respectively the positive secondary ion spectra of glycerol and thioglycerol:glycerol (1:1) produced by bombardment with 25 keV In^+. Figure 4-8(a), (b), and (c) show respectively the negative secondary ion spectrum of glycerol generated by bombardment with 1.2nA of 25keV In^+, by bombardment with 0.7 nA of 25keV Au^+, and by bombardment with 0.5nA of 25keV Bi^+. In the positive secondary ion spectra, protonated glycerol $(glycerol+H)^+$, protonated diglycerol $(2glycerol+H)^+$, and proton $(H)^+$ peaks are dominant while, in the negative secondary ion spectra, deprotonated glycerol $(glycerol-H)^-$, deprotonated diglycerol $(2glycerol-H)^-$, and hydride $(H)^-$ peaks are dominant. From these spectra, it is clear that essentially the secondary ion species are generated by bombardment with different species of primary ions all having the same energy. The intensity of the secondary ion of an analyte under bombardment with a primary ion of heavier mass is stronger than those from produced by bombardment with a primary ion of lower mass in the same primary ion beam current.

4-3. Doped cation experiments

From equation 2-1, we know the kinetic energy, T, transferred from the incident particle to the target atom. We can rewrite the expression for T as a function of M_1/M_2 Taking derivative of T with respect to M_1/M_2, yields

Figure 4-7: Positive ion spectra of glycerol (a), and of thioglycerol (b)

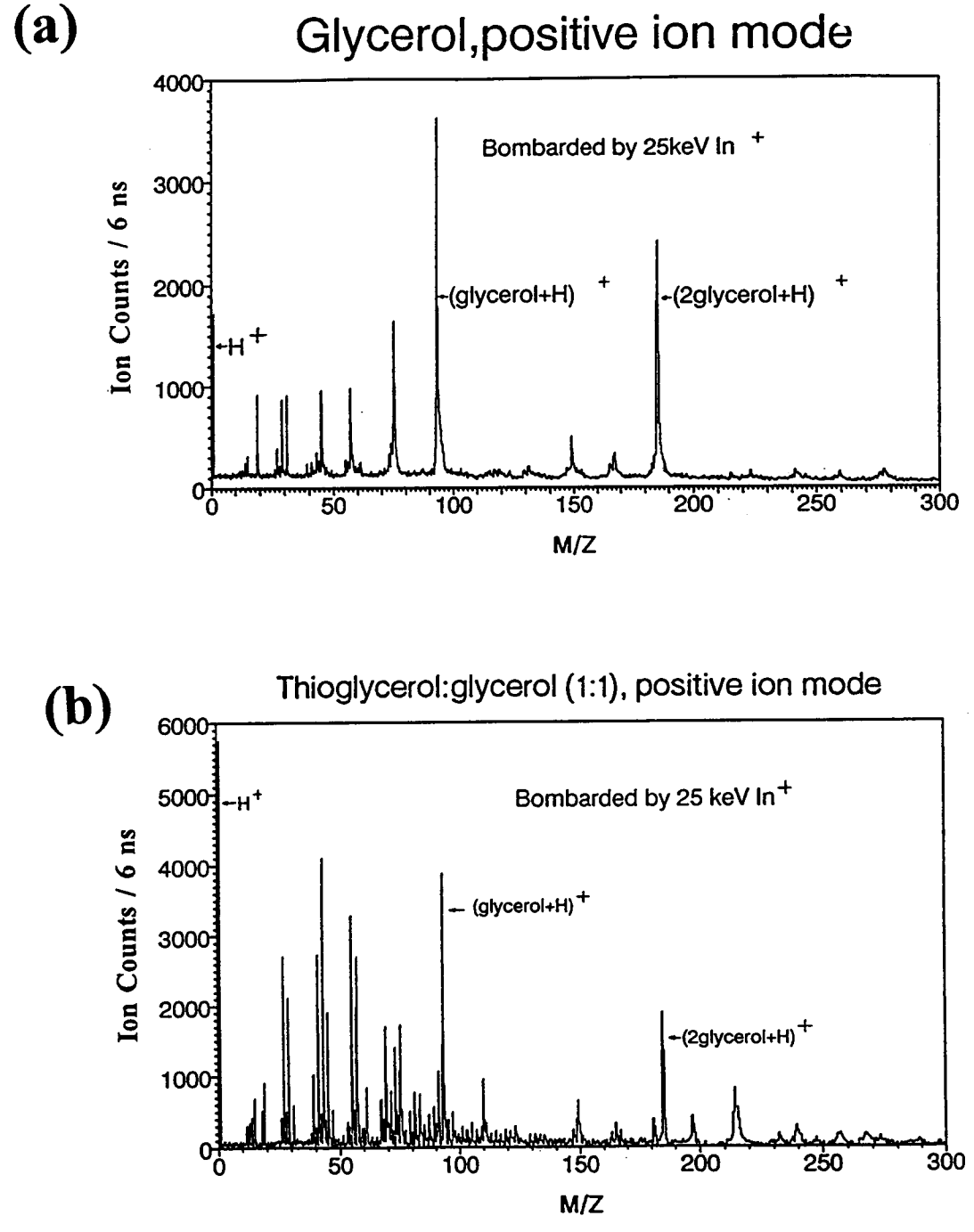

Figure 4-8: Negative ion spectra of glycerol bombarded by 25 keV of In^+ (1.2 nA) (a), of Au^+ (0.7 nA) (b), and of Bi^+ (0.5 nA) (c)

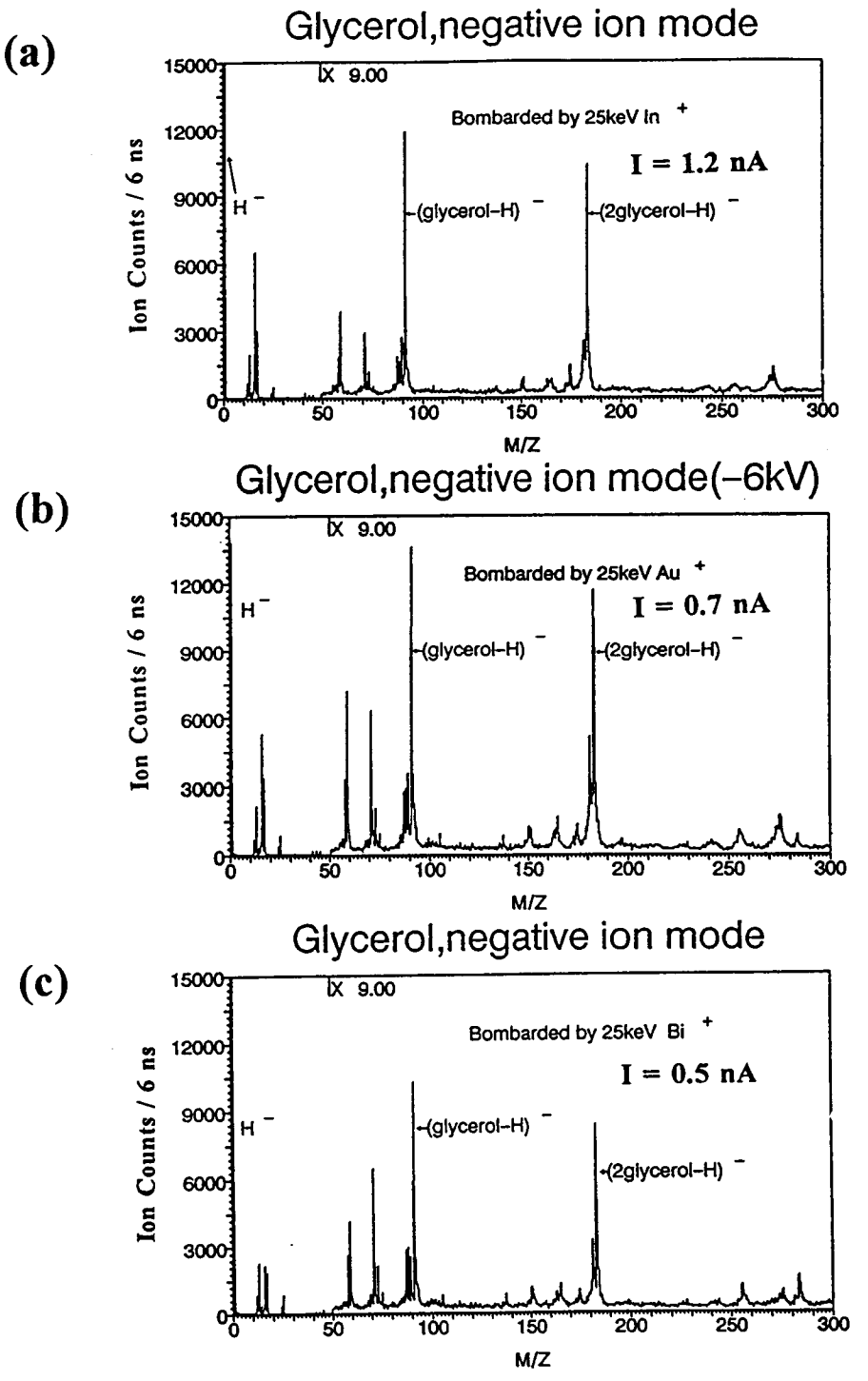

particle to the target atom. We can rewrite the expression for T as a function of M_1/M_2

$$T\left(\frac{M_1}{M_2}\right) = \frac{4\frac{M_1}{M_2}}{\left(\frac{M_1}{M_2}+1\right)^2} E_0 \sin^2\frac{\theta}{2} \quad . \tag{4-3}$$

Taking derivative of T with respect to M_1/M_2, yields

$$\frac{dT}{d\left(\frac{M_1}{M_2}\right)} = \frac{4\left(1-\frac{M_1}{M_2}\right)}{\left(\frac{M_1}{M_2}+1\right)^3} E_0 \sin^2\frac{\theta}{2} \quad , \tag{4-4}$$

which clearly shows the well known result that $T(M_1/M_2)$ has a maximum for any scattering angle θ when $M_1=M_2$.

Organic analytes are mostly composed of H, O, and N atoms which are relatively small in comparison with the primary ions used in this study. In order to increase the kinetic energy transferred from a primary beam of In^+ to the target, we doped a matrix of thioglycerol:glycerol (1:1) with $Cd(NO_3)_2 \bullet 4H_2O$. The dopant, which is water soluble, contains a large number of Cd atoms whose mass, 112.4, clearly matches that of the incident In particle, 114.8. Hence, the kinetic energy transferred from the incident In^+ to Cd atoms in the target should be optimal.

Figure 4-9(a) shows the positive secondary ion spectrum of met-enkephalin in a thioglycerol:glycerol (1:1) matrix bombarded by 25keV In^+. Figure 4-9(b) show the

Figure 4-9: Positive ion spectra of met-enkephalin: from thioglycerol:glycerol (1:1) matrix (a), from matrix doped with 32 μg/μL $Cd(NO_3)_2 \cdot 4H_2O$ (b), and from matrix doped with 100 μg/μL $Cd(NO_3)_2 \cdot 4H_2O$ (c)

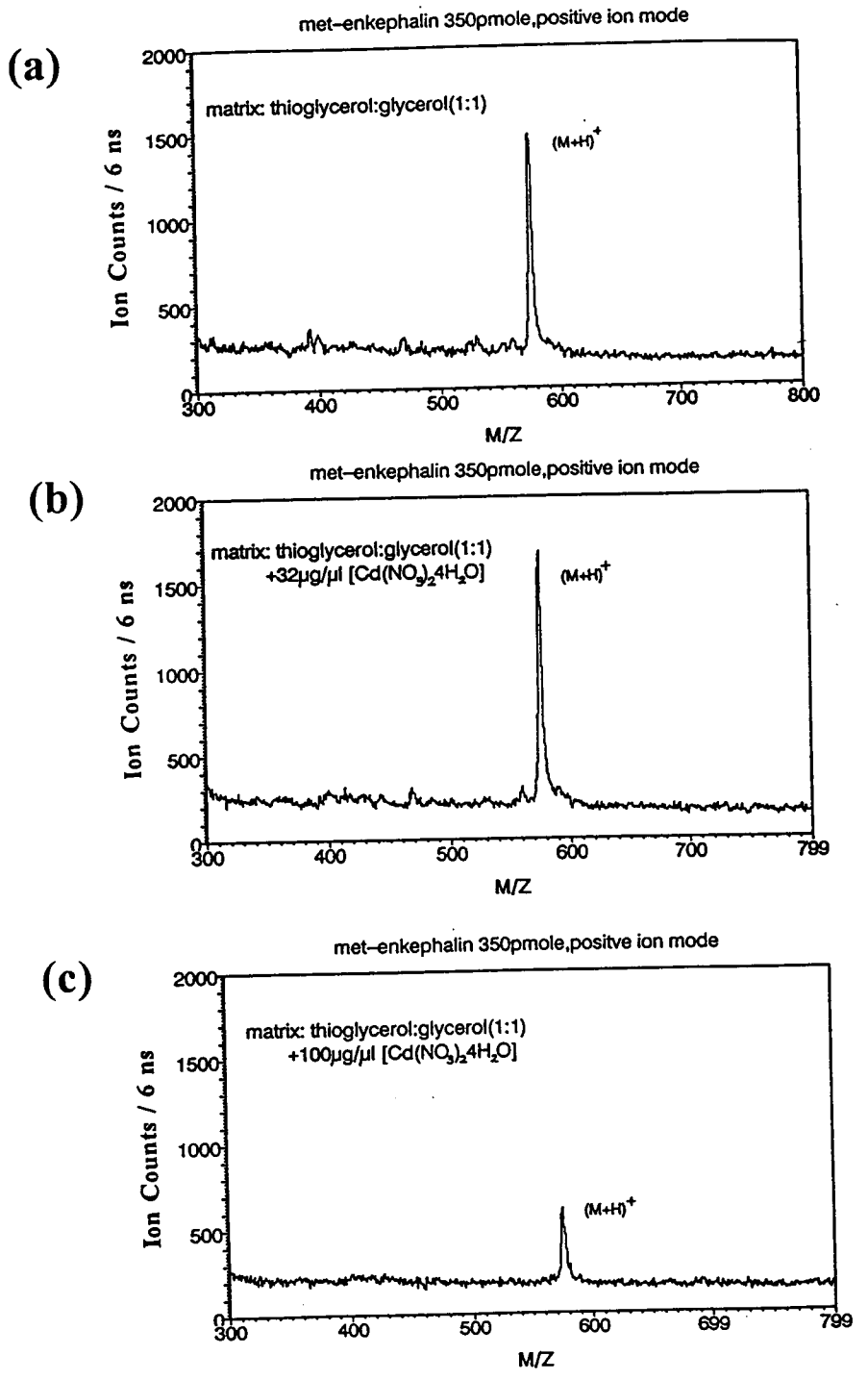

by the doping with Cd. However, this enhancement does not exist if the concentration of $Cd(NO_3)_2 \cdot 4H_2O$ is increased over 50 μg/μl. Figure 4-9(c) shows that, the matrix is doped at a concentration of 100 μg/μl $Cd(NO_3)_2 \cdot 4H_2O$, the intensity of the protonated met-enkephalin $(M+H)^+$ is dramatically decreased. The yield* of protonated met-enkephalin as a function of the concentration of $Cd(NO_3)_2 \cdot 4H_2O$ is shown in Figure 4-10. The yield of protonated met-enkephalin has a maximum at the $Cd(NO_3)_2 \cdot 4H_2O$ concentration of 30 μg/μl. A similar result was obtained for the yield of protonated met-enkephalin when the matrix was doped with $InCl_3 \cdot 4H_2O$.

These experiments suggest that the physical processes of energy transfer are responsible for the enhancement in the yield of protonated met-enkephalin when the doped concentration of $Cd(NO_3)_2 \cdot 4H_2O$ in the matrix is lower than 30 μg/μl. They further suggest that chemical interactions between the dopant and the analyte (met-enkephalin) become dominant over the physical processes when the concentration of doped $Cd(NO_3)_2 \cdot 4H_2O$ is over than 30 μg/μl. Further investigation of these phenomena were not carried out in this study.

*The secondary ion yield in our measurements is calculated as a dimensionless relative yield by normalizing the integral area of the protonated met-enkephalin peak with its maximum of all the spectra. The absolute yield in our measurements can not be exactly determined because the detection efficiency of the detector and transmission factor of the instrument are unknown.

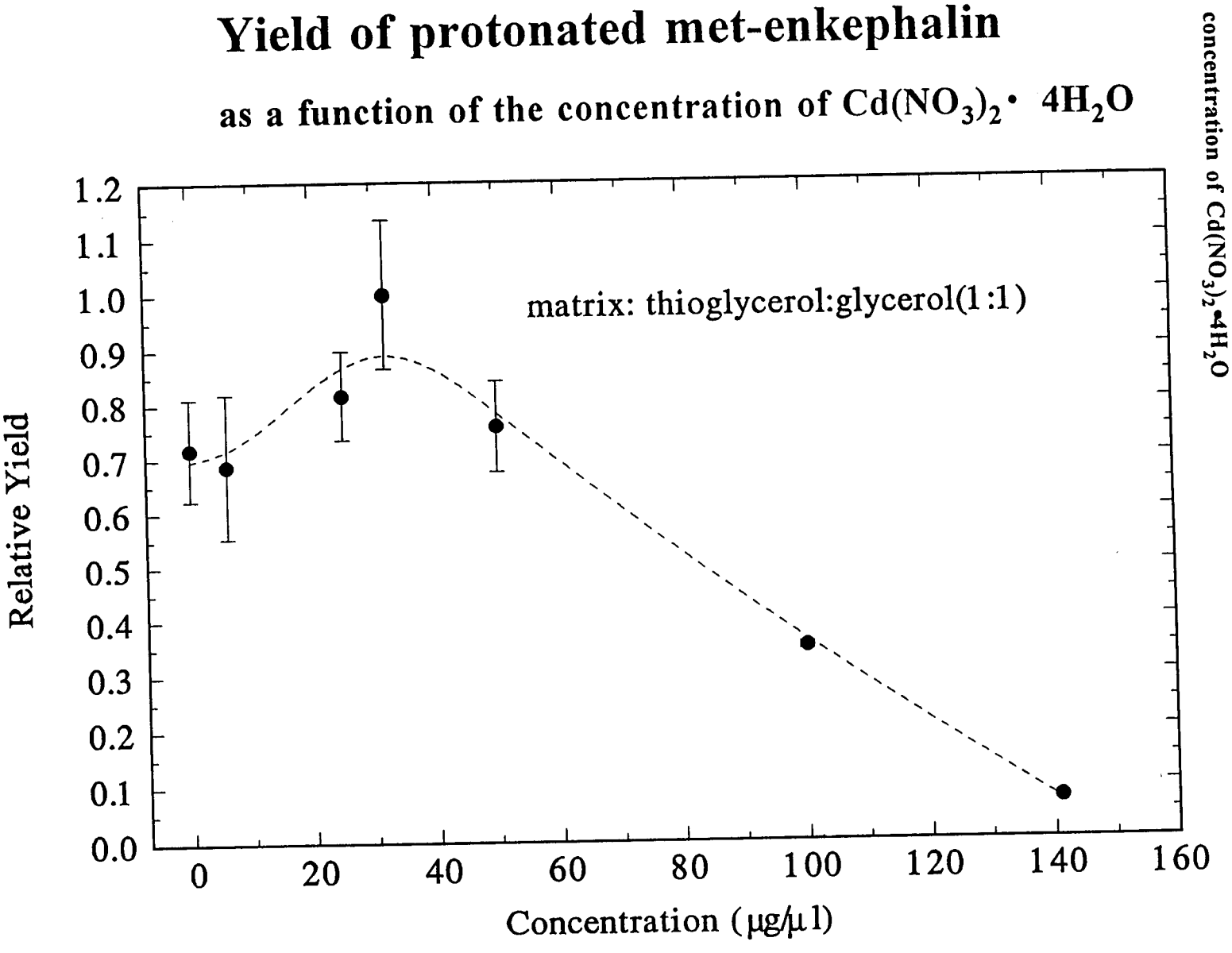

Figure 4-10: Yields of protonated met-enkephalin as a function of the concentration of $Cd(NO_3)_2 \cdot 4H_2O$

4-4. Secondary ion yield of amino acids

It has been proposed by several investigators that the secondary ion yield of an analyte from a liquid matrix varies with the concentration of analyte on the surface of the target and with the interaction between the analyte and the liquid matrix. It is difficult to quantitatively define the surface condition of a liquid target let alone to try to interpret the results of the secondary ion yield measurements from such targets. Some of this difficulty is illustrated in Figures 4-11(a), (b), and (c), in which the positive secondary ion spectra (primary ion = 25 keV In^+) of 7 pmol of alanine in glycerol recorded at different times after introduction into vacuum, are shown. During the first minute after the target has been inserted into the mass spectrometer (Figure 4-11(a)), protonated alanine and protonated glycerol ions are dominant; the dimer peak are also intense. About 10 minutes later (Figure 4-11(b)), the protonated glycerol peak and dimer peaks have almost disappeared, but the protonated alanine peak remains fairly strong in the spectrum. Figure 4-11(c) shows the spectrum collected 16 minutes after insertion. The protonated alanine still exists in the spectrum but the intensity is about 3 times smaller than in Figures 4-11(a) and 4-11(b). Figures 4-12(a), (b), and (c) show the secondary ion spectra of 700 fmol alanine bombarded by 25keV In^+ recorded at different times after introduction into the instrument. This series of spectra clearly indicates that the intensity of the protonated glycerol decreases with increasing time in vacuum while the intensity of the protonated alanine increases with increasing time in vacuum. These results are summarized in Figures 4-13(a) and (b), which show the

Figure 4-11: Positive ion spectra of 7 pmol alanine in glycerol as a function of residence time in vacuum: 1 min (a), 10 min (b), and 16 min (c)

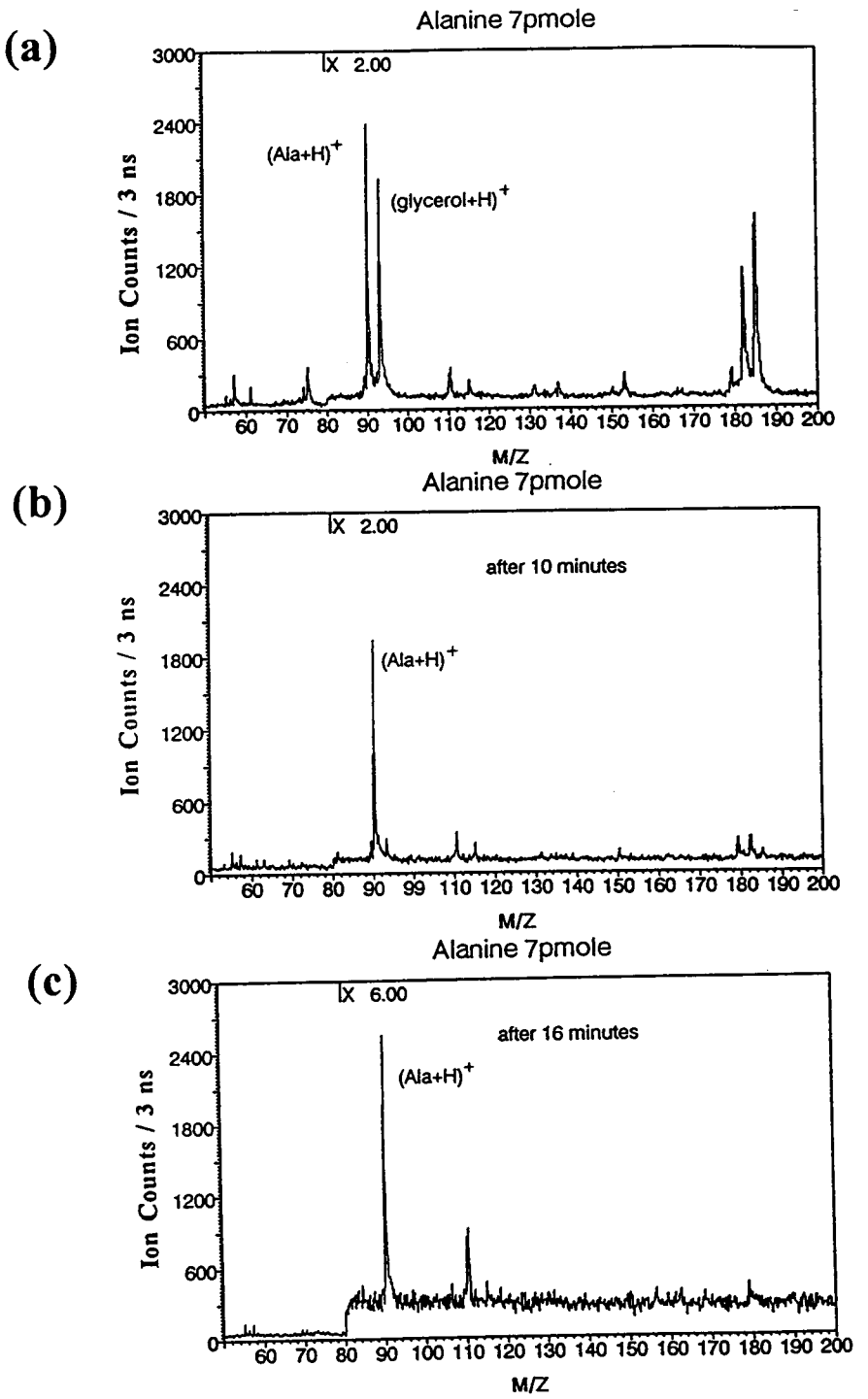

Figure 4-12: Positive ion spectra of 700 fmol alanine in glycerol as a function of residence time in vacuum: 1 min (a), 10 min (b), and 16 min (c)

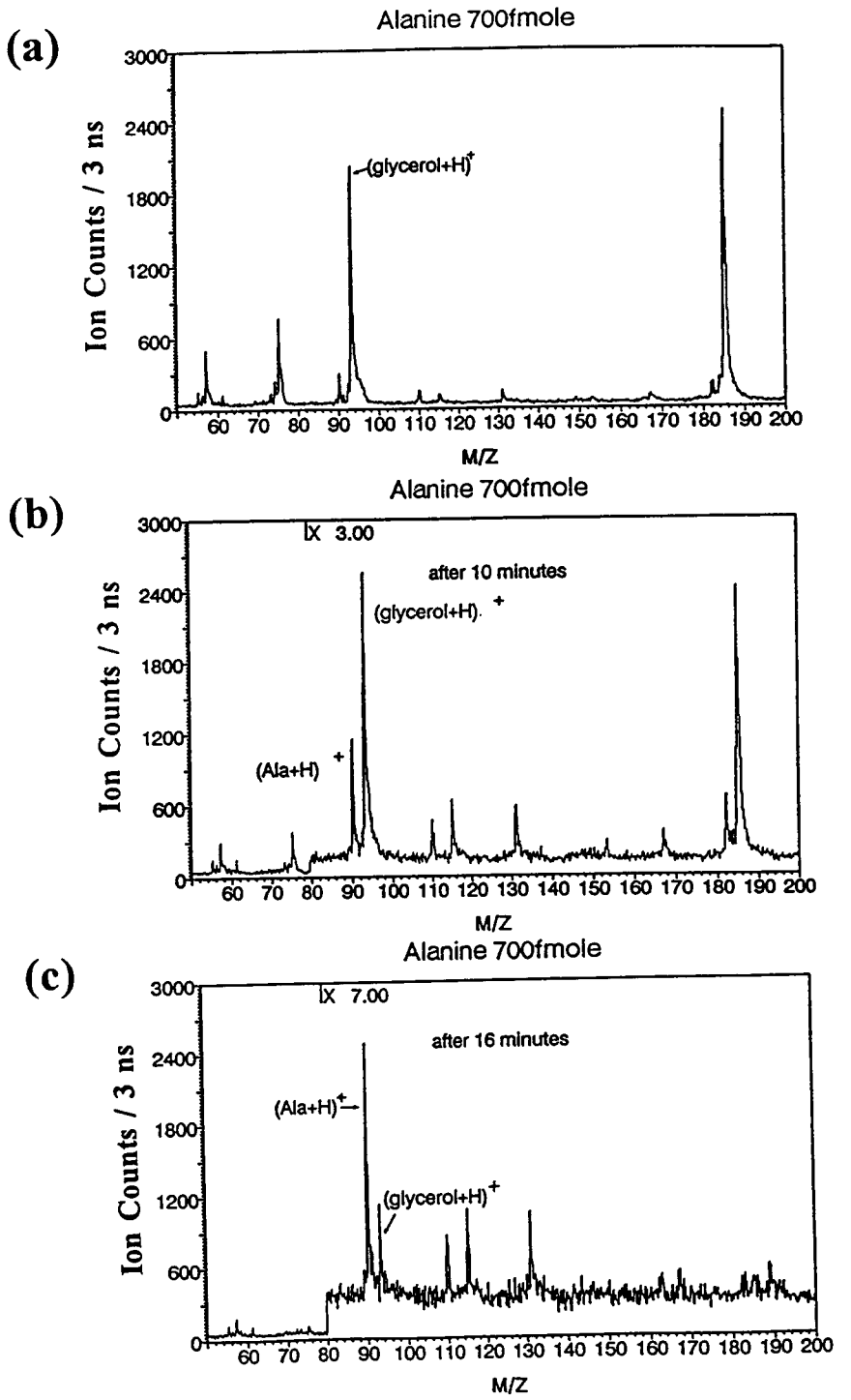

Figure 4-13: Yields of protonated alanine as a function of residence time in vacuum(a), and yields of protonated alanine as a function of target diameter (b)

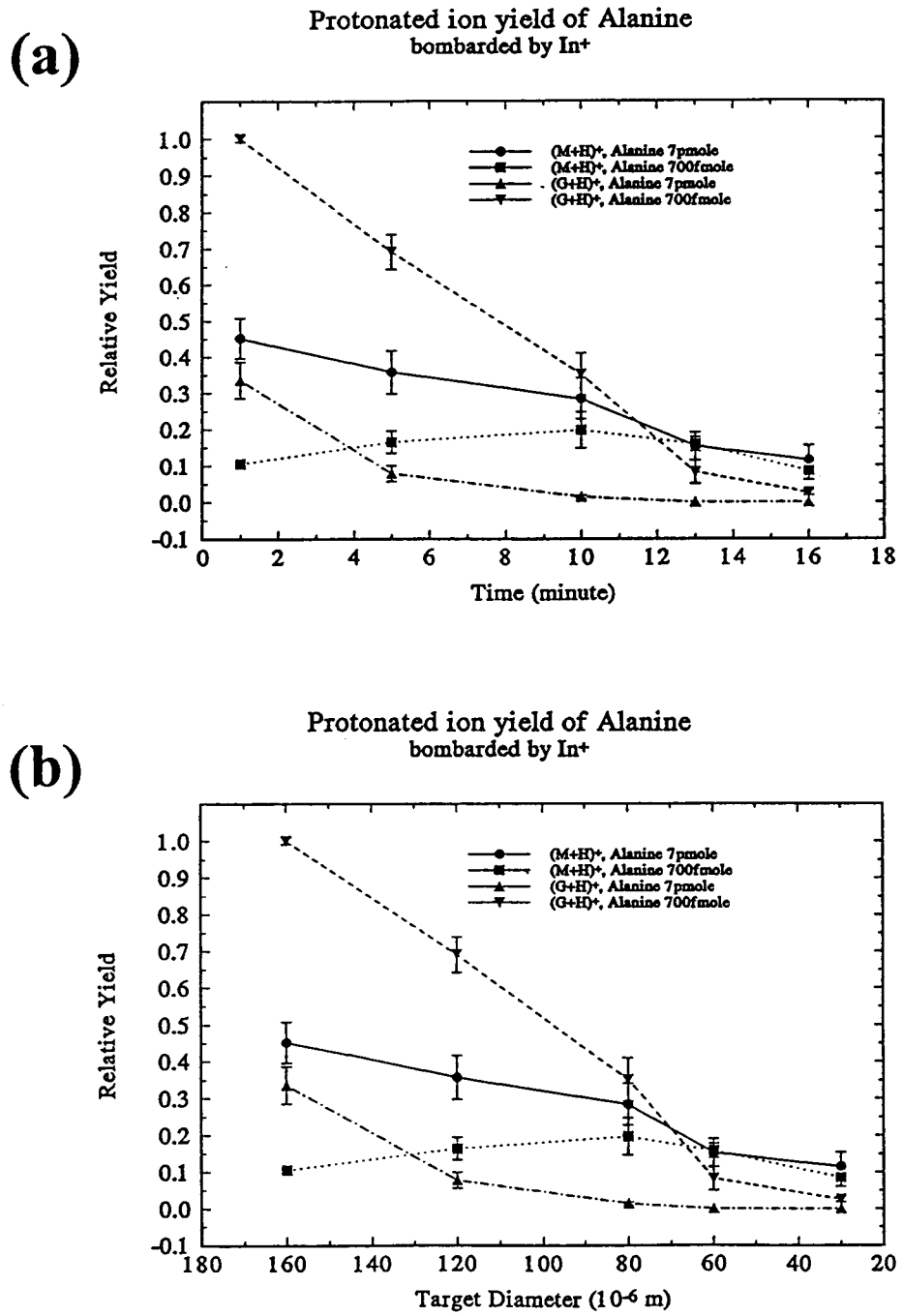

yields of protonated alanine and glycerol as a function of the vacuum residence and as a function of target's diameter, respectively. Similar results have also been observed for leucine in a glycerol matrix.

This result is significant because the diameter of target ball decreases over time in the vacuum system due to the evaporation of the glycerol matrix. We expect that the intensity of secondary ion should be decreased when the diameter of target is reduced because the ionization zone of the target also decreases. However, this intuition can not employ in case of 700 fmol alanine in the glycerol matrix (Figure 4-13(b)). The possible explanation of this effect is that the concentration of alanine at the surface of the target increases when the diameter of the target decreases. On the other hand, the concentration of alanine on the surface of the glycerol matrix in the case of 7 pmol alanine is saturated. This explains why protonated alanine (Figure 4-13(b)) decreases with the decreasing of the diameter of the target ball.

4-5. Secondary ion yield of nucleosides and nucleotides.

Nucleosides and nucleotides are an important group of biomolecules and are the basic building blocks of the biopolymeric ribonucleic acids (RNA) and deoxyribonucleic acids (DNA). Nucleotides are made by combining nitrogenous heterocyclic rings, sugars, and phosphate groups. A nucleotide without phosphate groups is called nucleoside. The nitrogenous heterocyclic rings of nucleosides and nucleotides are

referred as the bases (B, in the notation of our spectra) of the nucleotides or the nucleosides.

We have extensively measured the secondary ion yields of nucleosides and nucleotides from glycerol matrices bombarded with different species of primary ions. Figures 4-14(a) and (b) show the positive secondary ion spectra respectively for the nucleosides deoxyadenosine (dA) and deoxycytidine (dC) produced by bombardment with 25keV In^+. Figures 4-15(a) and (b) show the spectra respectively for the nucleosides deoxyguanosine (dG) and thymidine (T) generated the same way. The protonated nucleoside $(M+H)^+$ and base ion $(B+2H)^+$ dominate in all four spectra. Figure 4-16 show the relative yields (the relative yields are calculated by dividing the yield of a given species by the yield of protonated deoxyadenosine) of protonated nucleosides from 160 pmol of analyte bombarded by 25keV In^+ and Bi^+. The yields of protonated nucleosides clearly vary with the species of nucleoside and are clearly larger for the more massive primary ion, Bi^+, in comparison with the less massive primary ion, In^+. Figures 4-17(a) and (b) show comparable positive secondary ion spectra respectively for the nucleotides dAMP and dCMP produced by bombardment with 25keV In^+. Figures 4-18(a) and (b) show them respectively for the nucleotides dGMP and TMP produced under the same condition. Figure 4-19 shows the yields of the protonated nucleotides generated by bombardment with 25keV In^+ and 25 keV Bi^+. These results are similar to that (Figure 4-16) for the nucleosides.

Figure 4-14: Positive ion spectra of nucleosides in glycerol: deoxyadenosine (a), and deoxycytidine (b)

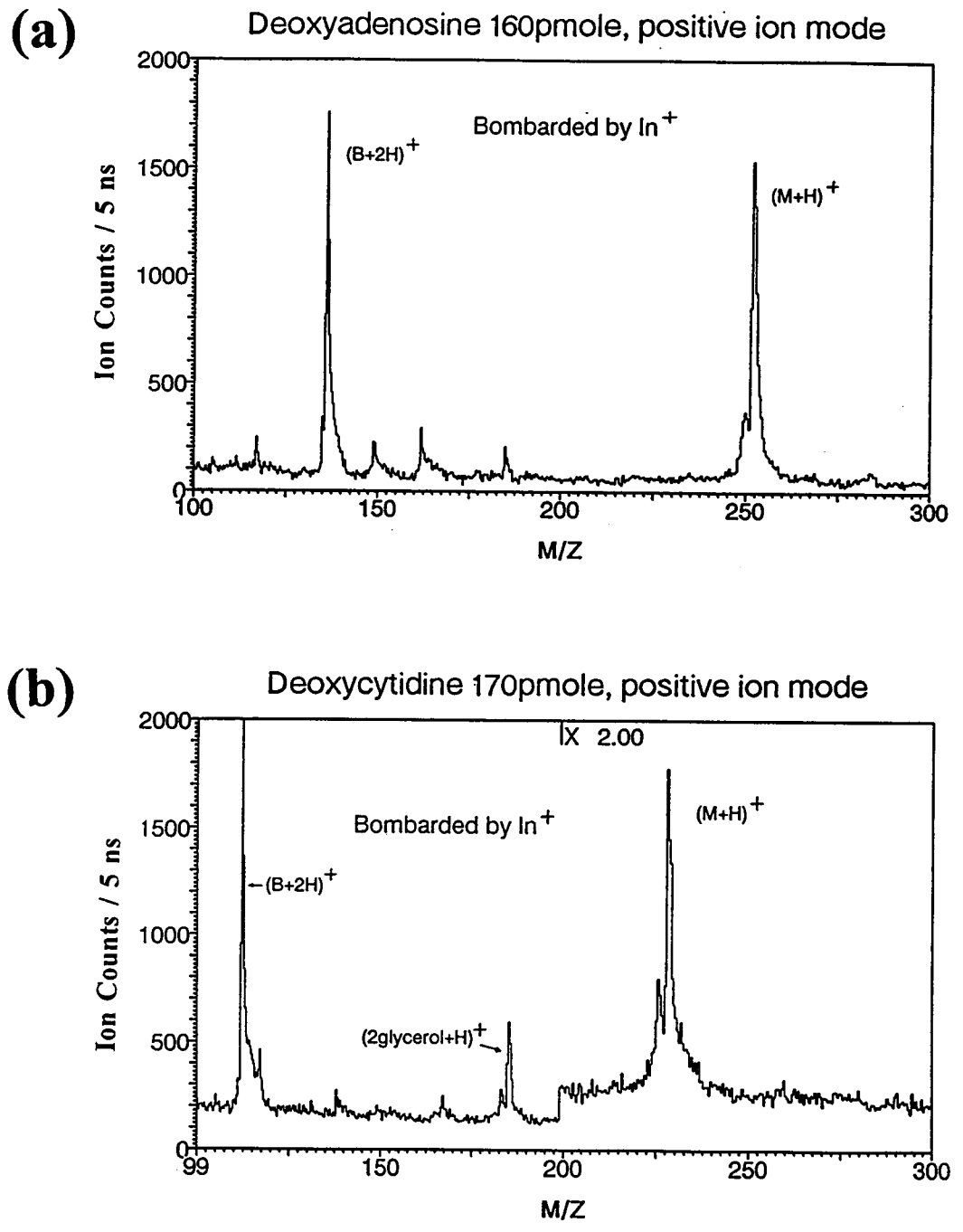

Figure 4-15: Positive ion spectra of nucleosides in glycerol: deoxyguanosine (a), and thymidine (b)

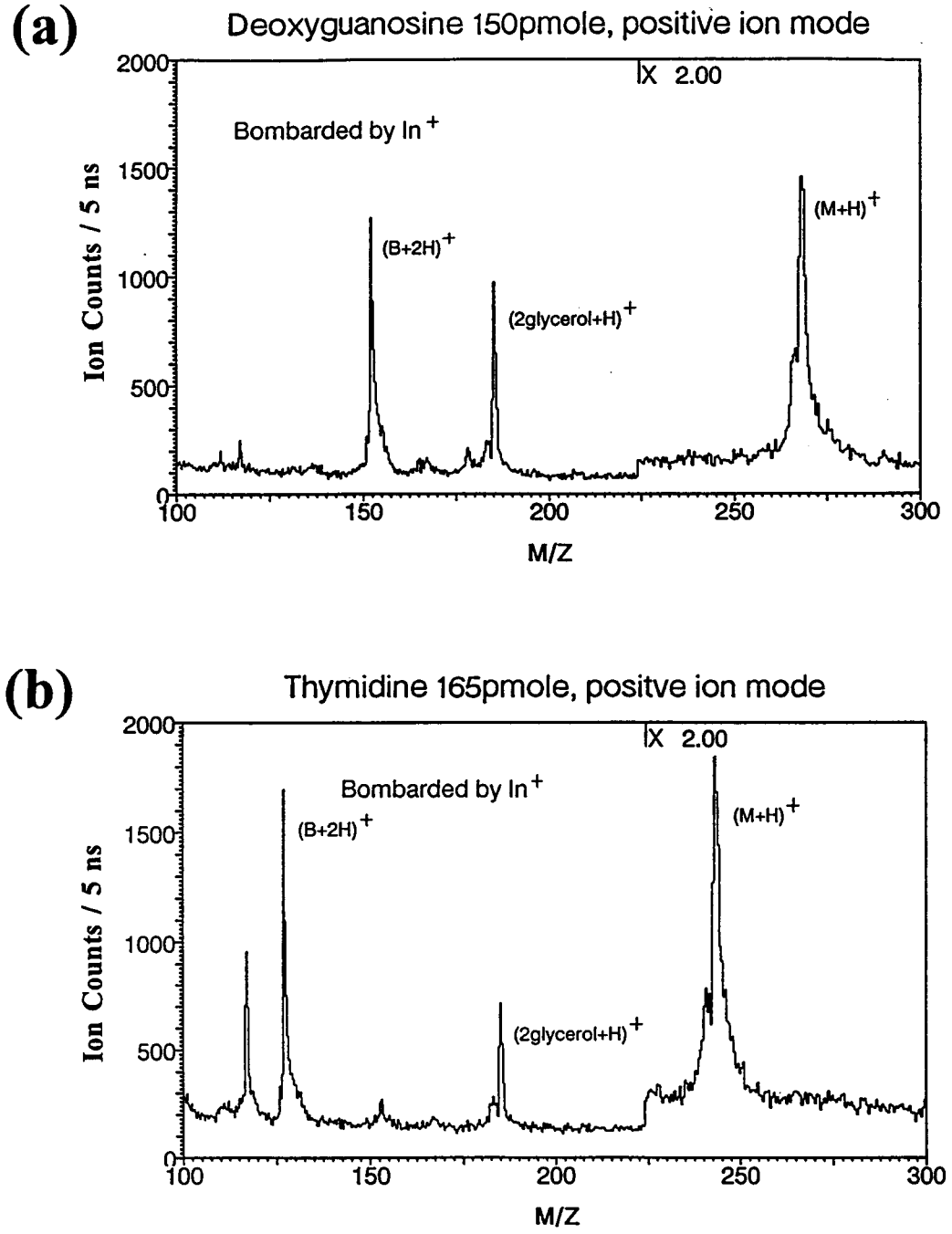

Figure 4-16: Yields of protonated nucleosides bombarded by 25 keV In^+, Bi^+

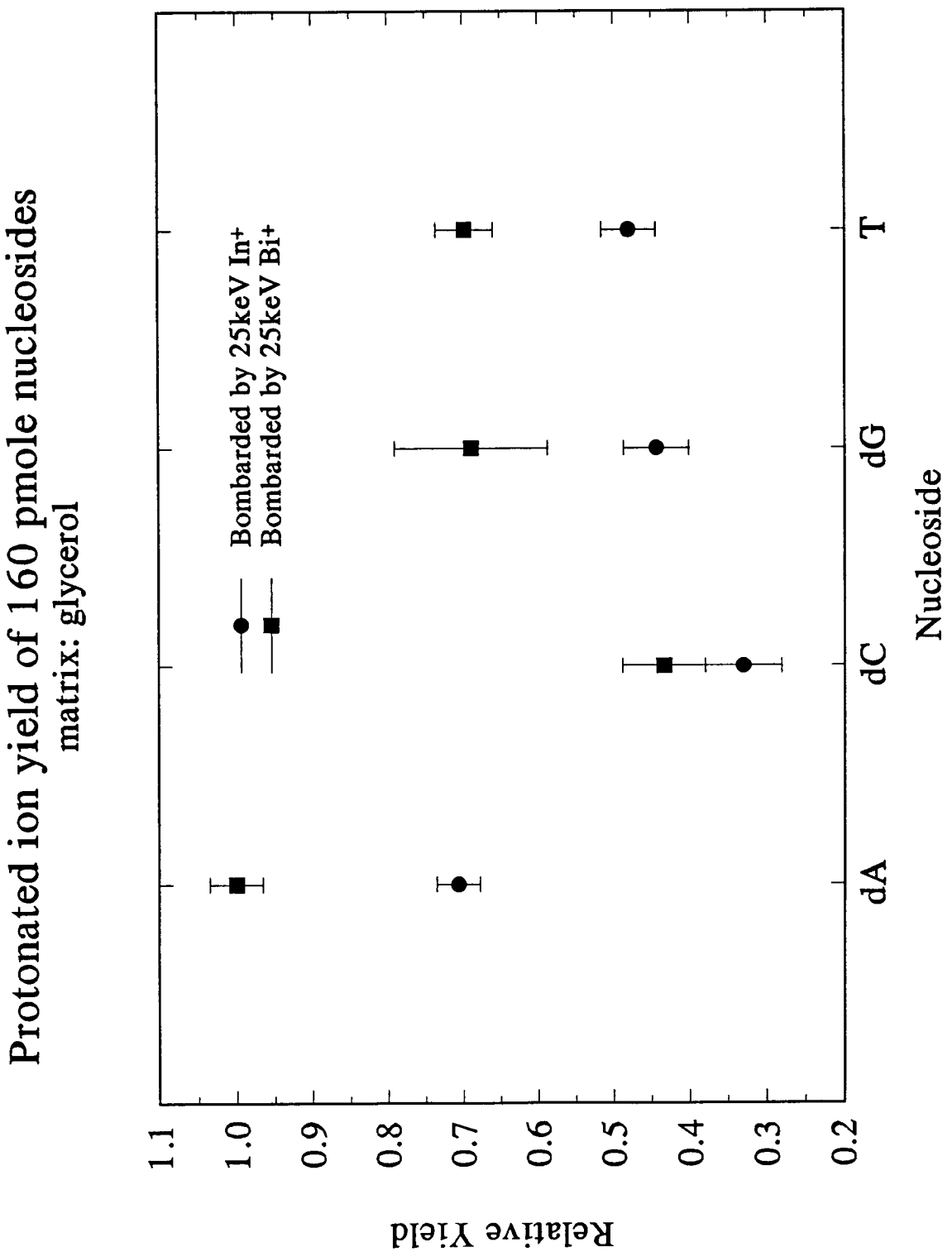

Figure 4-17: Positive ion spectra of nucleotides in glycerol: dAMP (a), and dCMP (b)

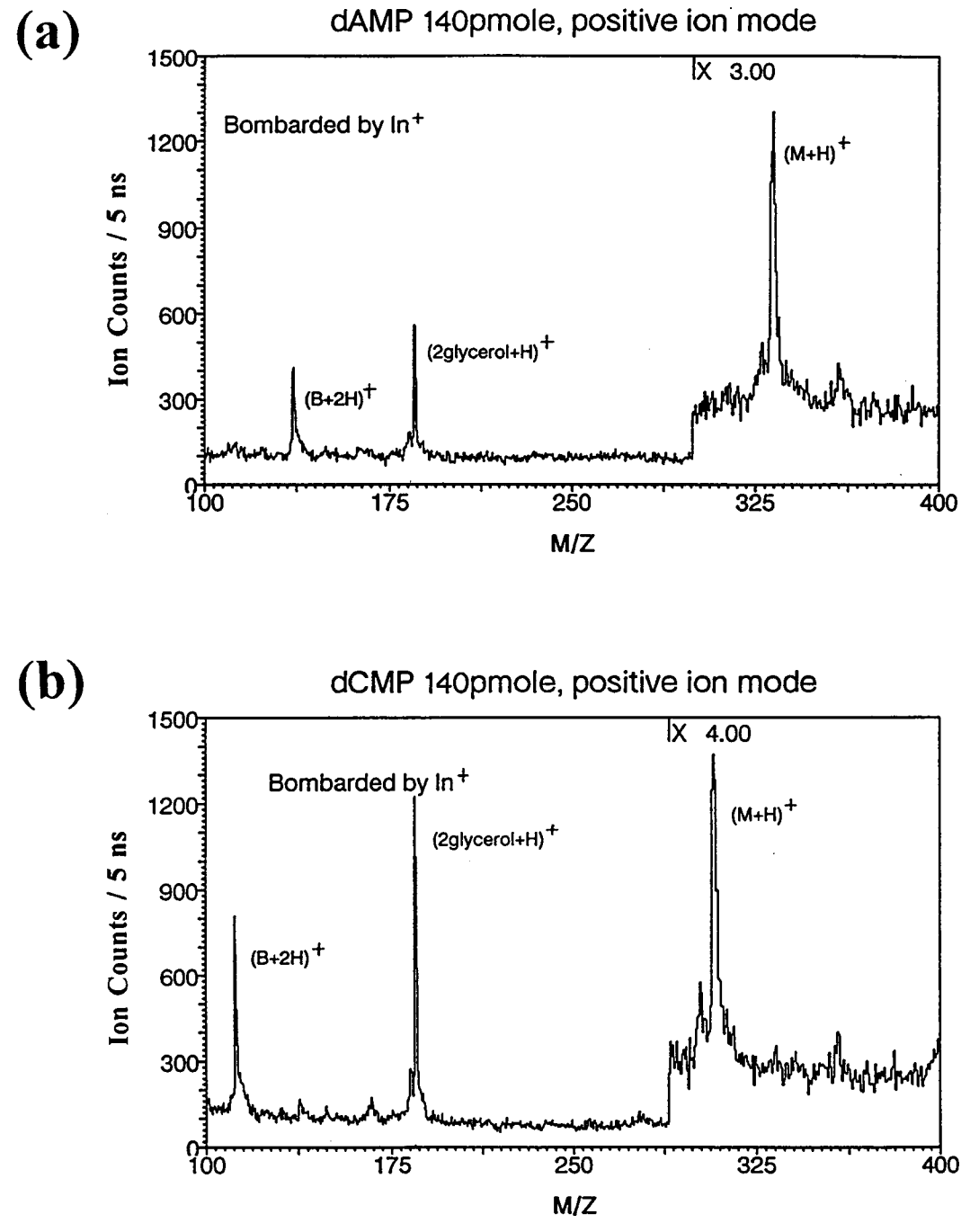

Figure 4-18: Positive ion spectra of nucleotides in glycerol: dGMP (a), and TMP (b)

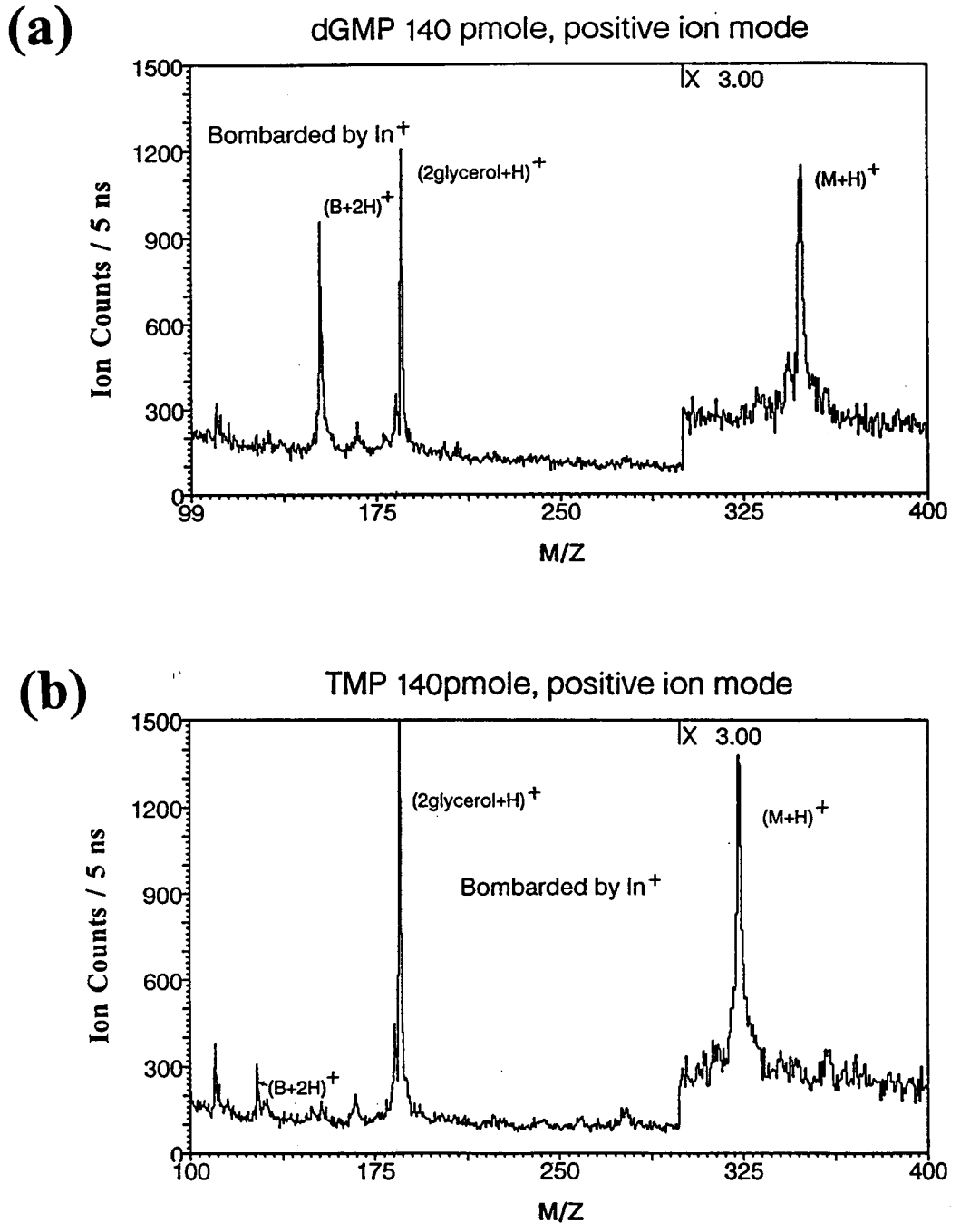

Figure 4-19: Yields of protonated nucleotides bombarded by 25 keV In^+, Bi^+

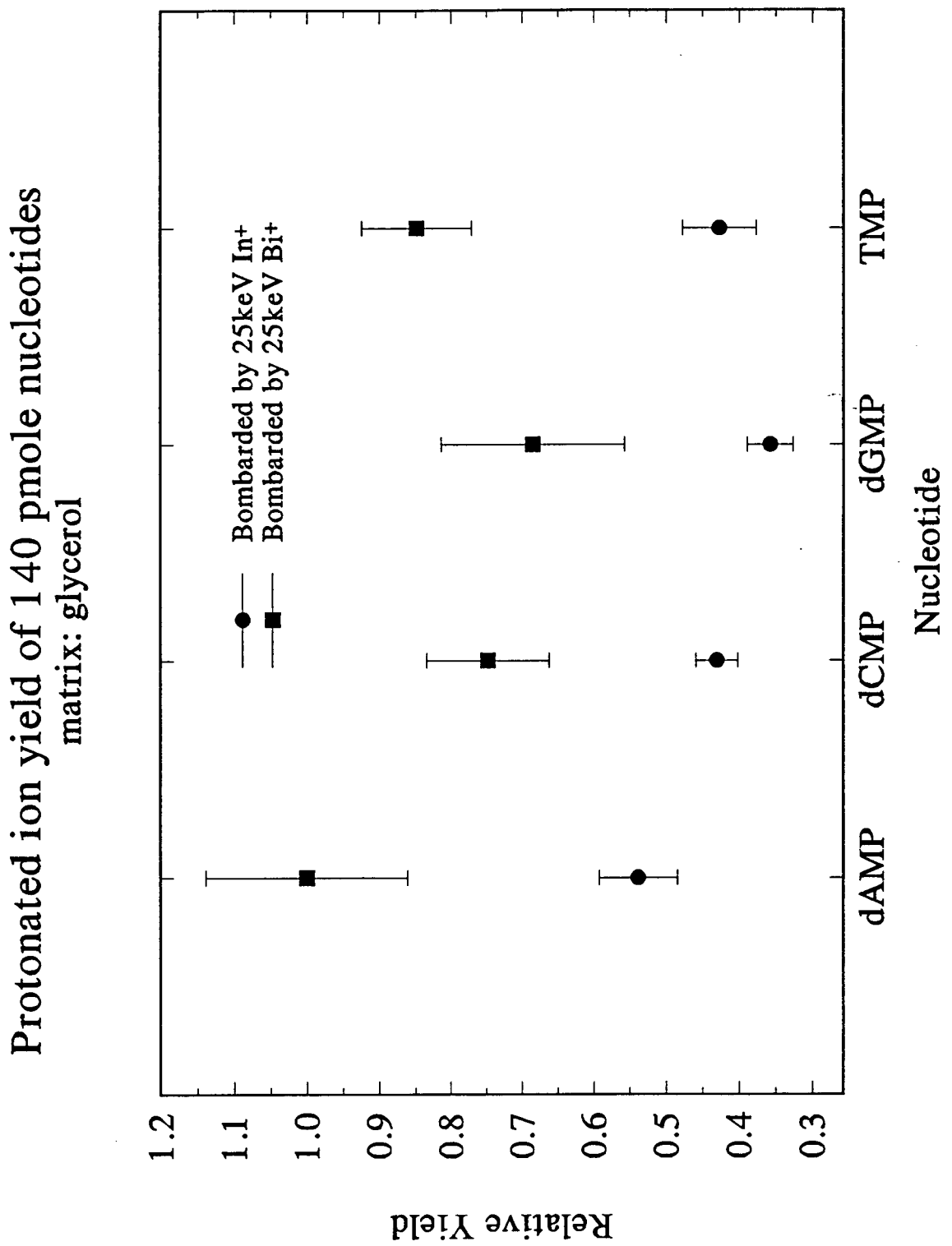

The positive secondary ion spectra of nucleosides and nucleotides behave in time similarly to those of 700 fmol of alanine. Figure 4-20 show the yields of protonated dGMP and protonated diglycerol, and protonated base $(B+2H)^+$ as a function of residence time in vacuum. The yield of protonated dGMP increases gradually with time and reaches a plateau about 15 minutes after the sample is inserted into the mass analyzer.

The yield of protonated deoxyadenosine (dA) as a function of primary ion species is shown in Figure 4-21. Obviously, the yield of protonated dA is greatly enhanced when polyatomic primary ions (Bi_3^{+2}, Bi_2^+, Bi_3^+, Au_2^+, and Au_3^+) are used instead of monoatomic primary ions (Bi^+, Au^+).

In summary, the yields of protonated nucleosides and protonated nucleotides increase with increasing mass of the primary ion; it also varies with the analyte species and the residence time in vacuum. A basic question is where do the secondary ions come from and to what extend do they represent to total sputtering process. In principle, the mechanism for secondary ion emission from the surface of the target is different than that for emission from the bulk of the target. In chapter 2, it was pointed out that a thermal spike model, based on the energy of a primary ion being deposited into a cylindrical matrix volume, predicts the emission of the secondary particles essentially from the surface of the target. For emission of secondary particles from the bulk of the target, we need to consider a spherical spike model in order to obtain the

Figure 4-20: Yields of protonated dGMP as a function of residence time in vacuum

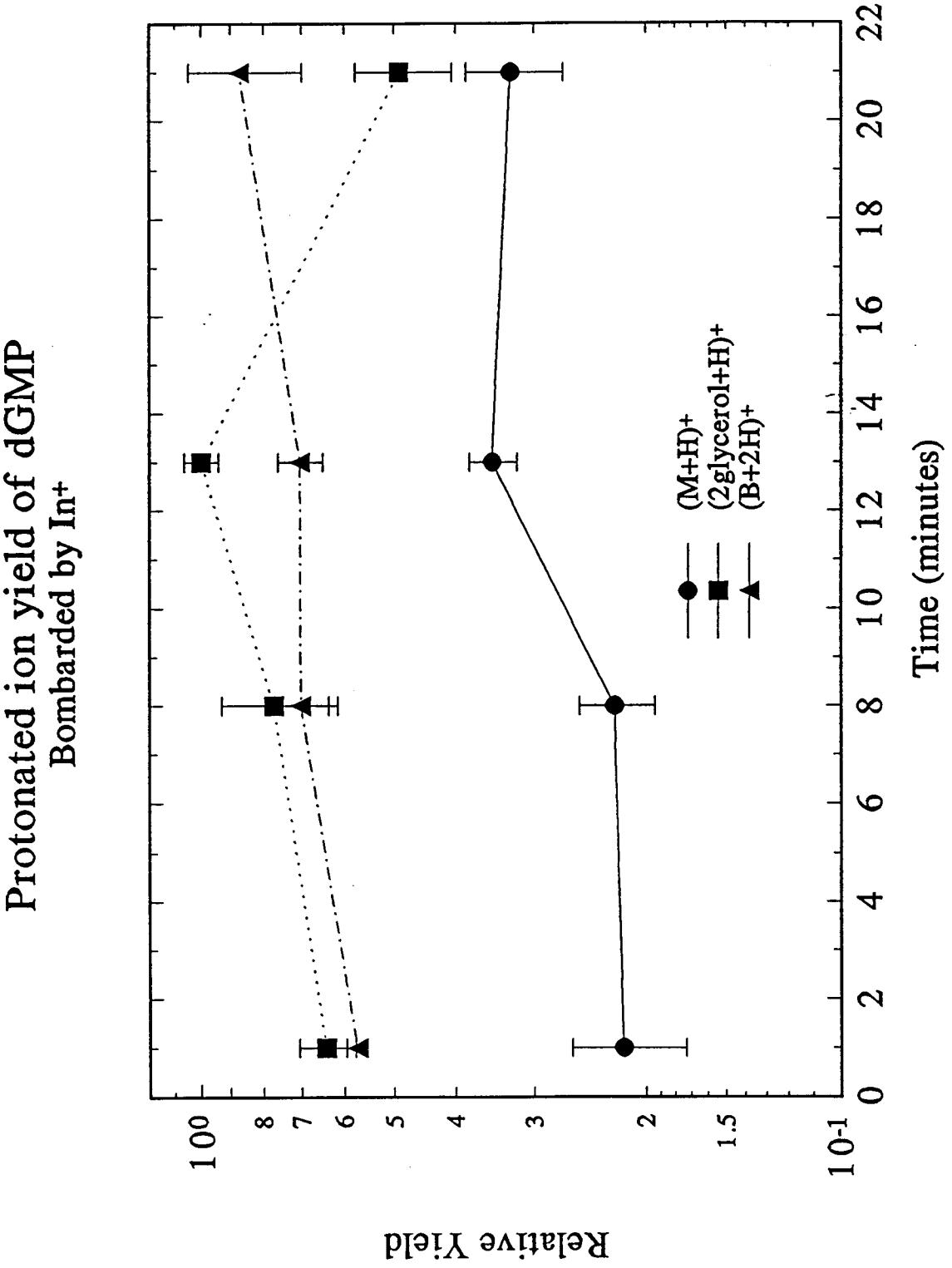

Figure 4-21: Yields of protonated deoxyadenosine bombarded by a different species of primary ions

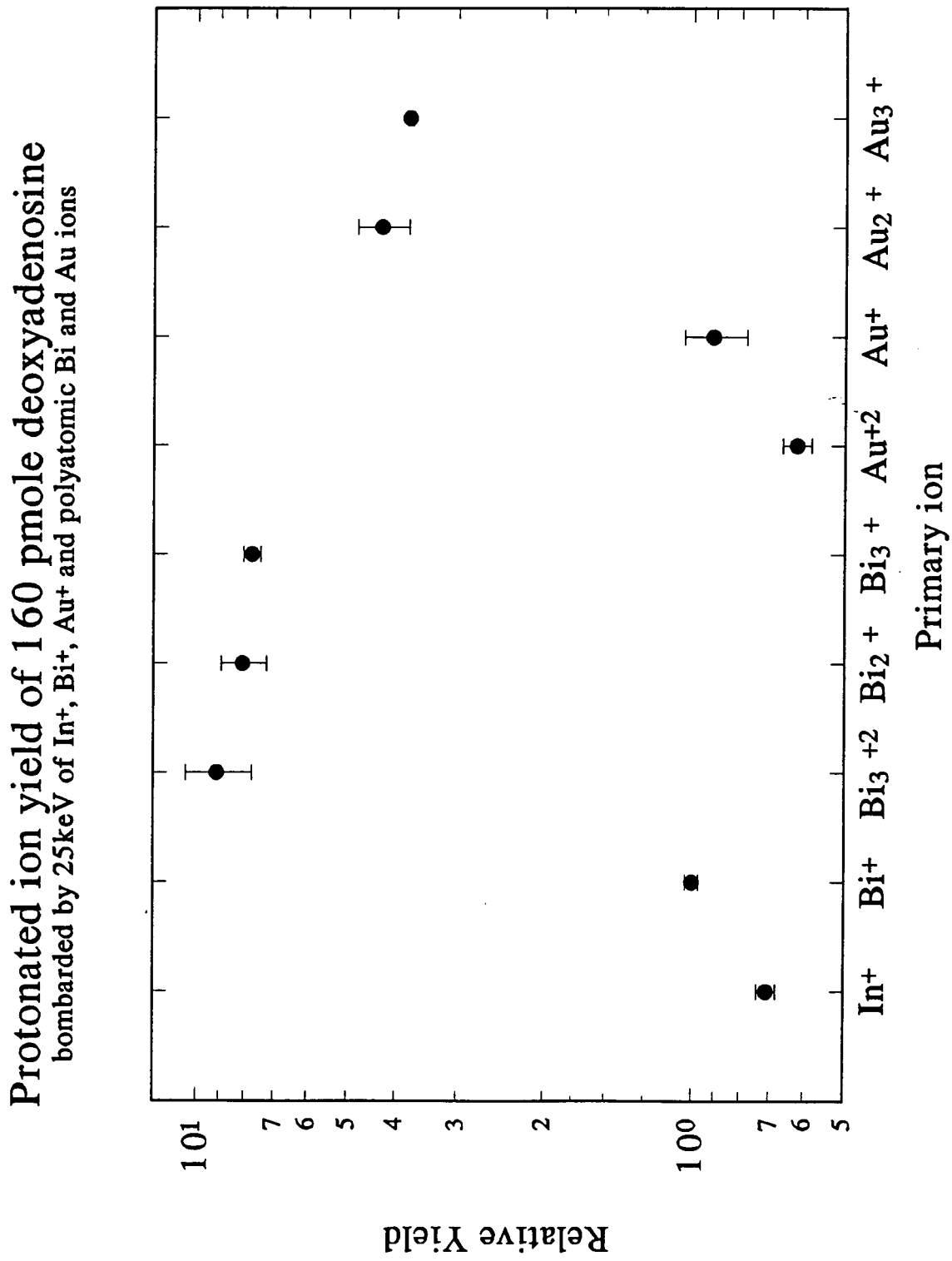

correct expression for the yield as a function of stopping power. The details of these different models will be discussed in the context of our data in next chapter. On the basis of the results that we have shown so far it is not possible to determine whether the secondary ions originate from the surface or from the bulk of the target. In the next section, we present results from a system which allows us some degree of control over this problem.

4-6. Secondary ion yield of nucleotides in the presence of a surfactant.

In chapter 1, we mentioned that Ligon and Dorn[48] reported a sensitivity improvement for deprotonated ATP by adding a surfactant (hexadecylpyridinium acetate, HDPA) to a glycerol matrix. We have systematically measured the secondary ion yields of a two mononucleotides in the presence of HDPA. Hexadecylpyridinium acetate is a surfactant because of the hydrophobic nature of the n-alkyl pyridinium cation in a polar solvent (glycerol, in particular). Figure 4-22(a) shows the negative secondary ion spectrum produced from $1x10^{-2}$ M dGMP in a glycerol matrix bombarded by 0.5nA, 27keV Bi^+. Figure 4-22(b) shows the negative secondary ion spectrum of $1x10^{-3}$ M dGMP with $1x10^{-2}$ M surfactant (HDPA) added to the glycerol. The intensity of the deprotonated dGMP in the presence of HDPA is about 10 time stronger than in the absence of HDPA despite the fact that the concentration of dGMP in Figure 4-22(b) is 1/10 the concentration of dGMP in Figure 4-22(a). It is also interesting to note from these negative ion spectra that with HDPA present the deprotonated glycerol and

Figure 4-22: Negative ion spectra of dGMP (10 mM) in glycerol (a), and of dGMP (1 mM) in HDPA/glycerol matrix (b)

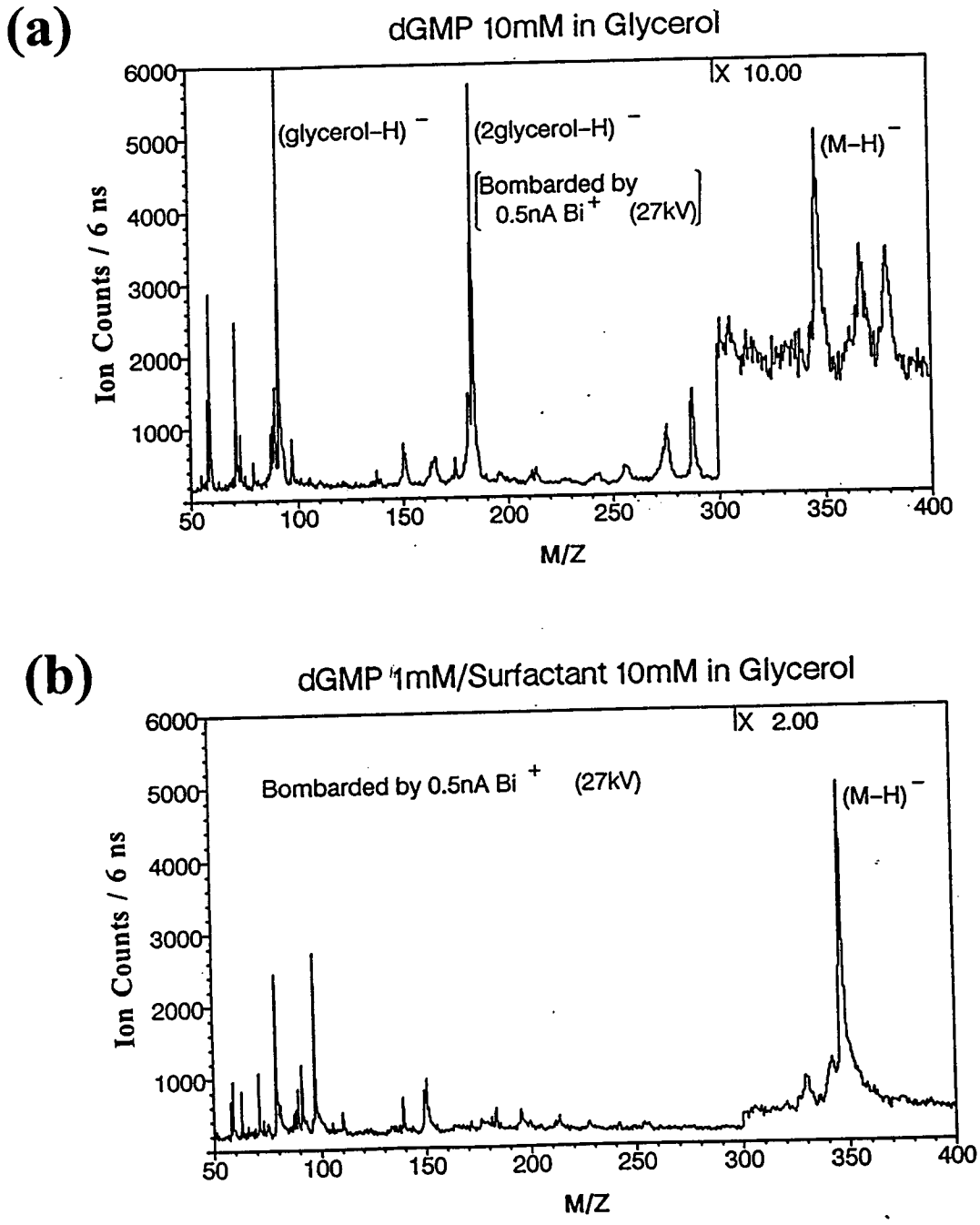

diglycerol ions have been substantially suppressed. The lowest detection limits we have obtained for dAMP and dGMP from an HDPA/glycerol matrix are 4 fmol (0.4 nL of 10^{-5} M dAMP) and 5 fmol (0.4 nL of 1.25×10^{-5} M dGMP) respectively. These spectra are shown in Figures 4-23(a) and (b).

The yields of deprotonated dAMP and deprotonated dGMP in an HDPA/glycerol matrix are dependent on the concentration of HDPA, on the identity and the concentration of analyte as well as on the energy of primary ion. Figure 4-24 shows the relative yields of deprotonated dGMP generated by three different primary ions (Bi^+, Bi_3^{+2}, and Au^+) with the same energy (25keV) as a function of the concentration of HDPA. In all three cases, the deprotonated dGMP shows a clear maximum at HDPA concentration about 10 mM. Also evident, as in the case of the positive secondary ion spectra, is that the yield of deprotonated dGMP is much greater under bombardment with a polyatomic ion, (Bi_3^{+2}) than under bombardment with a monoatomic ion (Bi^+, Au^+). As a function of residence time in vacuum, the secondary ion signals of dAMP and dGMP in presence of HDPA behave similarly to those of 7 pmol of alanine. Figure 4-25 shows the yield of deprotonated dGMP at three concentrations as a function of the concentration of HDPA. The maximum of the curves clearly varies with the concentration of the analyte (dGMP). Also the relative enhancement of yield at the lower concentration of dGMP (0.1 mM) in presence of HDPA is seen to be slightly larger than that at the two higher concentrations (1 mM and 10 mM).

Figure 4-23: Negative ion spectra of 4 fmol dAMP (a), and of 5 fmol dGMP (b) in HDPA/glycerol matrix

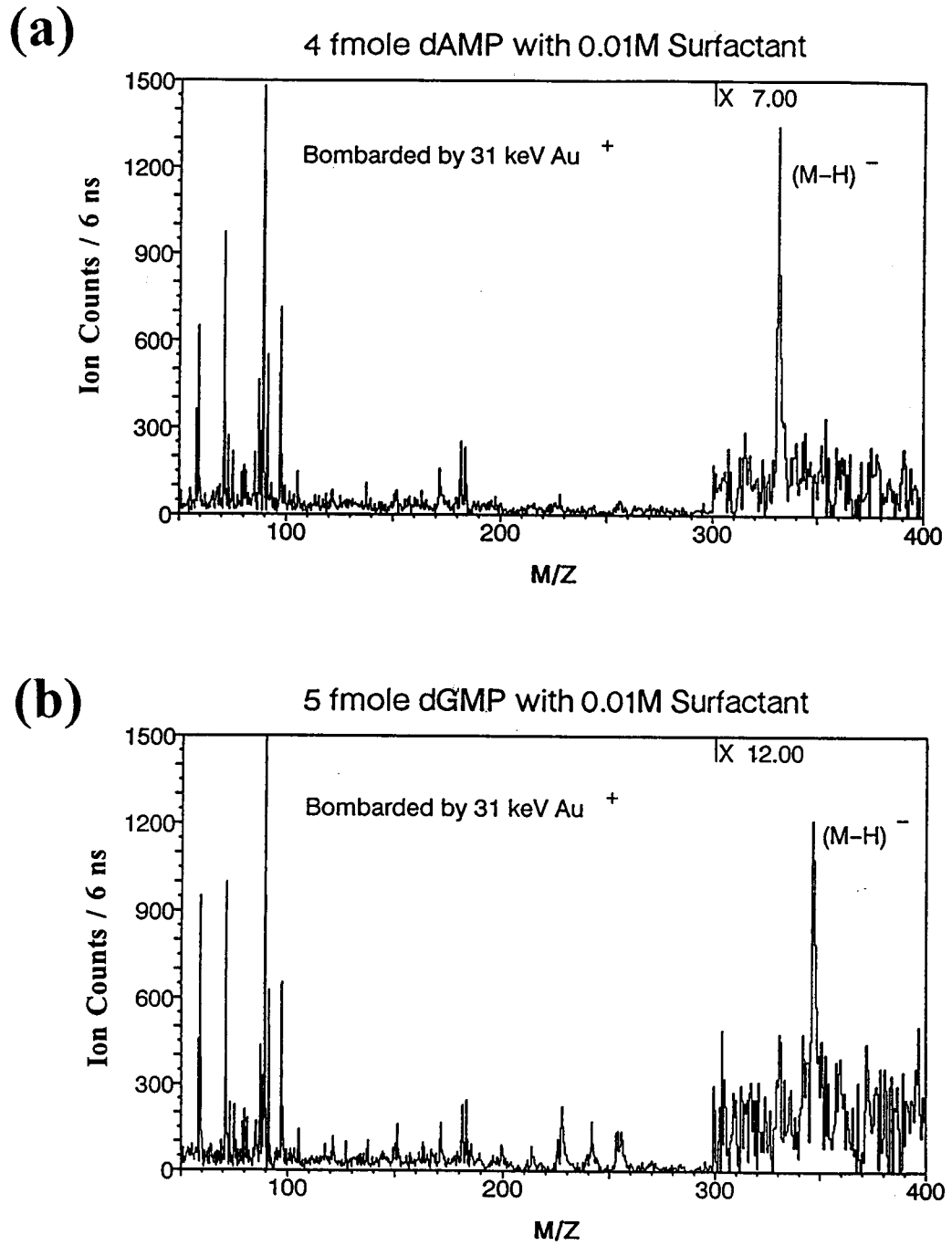

Figure 4-24: Yields of deprotonated dGMP bombarded by Au^+, Bi^+, and Bi_3^{+2} as a function of the concentration of surfactant (HDPA)

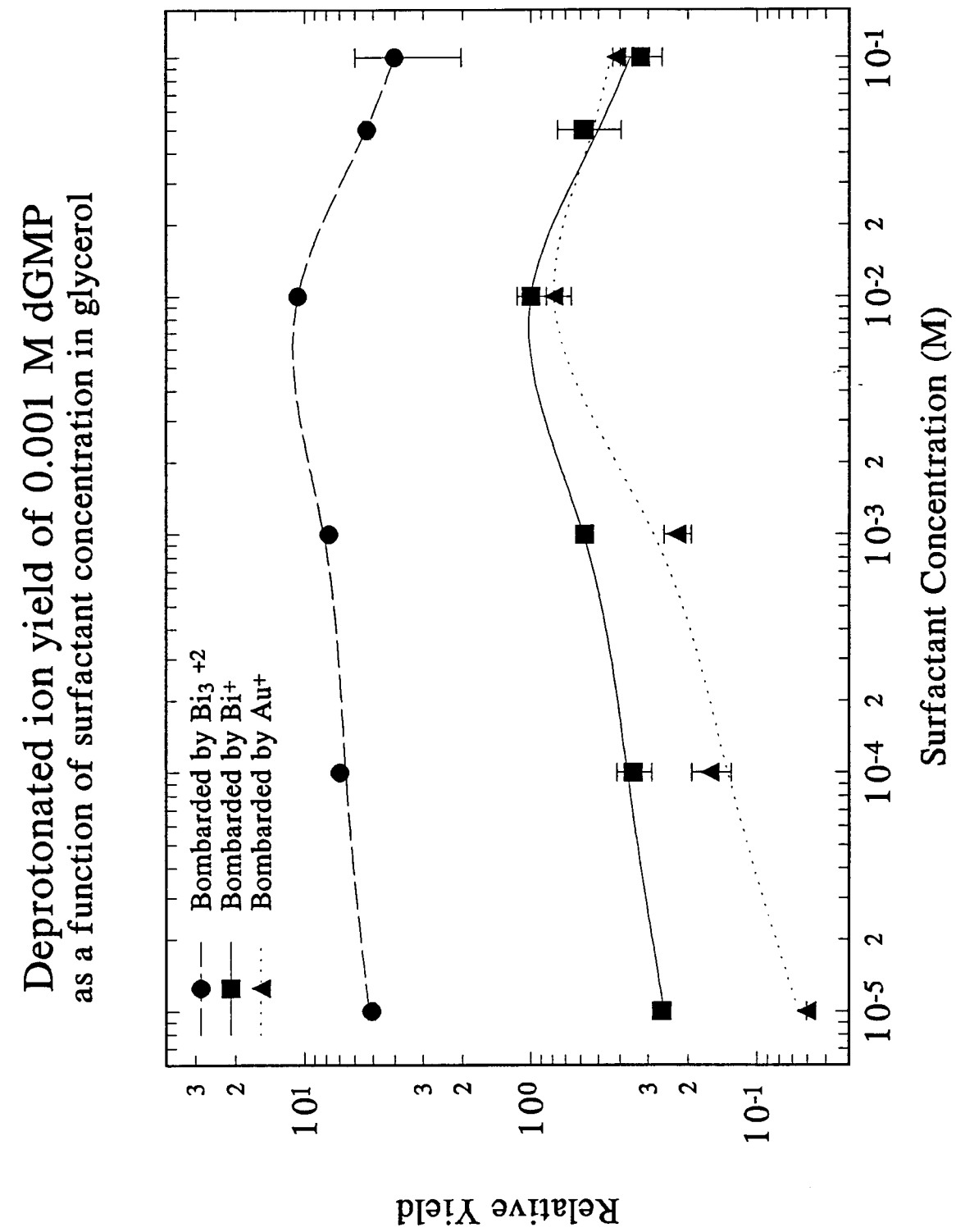

Figure 4-25: Yields of deprotonated dGMP bombarded by Au^+ ion, as a function of the concentration of surfactant (HDPA) and of dGMP

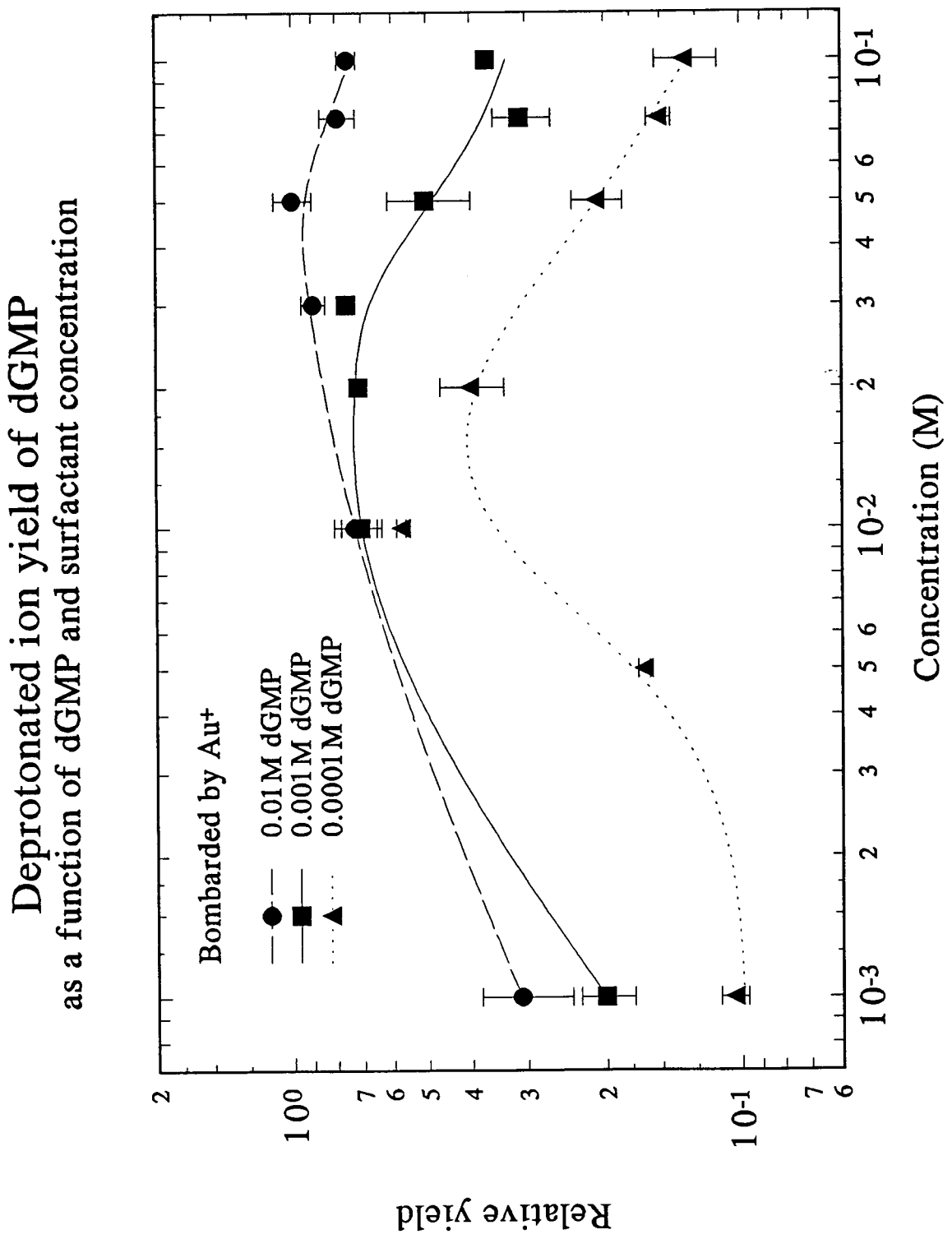

Systematic measurements of the yields of deprotonated dAMP and deprotonated dGMP as well as $(HDPA-59)^+$ have been made as functions of the primary ions species (monoatomic or polyatomic ions) and the energy of the primary ions. Figures 4-26 (a) and (b) show the relative intensity of deprotonated dAMP and deprotonated dGMP, respectively, as a function of the primary ion beam accelerating voltage in the range 11kV to 27kV for the five monoatomic primary ions (Bi^+, Au^{+2}, Au^+, In^+, and Ga^+). Intensity are normalized with respect to the intensity of deprotonated dAMP bombarded by 27kV Au^+.

The variations in relative intensity of the negative ions of dAMP and dGMP sputtered from a matrix of 10 mM HDPA in glycerol bombarded by the polyatomic primary ions (Bi_3^{+2}, Bi_2^+, Au_2^+, and Au_3^+) are shown in Figure 4-27 as a function of the accelerating voltage of the primary ions. Again, we clearly observe that the relative intensity of the deprotonated nucleotides generated by bombardment with polyatomic ions (Bi_3^{+2}, Bi_2^+, Au_2^+, Au_3^+) are much greater than those generated by bombardment with monoatomic ions (Bi^+, Au^+).

The positive secondary ion spectra of 10 mM dAMP and 10 mM dGMP in a matrix of 10 mM HDPA in glycerol are shown in Figure 4-28 (a), and (b), respectively. Hexadecylpyridinium cation $(HDPA-59)^+$ is dominant in these spectra; moreover, the intensity of $(HDPA-59)^+$ in Figure 4-28(a) is almost as same as that in Figure 4-28(b). Positive ion spectra of 10 mM HDPA in glycerol without the mononucleotides dAMP

Figure 4-26: Intensity of deprotonated dAMP (a) and deprotonated dGMP (b) bombarded by monoatomic ions (Au^+, Au^{+2}, Bi^+, In^+, Ga^+)

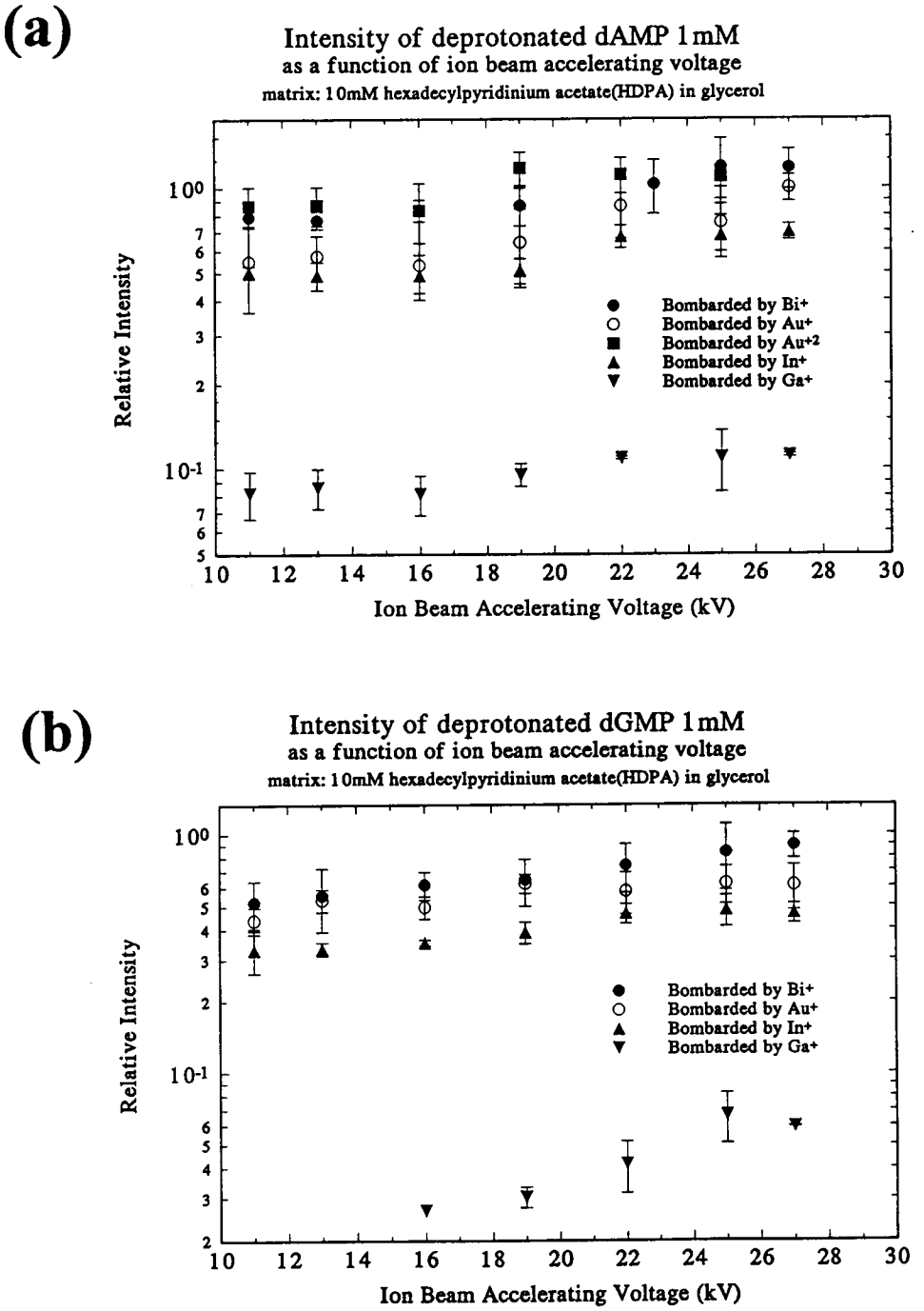

Figure 4-27: Intensity of deprotonated dAMP (a) and deprotonated dGMP (b) bombarded by monoatomic and polyatomic ions (Au^+, Au^{+2}, Bi^+, In^+, Ga^+, Bi_3^{+2}, Bi_2^+, Au_2^+, Au_3^+)

(a)

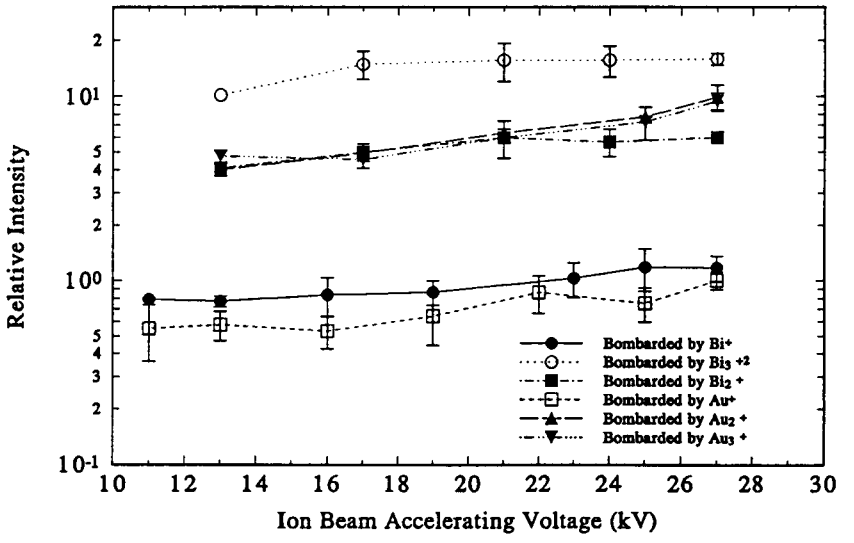

(b)

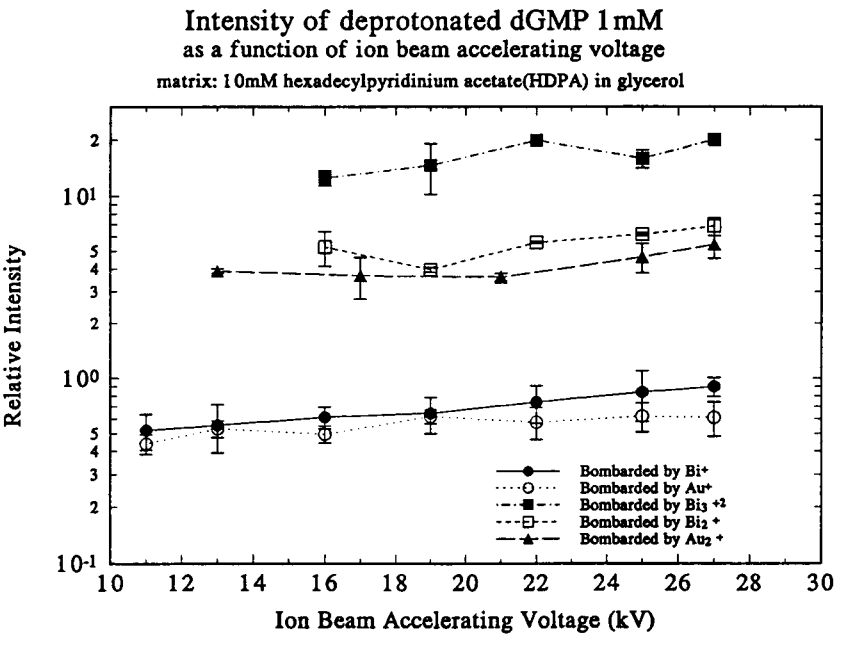

Figure 4-28: Positive ion spectra generated by bombardment with 27 keV Bi+ from dAMP in 10 mM HDPA/glycerol matrix (a), and form dGMP in 10 mM HDPA/glycerol matrix (b)

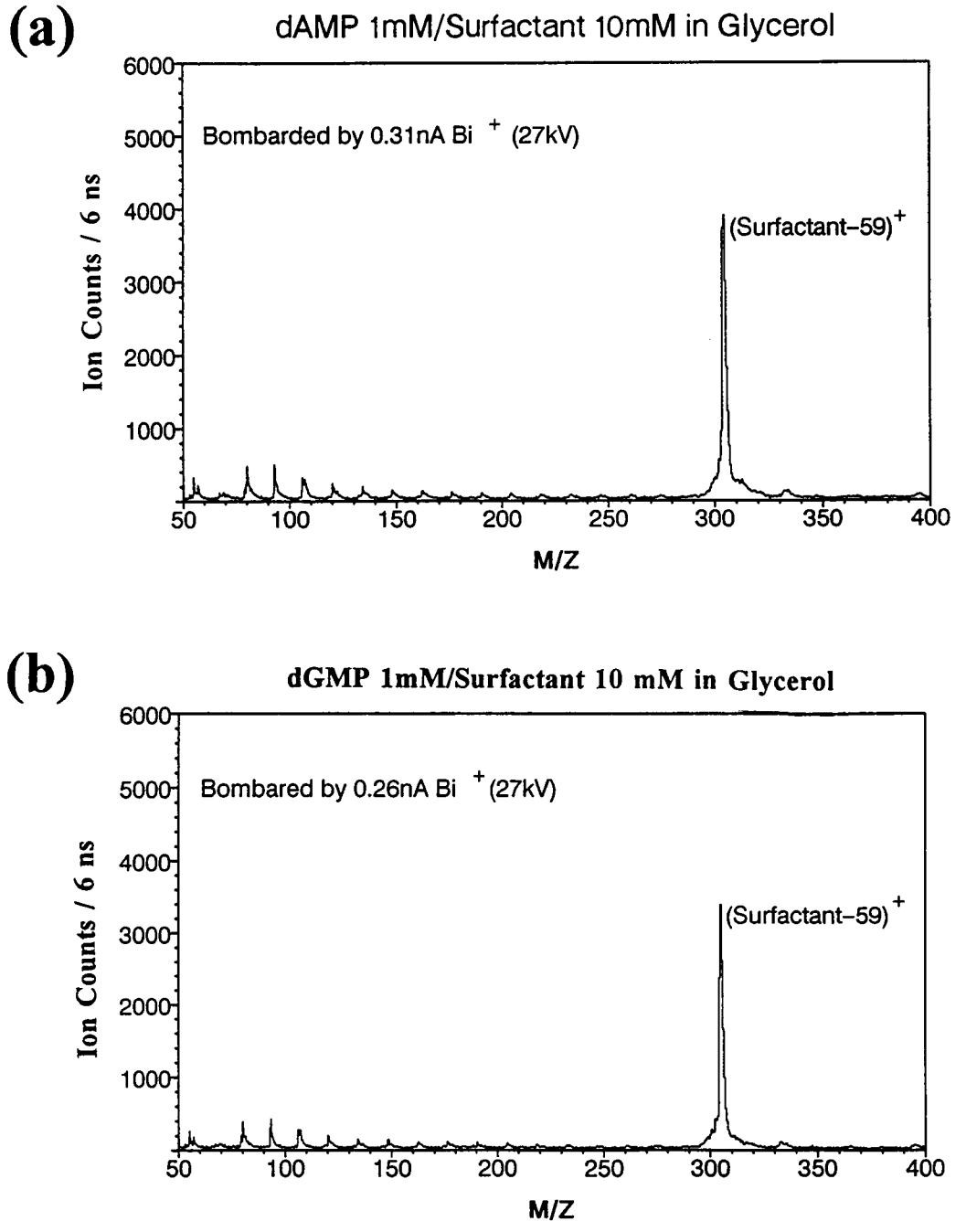

and dGMP are essentially the same, i.e. show the same intensity of $(HDPA-59)^+$ and the same background, as those with the mononucleotides under the same bombardment conditions. The intensity of $(HDPA-59)^+$ slowly increases with concentration of HDPA in the glycerol. The relationship between the relative intensity of $(HDPA-59)^+$ and the relative intensity of $(2glycerol+H)^+$ as a function of the concentration of HDPA in glycerol is shown in Figure 4-29. The signal from protonated glycerol $(glycerol+H)^+$ and protonated diglycerol $(2glycerol+H)^+$ are almost completely suppressed when the concentration of HDPA in glycerol reaches 1 mM. The intensity of $(HDPA-59)^+$ from a matrix of 10 mM HDPA in glycerol as a function of the primary ion beam accelerating voltage for the three primary ion species Ga^+, In^+, and Bi^+ has also been measured and is shown in Figure 4-30. Comparison of Figure 4-30 to Figure 4-27(a) clearly shows that the intensity of $(HDPA-59)^+$ is 10 fold stronger than that of deprotonated dAMP. Intensity of $(HDPA-59)^+$ is normalized to the intensity of deprotonated dAMP generated from the same matrix by bombardment with 27kV Au^+.

4-7. Disappearance cross section

In the previous section, we have shown that the yields of deprotonated dAMP and dGMP are greatly increased when HDPA is present in the glycerol matrix. The liquid matrix exhibits another interesting phenomenon, namely that the analyte's signal can last for a long time without significantly decreasing even when the matrix is bombarded with a high current of primary ion beam. This is much different than in case

Figure 4-29: Yields of HDPA cation and protonated diglycerol as a function of the concentration of HDPA

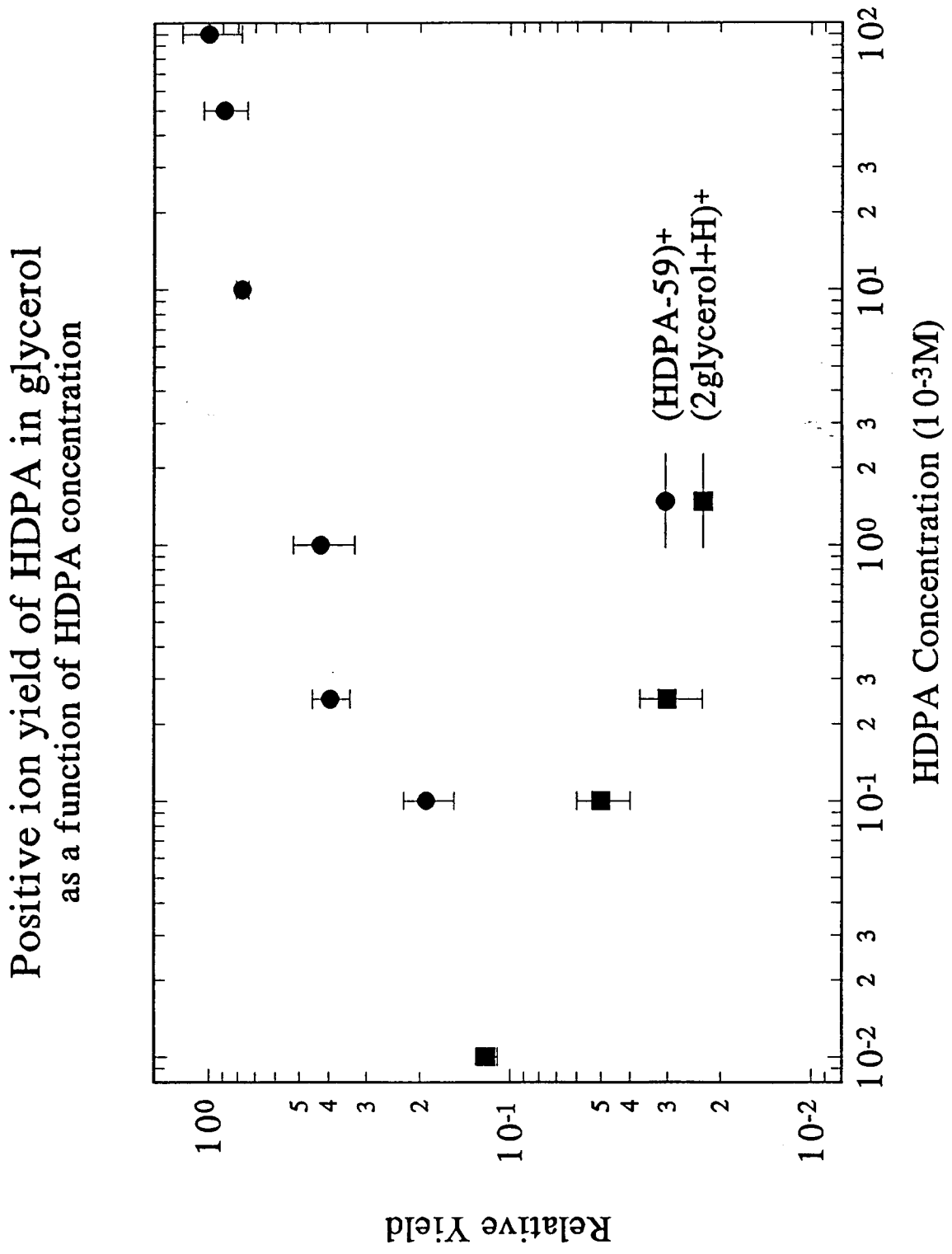

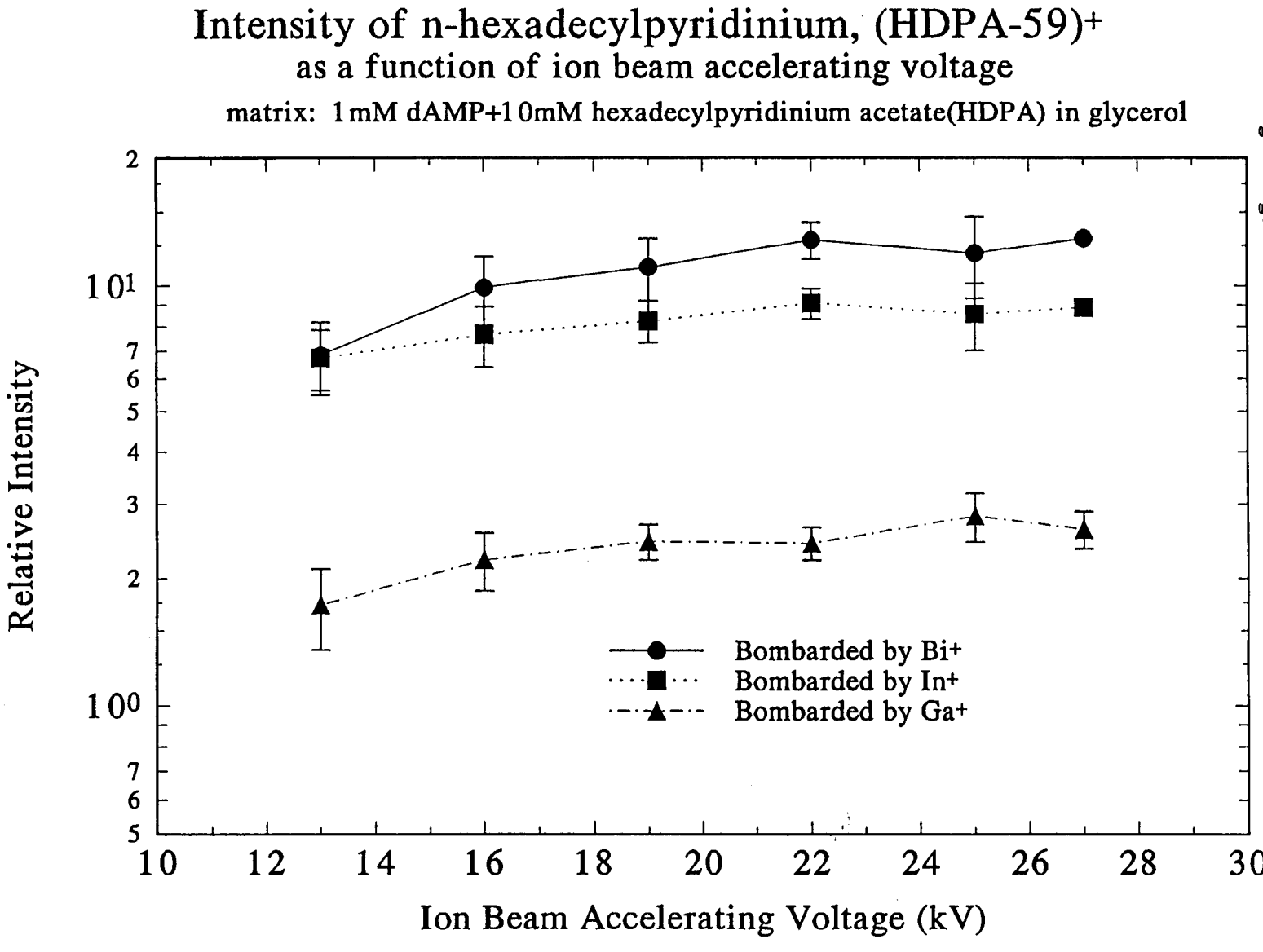

Figure 4-30: Intensity of hexadecylpyridinium cation as a function of ion beam accelerating voltage

of an organic analyte adsorbed to the surface of a solid where the analyte's signal quickly decreases due to the bombardment from a high current of primary ion beam. In section 3-4, we showed that the disappearance cross section of analyte during sputtering can be calculated from equation 3-4. We have measured the disappearance cross section of deprotonated dGMP from a matrix of 10 mM HDPA in glycerol and the disappearance cross section of $(HDPA-59)^+$ from a series of matrices with different concentrations of HDPA in glycerol. Figure 4-31(a) shows the positive secondary ion spectrum of 0.1 mM HDPA in glycerol generated by bombardment with 25 kV In^+ (those spectra without any special indication were recorded with a primary ion dose of less than $2x10^{13}$ ions/cm^2). Figure 4-31(b) shows the positive ion spectrum of the same analyte as in Figure 4-31(a) with a primary ion dose of $2.5x10^{14}$ ions/cm^2. The spectra of 1 mM HDPA in glycerol and 10 mM HDPA in glycerol under bombardment with the same primary ion fluxes are shown in Figure 4-32 and Figure 4-33, respectively. Intensities of the protonated glycerol species from 0.1 mM HDPA in glycerol are more than twice as large under bombardment with the higher primary ion dose (Figure 4-31(b)) than with the lower primary ion dose (Figure 4-31(a)). By contrast, the intensity of $(HDPA-59)^+$ (MW=304) from the same matrix decreases when the primary ion dose is increased. These measurements suggest that the surface of the analyte is mostly replenished by glycerol. However, this is not the case when the concentration of HDPA in glycerol is over 1mM; there are no indications of the surface replenishment by glycerol in Figure 4-32 and Figure 4-33. A striking difference between Figure 4-32 and Figure 4-33 is that the decrease in intensity of $(HDPA-59)^+$ from 10 mM HDPA in

Figure 4-31: Positive ion spectra of 0.1 mM HDPA/glycerol bombarded by 25 keV In^+ with an ion dose of < 10^{13} ions/cm^2 (a), and with an ion dose of 2.5x10^{14} ions/cm^2 (b)

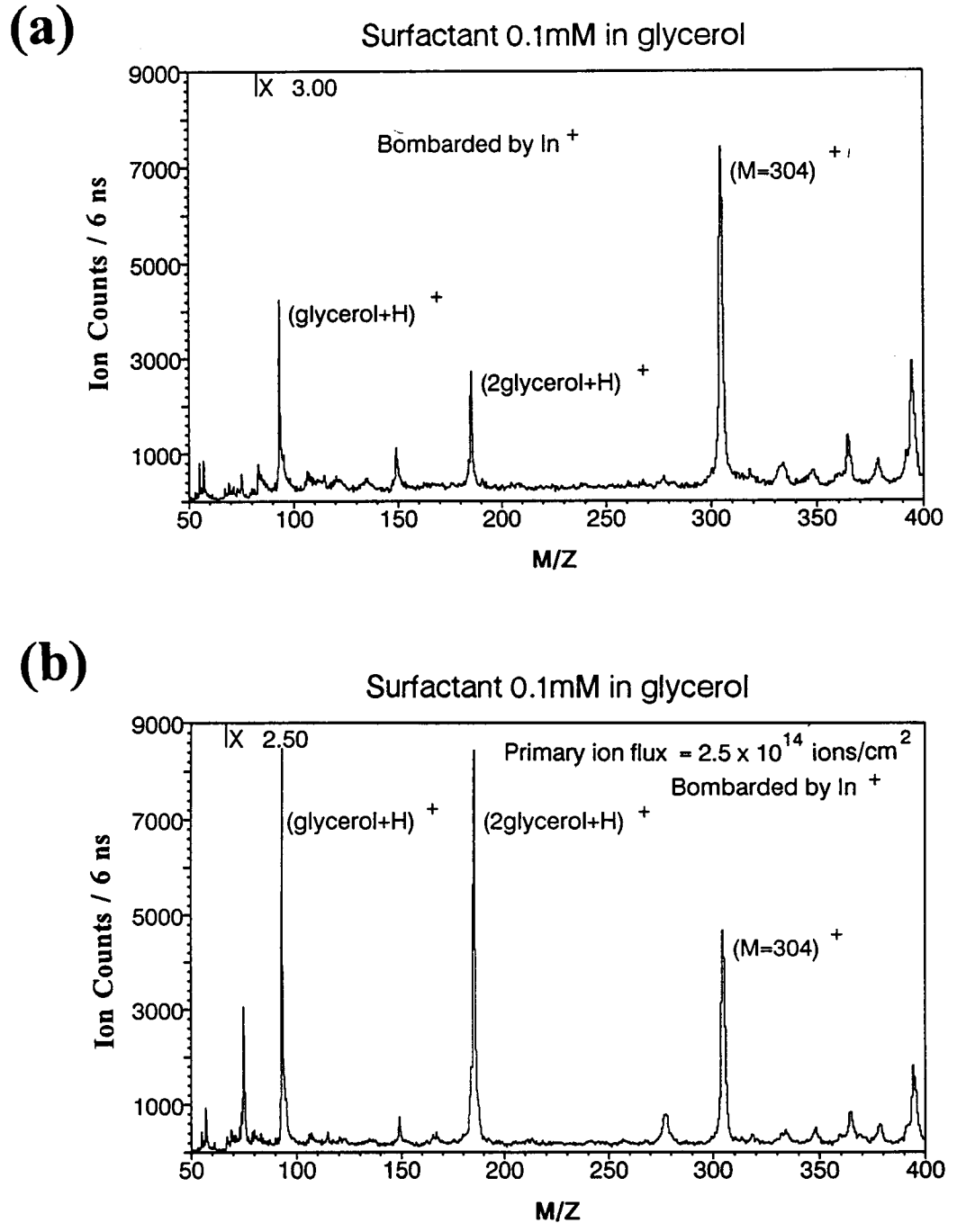

Figure 4-32: Positive ion spectra of 1 mM HDPA/glycerol bombarded by 25 keV In^+ with an ion dose of < 10^{13} ions/cm^2 (a), and with an ion dose of 2.5x10^{14} ions/cm^2 (b)

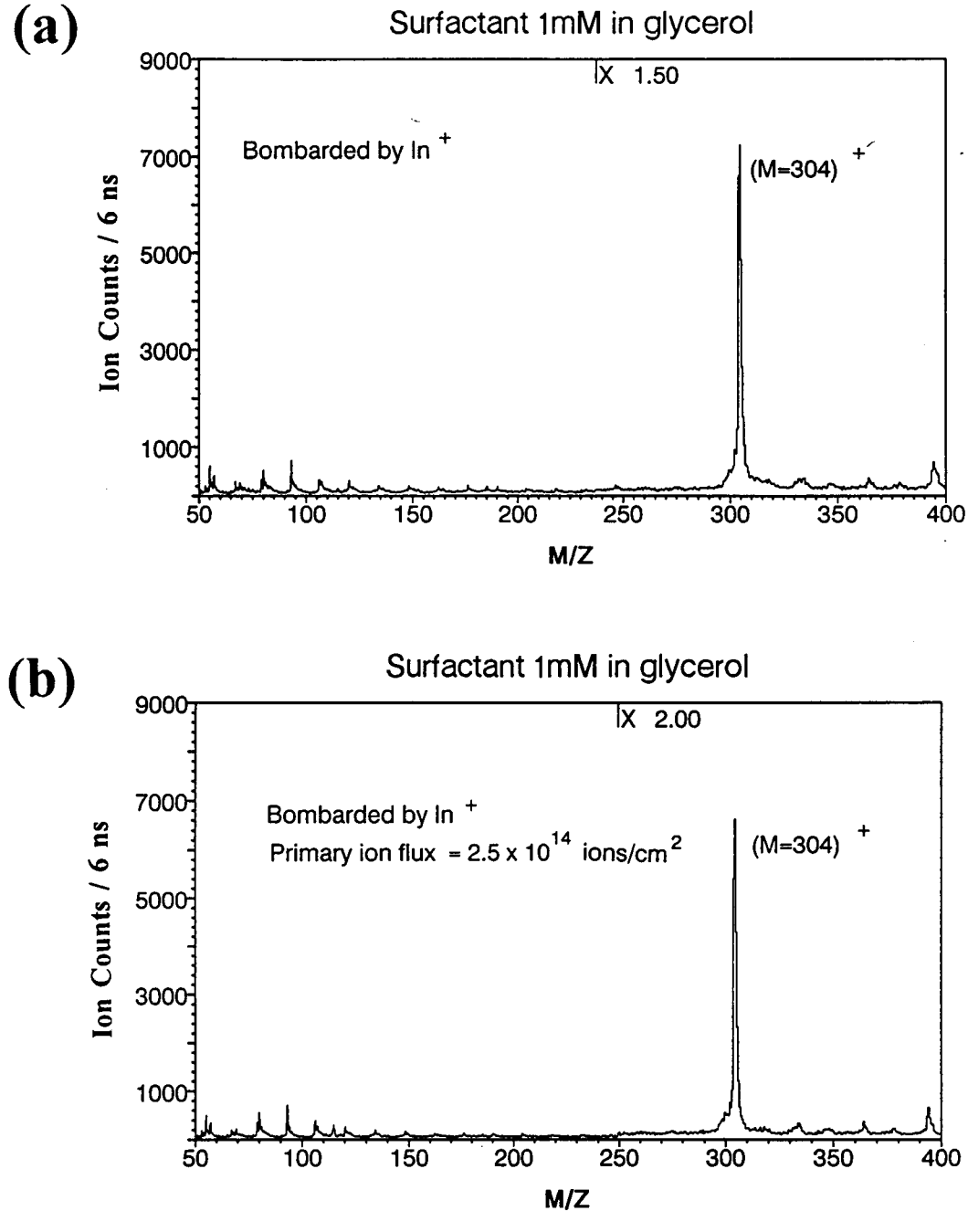

Figure 4-33: Positive ion spectra of 1 mM HDPA/glycerol bombarded by 25 keV In^+ with an ion dose of < 10^{13} ions/cm^2 (a), and with an ion dose of $2.5x10^{14}$ ions/cm^2 (b)

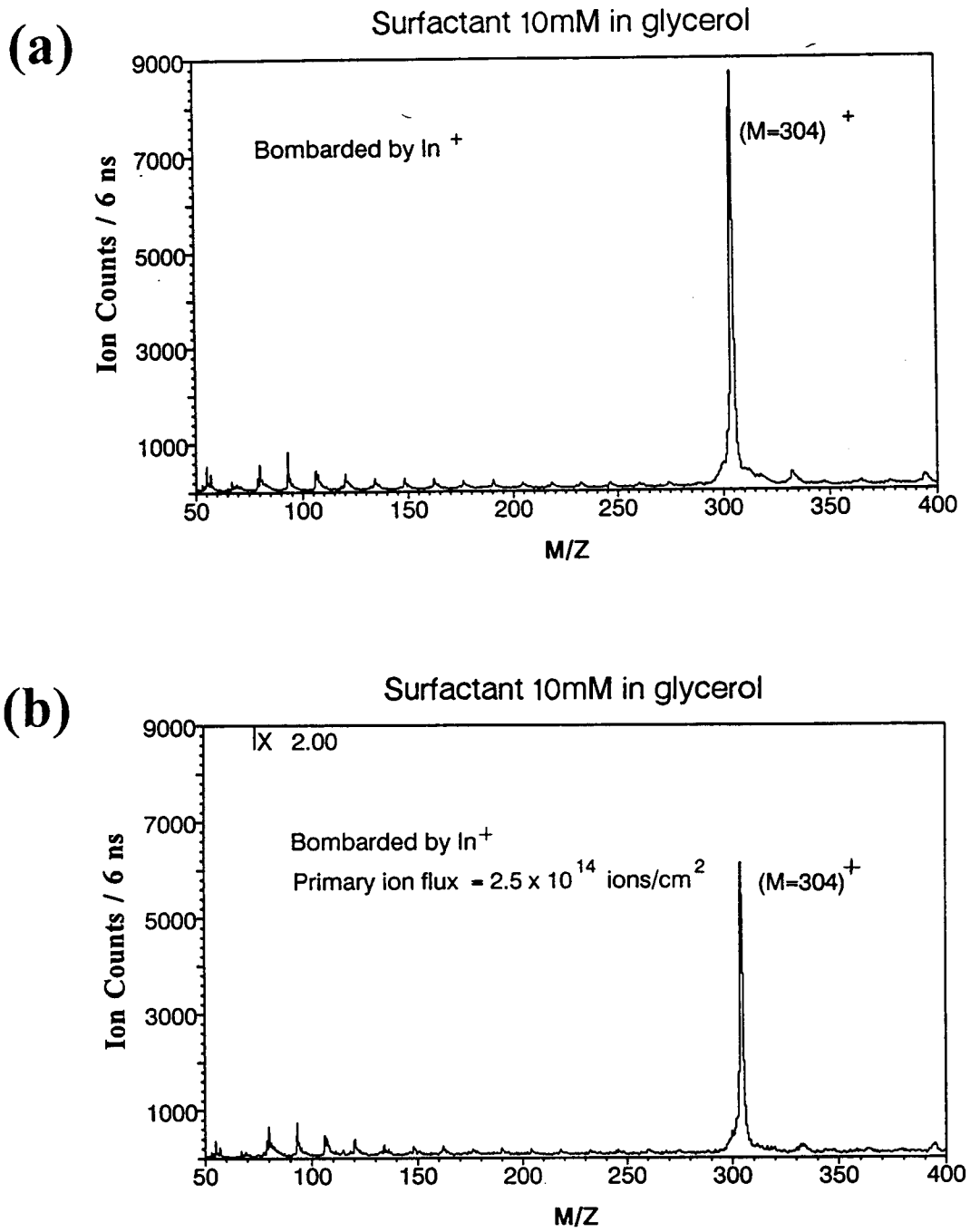

glycerol (Figure 4-33(b)) under bombardment with a high primary ion dose is much more pronounced than that from 1 mM HDPA is glycerol (Figure 4-32(b)). Figures 4-34 and 4-35 show the disappearance cross section plots for $(HDPA-59)^+$ and deprotonated dGMP, respectively. The disappearance cross section for both analytes is about $2x10^{-15}$ cm^2/ion. This is more than an order of magnitude lower than the results from an analyte adsorbed on the solid substrate under bombardment with keV primary ions ($\sigma \approx 5x10^{-14}$ cm^2/ion)[76]. The most plausible explanation for the lower value of the disappearance cross section in the case of a liquid matrix is that a liquid is capable of the surface replenishment on the same time frame as the arrival of the primary ions whereas a solid is not. However, an analytical explanation for these results is not yet available.

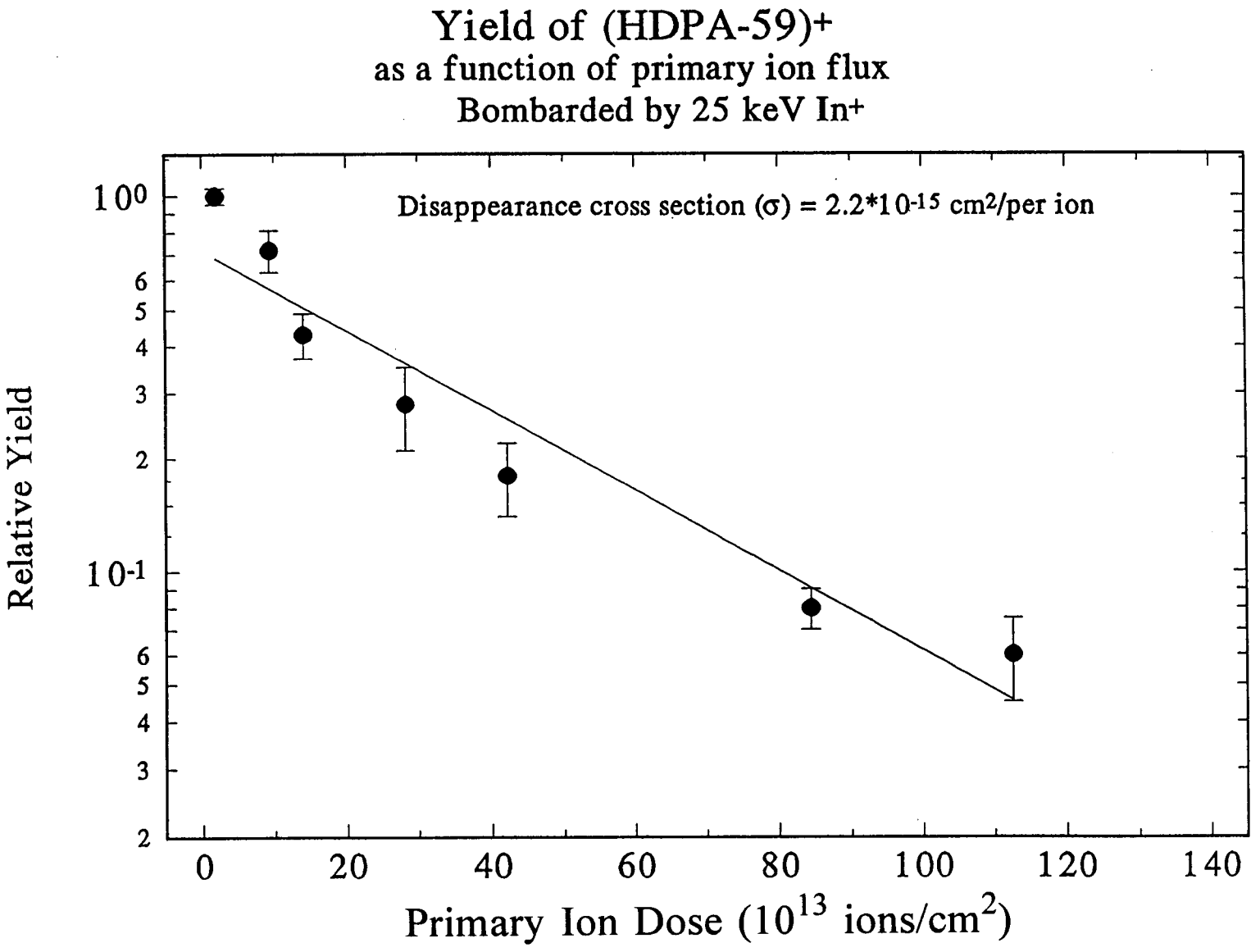

Figure 4-34: Yields of $(HDPA\text{-}59)^+$ as a function of primary ion dose

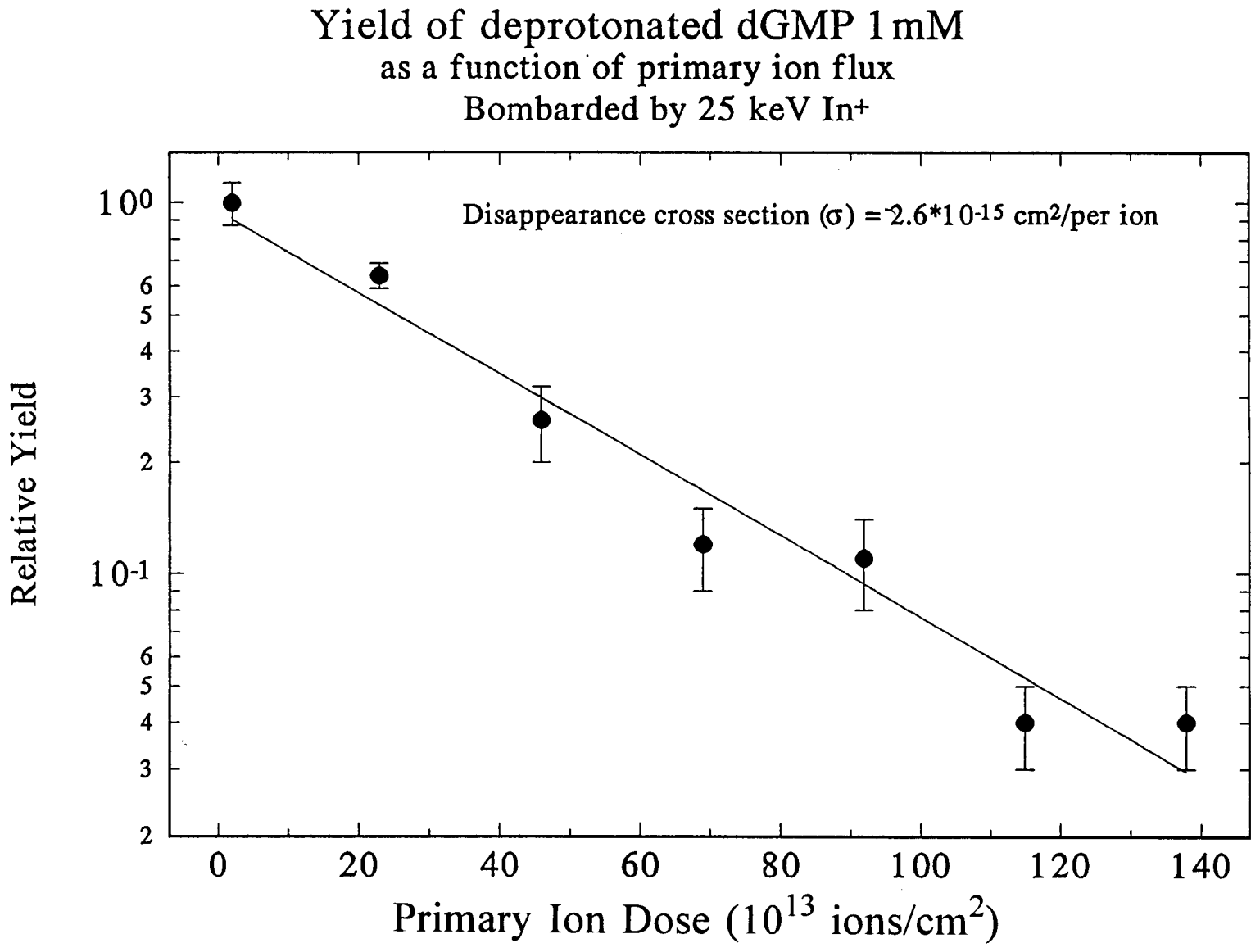

Figure 4-35: Yields of deprotonated dGMP as a function of primary ion dose

Chapter 5

Discussion

5-1. Calculations of nuclear stopping cross section

In chapter 2, we have shown that the total stopping cross section can be calculated from equation 2-16. Because the electronic stopping cross section contributes less than 20% to the total stopping cross section in our experiments, most of error of in calculating the total stopping cross section is generated from the computations of the nuclear stopping cross section. Accurate calculations of the nuclear stopping cross section depend on the forms of the ion-atom interaction potential (screening Coulombic potential) and of the screening Coulombic length, a. In general, two different screening lengths have been widely adopted: Firsov's and Bohr's as modified by Lindhard et al.[50] These expressions are given by

$$a_F = \frac{0.8853 a_0}{(Z_1^{\frac{1}{2}} + Z_2^{\frac{1}{2}})^{\frac{2}{3}}} \quad (Firsov), \tag{5-1}$$

$$a_B = \frac{0.8853 a_0}{(Z_1^{\frac{2}{3}} + Z_2^{\frac{2}{3}})^{\frac{1}{2}}} \quad (Bohr). \tag{5-2}$$

where a_0 =0.53 Å. Figure 5-1 shows the total stopping cross sections calculated for glycerol from Firsov's and Bohr's screening lengths; a Thomas-Fermi interaction potential was used to calculate these nuclear stopping cross sections. The stopping cross sections from Bohr's screening length are systematically larger than those from Firsov's screening length for Bi^+, Au^+, In^+, and Ga^+ primary ions. The numerical variation between stopping powers generated with Bohr's screening length and those generated with Firsov's screening length is not great; the maximum difference being less than 10%.

Figure 5-2 shows total stopping cross sections for glycerol that have been calculated from a Wilson[51] potential and from a Thomas-Fermi potential. Wilson et al.[51] developed a free electron method to calculate the nuclear stopping cross section, using Kr-C as a representative case. The numerical expression for the reduced nuclear stopping cross section $s_n(\varepsilon)$ using a Wilson potential is the same as that given by equation 2-8 except that A is equal to 0.10718 and B is equal to 0.37544. Obviously, the two potentials yield significantly different results in different parts of energy range. At high ion energies (> 200keV), the total stopping cross sections calculated from the two potentials for Bi^+, In^+, and Ga^+ primary ions in glycerol are nearly the same.

Figure 5-1: Stopping cross section of glycerol for Firsov and Bohr screening length

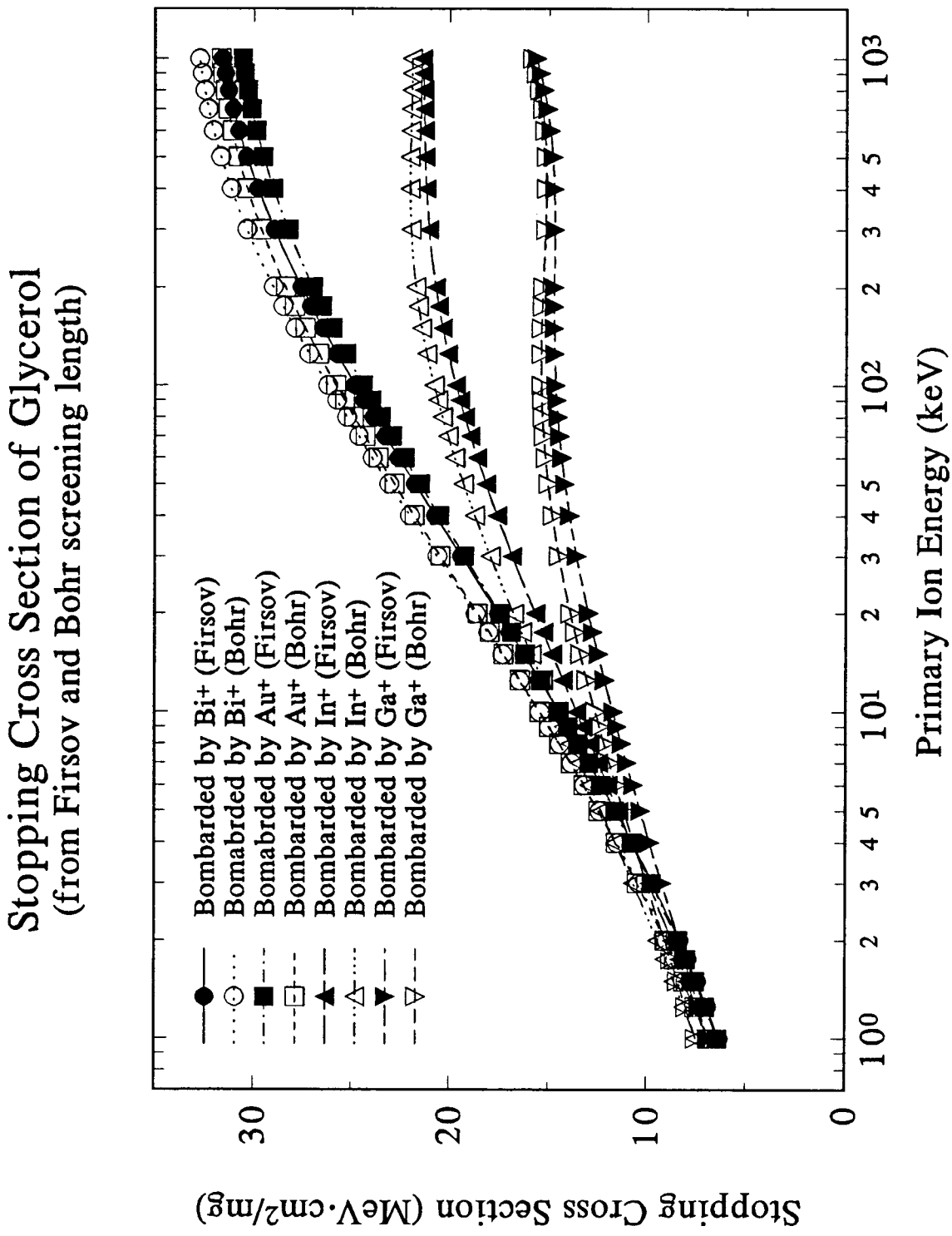

Figure 5-2: Stopping cross section of glycerol for Wilson's and Thomas-Fermi's potential

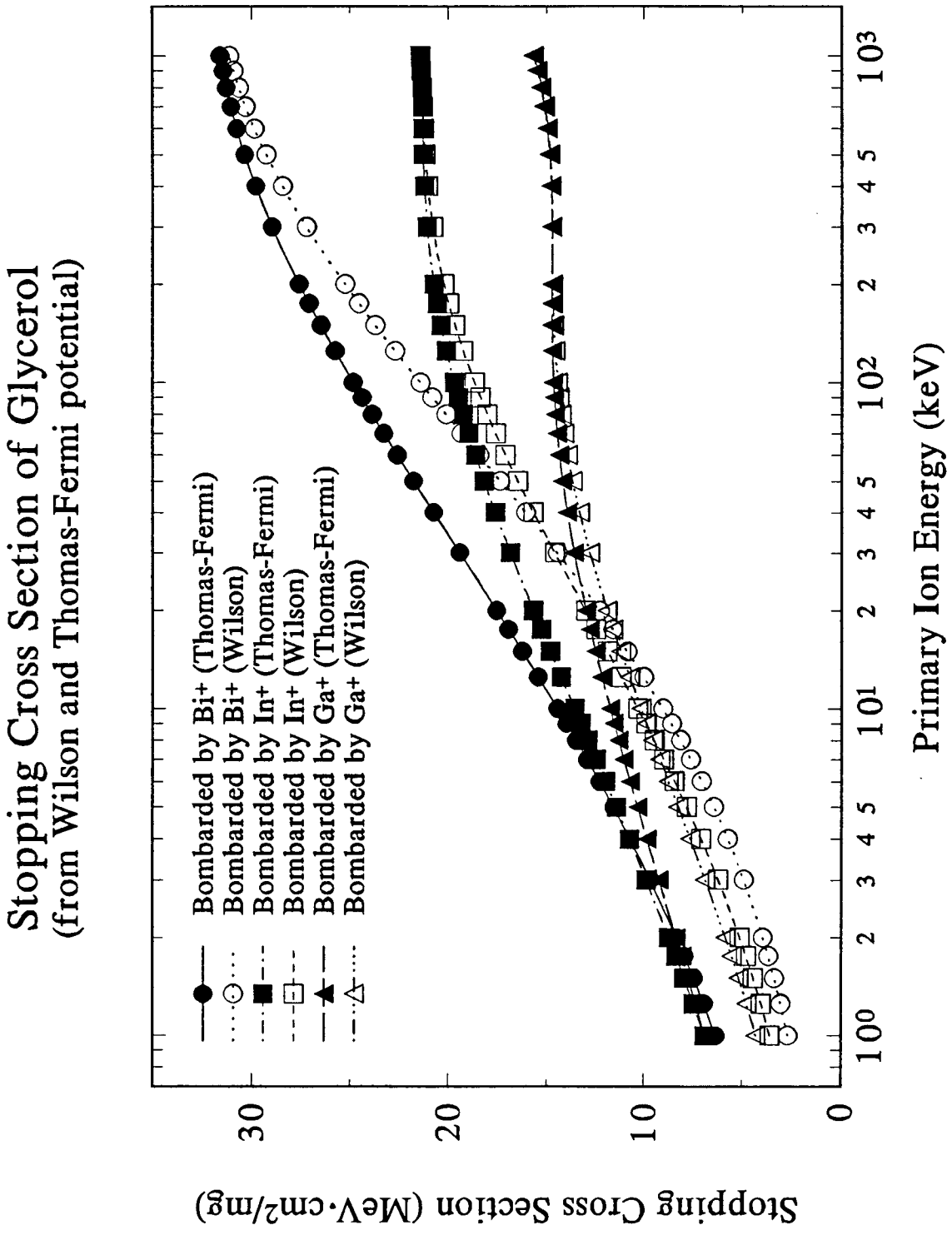

However, at low ion energies (< 30keV), the total stopping cross sections calculated from the Wilson potential for Bi^+ in glycerol become smaller than those for In^+ at the same energy. Moreover, for ion energies less than 6 keV, the total cross sections calculated from the Wilson potential for Ga^+ in glycerol become larger than those for In^+ or Bi^+. These predictions are difficult to reconcile with experimental fact that analyte yields produced by bombardment with Ga^+ are is smaller than those produced by bombardment with In^+ or Bi^+ (Figures 4-26).

We have also calculated the total stopping cross sections for glycerol using a Ziegler[52] potential; the results are shown in Figure 5-3. The numerical expressions for Ziegler's screening Coulombic length, a, and reduced nuclear stopping cross section, $s_n(\varepsilon)$, are different from those of Wilson et al.[51]; the former are given respectively by

$$a = \frac{0.4693}{Z_1^{0.23}+Z_2^{0.23}} \quad (\text{Å}), \tag{5-3}$$

$$s_n(\varepsilon) = \frac{\ln(1+1.1383\varepsilon)}{2(\varepsilon+0.01321\varepsilon^{0.21226}+0.19593\varepsilon^{0.5})} \tag{5-4}$$

where $\varepsilon = aM_2E_0/Z_1Z_2e^2(M_1+M_2)$. Agreement between the total cross sections obtained for glycerol from Ziegler's potential and those from the Thomas-Fermi potential is better than that between the results from Wilson's potential and the Thomas-Fermi potential in the low ion energy region.

In this dissertation, we calculate the nuclear stopping cross sections for glycerol

Figure 5-3: Stopping cross section of glycerol for Ziegler's and Thomas-Fermi's potential

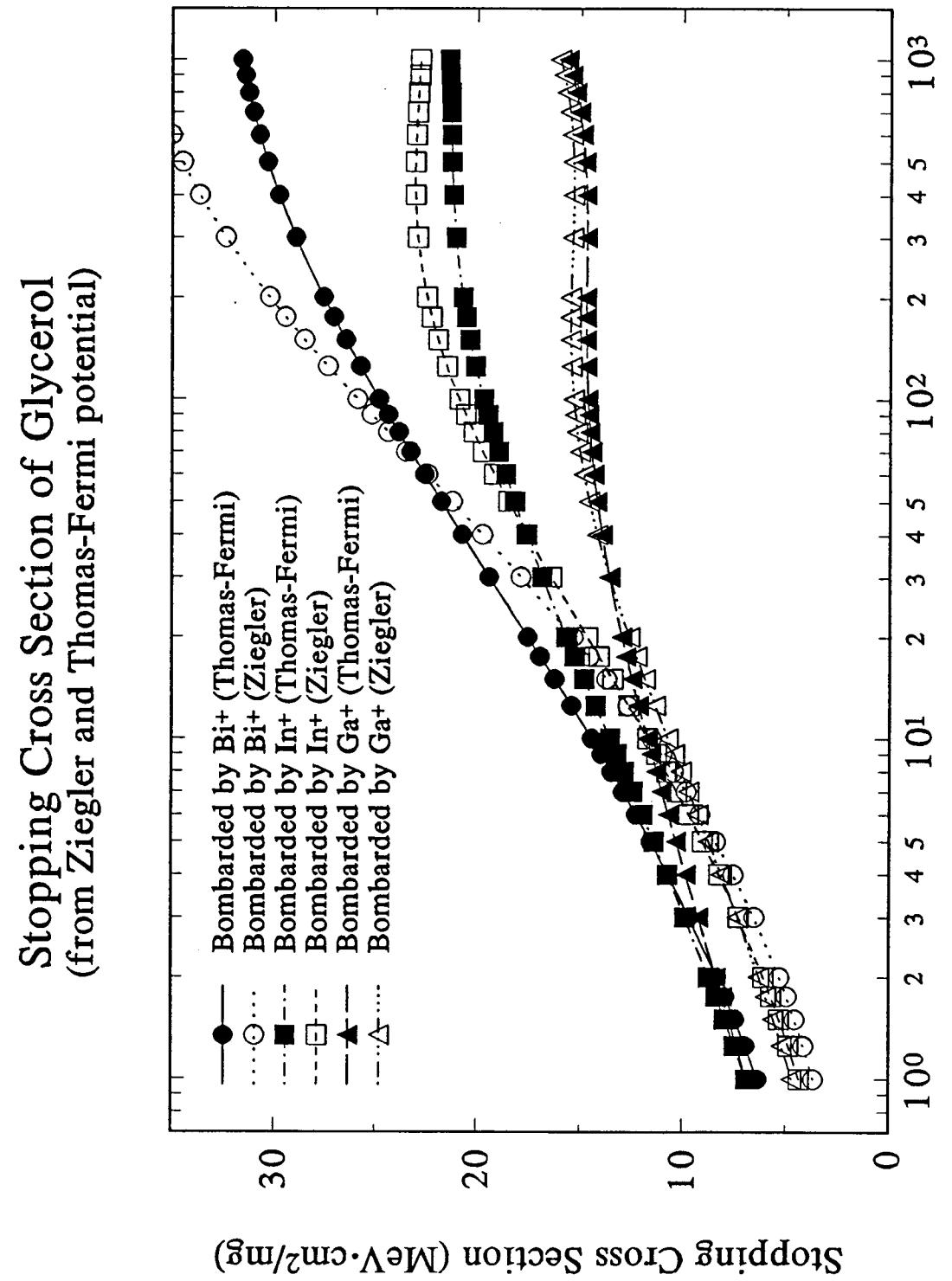

using the Thomas-Fermi potential. Some evidence for systematic errors that derive from use of the Thomas-Fermi potential with some experimental results have been reported[63,82]. But in the case of $Z_1 >> Z_2$, or $Z_2 >> Z_1$, Lindhard et al.[50] have pointed out that calculation of nuclear stopping cross sections based on the Thomas-Fermi potential gives better results. This corresponds to our experimental situation where we employ heavy primary ions (Bi, Au, In and Ga) to bombard organic compounds composed mostly of H, C, N, and O atoms. Even in the case of Ga, the primary ions are still considerably heavier than even O atoms so that the Thomas-Fermi potential is still the best choice in comparison with the other two potential.

5-2. Mechanism of secondary ion emission

In this section, we will examine, from a mechanistic point of view, our experimental results with dAMP and dGMP in a 10 mM HDPA/glycerol.

In chapter 1, we reviewed some of the experimental observations on ion sputtering from organic solids bombarded by keV or MeV primary ions. As we pointed out in that chapter, one of the difficulties in quantitatively explaining those results is due to the complexity of the chemical environment at the surface of the target. The phenomenon of secondary ion emission from a liquid organic matrix, such as glycerol, is important in practical applications of mass spectrometry but, is more complicated to interpret in some respects than that of emission from a solid substrate. For example, the

question of where the secondary ions are formed, i.e. in the bulk, on the surface, in the selvedge, or in the gas phase, during particle bombardment is still strongly debated for most analyte/matrix system. Surface activity is one of parameters that gives prominent effects on the secondary ion emission from a liquid matrix. Hexadecylpyridinium acetate (HDPA), a surfactant with a high surface activity, present in a matrix of glycerol with an anionic analyte, such as a mononucleotide, can increase the detection limit over 1000 -fold. Results demonstrating this dramatic effect for mononucleotides were shown in section 4-6.

A surfactant is composed of two major functional groups. First, it has a polar functional group which is soluble in a polar solvent such as water or glycerol. Second, it has a non-polar functional group, such as a long alkane chain, that is relatively insoluble in a polar solvent. Surfactants come in two general forms: ionic and non-ionic. An ionic surfactant has a charged polar functional group whereas a non-ionic surfactant has a neutral polar functional group. HDPA is an ionic surfactant. When HDPA is present in a glycerol matrix, it forms a hexadecylpyridinium cation that is highly active on the surface of the matrix, and an acetate anion that is solvated in the matrix.

A simple model to explain the enhancement of the yields of deprotonated mononucleotides from a matrix of HDPA in glycerol is that the negatively charged phosphate functional group of nucleotides forms ion pairings with the

hexadecylpyridinium cations adsorbed on the surface and, thus increases the number of analytes, e.g. dAMP or dGMP, available on the surface for sputtering. Although this model probably oversimplifies the chemical interaction between the mononucleotides and the HDPA in glycerol the matrix, it does qualitatively account for the increased intensity of deprotonated mononucleotides sputtered from a matrix of 10mM HDPA in glycerol over that from a pure glycerol matrix. Ligon et al.[83,84,85] have tested several surfactants with several different analytes and have pointed out numerous features of surfactant in glycerol matrices. However, the number of analytical applications using surfactants with biomolecules is still very limited. The detailed interaction between HDPA and mononucleotides is the subject of another study.[91]

For the purposes of studying the physical processes of sputtering from liquids, mononucleotides in a matrix of HDPA/glycerol provide a system that has two advantages: 1) the analyte already exists as an ion in the matrix, thus, making the chemistry of ionization to a large degree independent of the physics of sputtering and 2) the analyte is highly concentrated near the surface of the target, thus, providing a situation somewhat analogous to a monolayer or less of analyte adsorbed on a solid. We make the assumptions, therefore, that the secondary ion emission we observe from our system is primarily the result of the energizing mechanisms instigated by particle bombardment and, furthermore, that the chemical environment at the surface of the target is independent of the energizing mechanisms and can be treated as a complex surface binding state. Overall, these assumptions are tantamount to assuming that ion

sputtering from this system is representative of overall sputtering.

In chapter 2, we discussed the thermal spike model, an energizing mechanism based on the rapid deposition or spiking of a primary ion's energy into a cylindrical volume at the target surface. The sputtering yield Y is given in equation 2-22. The yield Y is expressed as an integral over the surface affected by the energizing spike, therefore, indicating a surface desorption processes. However, if the sputtered particles originate from the volume of the energizing spike rather than the surface then a spherical spike model is more proper appropriate since it expresses the yield of sputtered particles as an integral over the energizing volume. For a spherical spike, equations 2-21 and 2-22 need be rewritten as

$$T(x,t) = \frac{\varepsilon}{(4\pi\kappa t)^{\frac{3}{2}}} e^{\frac{-cx^2}{4\kappa t}}, \tag{5-5}$$

$$Y_S = \int_0^\infty 4\pi x^2 \, dx \int_0^\infty \psi \, dt \tag{5-6}$$

where Y_S is the sputtering yield. Following the same procedure as for a cylindrical spike, we can evaluate equation 5-6 to obtain

$$Y_S = \frac{0.022A\varepsilon^{\frac{5}{3}}}{\kappa C^{\frac{2}{3}} Q^{\frac{5}{3}}} \tag{5-7}$$

A detailed treatment of spherical spike can be found in references 67 and 69.

From equations 2-27, 2-28, and 2-29, we can deduce the sputtering yield induced by cylindrical spike is proportional to the square of the rate of energy deposition into matrix providing this deposited energy is much higher than the surface sublimation energy, U. This is based on the concept that simple bond breaking processes at the surface are the ultimate result of particle bombardment. In this case equation 2-28 simplifies to

$$Y = k_1\left(\frac{(\frac{dE}{dX})}{U}\right)^2 \tag{5-8}$$

where k_1 is a constant and dE/dX is the stopping power of the target.

All of our measurements were performed on the same sample system under various bombardment conditions; hence, U was constant within experimental limits. Under these circumstances, we can further simplify equation 5-8 to

$$Y = k_2\left(\frac{dE}{dX}\right)^2 \tag{5-9}$$

where k_2 is a constant.

In our calculation, we assume that the stopping cross section of the target is the sum of the nuclear stopping cross section and the electronic stopping cross section of glycerol, and that the energy spiked into the matrix is proportional to the total stopping

cross section multiplied the atomic density of the matrix. Based on the above models, our measurements should indicate the origin of the bulk of the particles sputtered from a glycerol matrix. If most of the sputtered particles originate from the target's surface region, we would expect the measured ion yields, which are assuming to be proportional to the total sputtering yields, to scale quadratically with the total stopping cross section. On the other hand, if a large fraction or most of the sputtering particles originate from the bulk, we would expect the measured ion yields to scale with stopping cross section to a significantly higher[31] or lower[69] power than 2. We like to point out that the atomic density of matrix is unchanged in our experiments; therefore, to be simplicity, we express all the rate of energy deposition (stopping power) in our analysis with the unit of stopping cross section.

Figure 5-4 shows the yield of deprotonated dAMP for a matrix of 10 mM HDPA mixed with glycerol as a function of the total stopping cross section of the matrix. The data were generated by bombardment with 17-66 keV monoatomic ions (Bi^+, Au^{+2}, Au^+, In^+, and Ga^+). The solid line is a fit of

$$Y = k\left(\frac{dE}{dX} - S_0\right)^n \tag{5-10}$$

where k is a constant and dE/dX is the total stopping cross section of the matrix for a given energy of primary ion, and S_0, threshold stopping cross section. Equation 5-10 is an empirical formula that has been employed by Brandl et al.[23]. The physical significance of S_0 is based on experimental reported by Dück[86]. He found that no intact

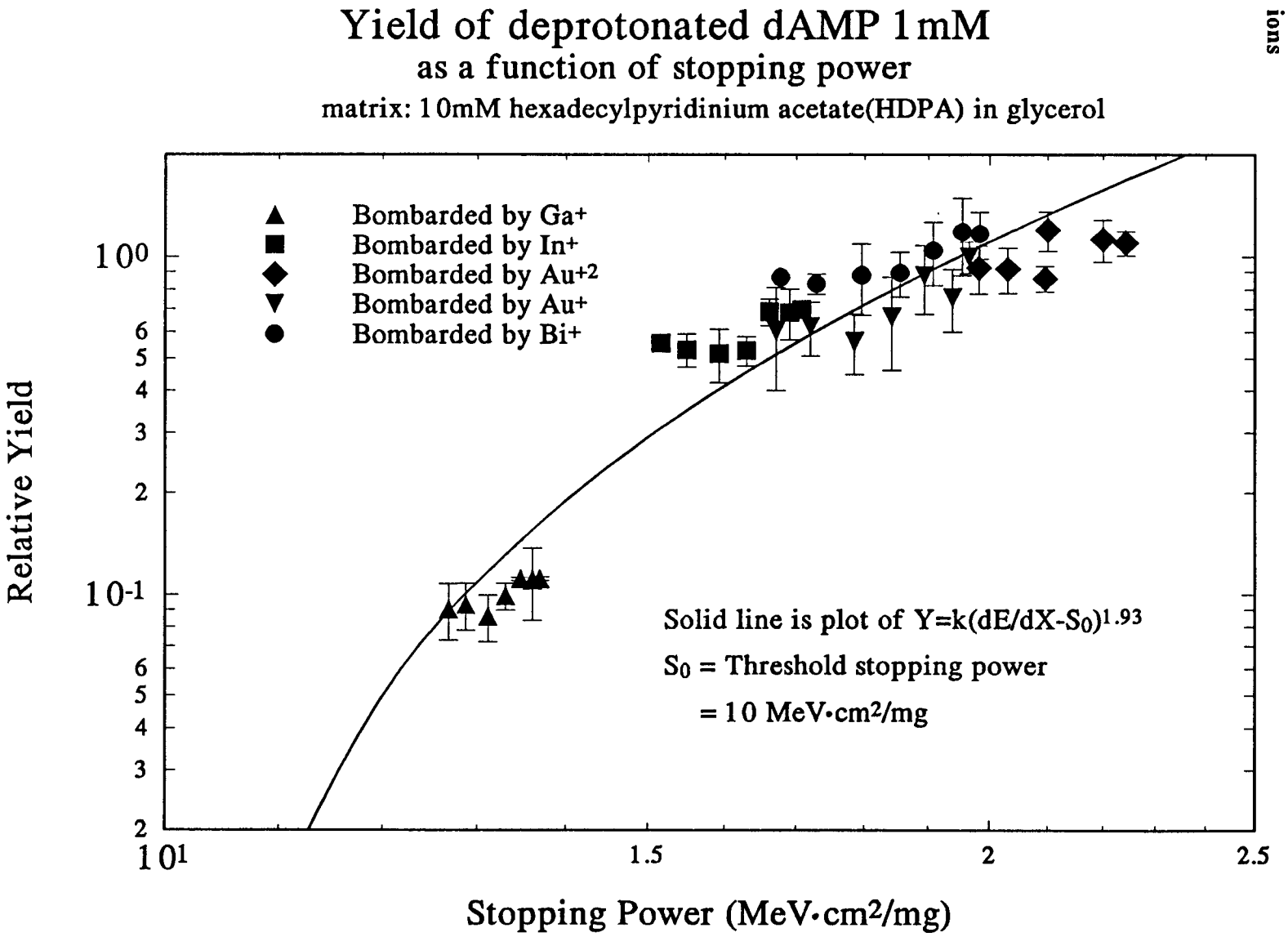

Figure 5-4: Yield of dAMP as a function of stopping power for monoatomic ions

ions desorb from a valine sample bombarded by α particles unless the stopping power of the substrate is greater than 1.5 MeV•cm^2/mg. In a theoretical argument, Sigmund[44] pointed out that the energy deposited per unit volume for a given sputtering event must exceed a certain minimum in order to generate a spike. Thus, both independent experimental evidence and theoretical argument support the use of equation 5-10 as a guide to interpret our experimental results. The fit to equation 5-10 for the experimental yield of deprotonated dGMP (MW=346) from a matrix of 10 mM HDPA is shown in Figure 5-5.

It is again clear from Figures 5-4 and 5-5 that the yields generated by bombardment with Ga^+ are significantly lower than those generated by bombardment with In^+, Au^+, and Bi^+. The same trend can be found for positive ions; Figure 5-6 shows the yield of the hexadecylpyridinium cation from the same sample as in Figure 5-4. The values of the fitted parameters obtained from Figures 5-4, 5-5, and 5-6 are summarized in Table 2.

As was shown with the raw data presented in section 4-6, the intensity of $(HDPA-59)^+$ is about 10 times stronger than the intensity of deprotonated dAMP or of deprotonated dGMP. The fitting errors for the constant k, S_0, and n for the positive ion data in Figure 5-6 are significantly larger than those for the negative ion data in Figures 5-4 and 5-5. This may result from the incident angle effects of the primary ion beam that were discussed in section 3-7. From Figure 3-18, we see that with a positive source

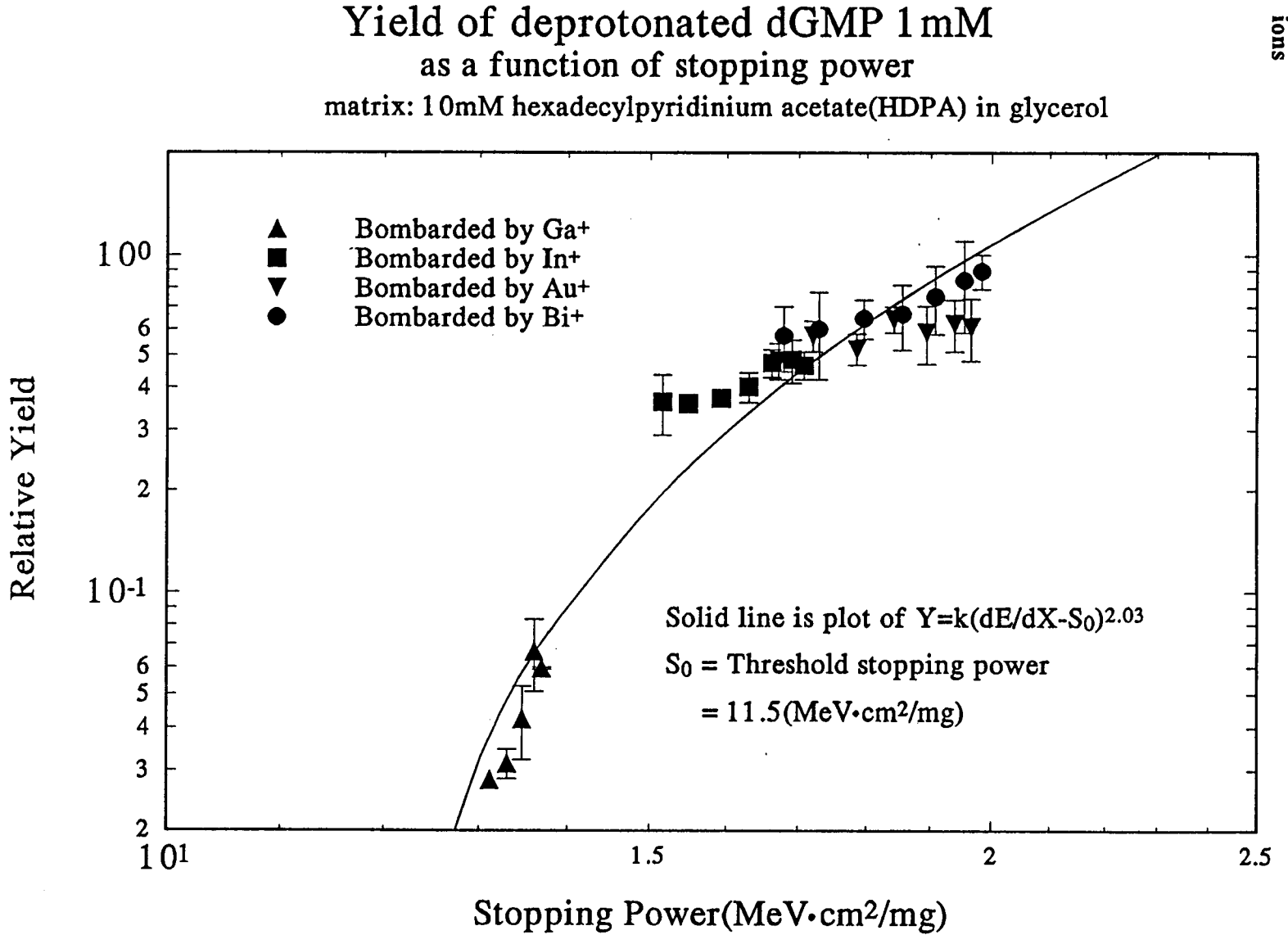

Figure 5-5: Yield of dGMP as a function of stopping power for monoatomic ions

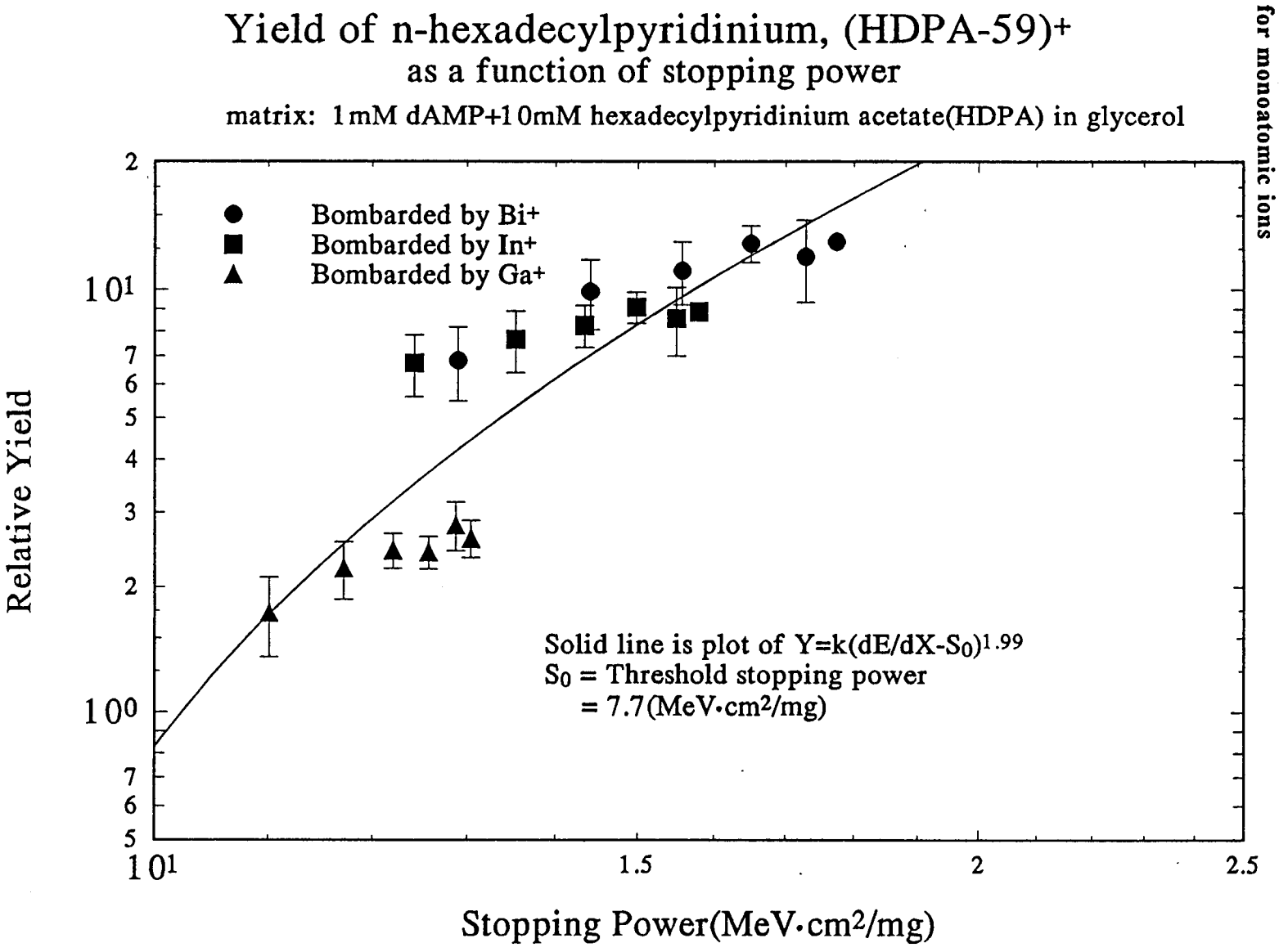

Figure 5-6: Yields of $(HDPA-59)^+$ as a function of stopping power of glycerol for monoatomic ions

Table 2: Summary of parameters from equation 5-10 used to fit the experimental yield curves

Figure	Yield Y	Constant k	Threshold ** S_0 MeV•cm^2/mg	Exponent n
5-4	deprotonated dAMP	0.013±0.003	10	1.93±0.11
5-6	deprotonated dGMP	0.014±0.002	11.5	2.03±0.11
5-7	(HDPA-59)	0.159±0.06	7.7	1.99±0.26
5-8	(HDPA-59)*	0.130±0.02	9	1.97±0.1
5-9	(HDPA-59)#	0.118±0.02	9.4	2.00±0.11

* Y normalize with $(\cos\theta)^{-1}$

Y as a function of the total stopping cross section of HDPA

**Threshold are selected as the initial fitting values.

voltage of 6kV that the incident angle of the primary ion varies from 50° to 75° as the energy of primary ion is changed from 27 keV to 13 keV. If yield is proportional to inverse of cosine, then Y(75°)= 2.5 Y(50°). The data shown in Figure 5-6 do not take this incident angle effect into account, but the data plotted in Figure 5-7 do. By correcting for incidence angle, we find that the yields of $(HDPA-59)^+$ generated by bombardment with lower energy Bi^+ and In^+ are more consistent with those generated by bombardment with higher energy Ga^+. Moreover, the fitting constants from Figure 5-7 have smaller errors than those from Figure 5-6. The fitting parameters obtained from Figure 5-7 are also listed in Table 2.

So far, our analysis of secondary ion yields as a function of the total stopping cross section has been based on the total stopping cross section of glycerol as the target medium. It is reasonable to argue that we should use HDPA as the target medium because most of the surface of the target is composed of HDPA. However, the stopping cross section of HDPA is only a little bit higher than that the stopping cross section of glycerol. Figure 5-8 show the yield of $(HDPA-59)^+$ cation scaled to the total stopping cross section of HDPA; the fitting constants are also listed in Table 2 for comparison. We can clearly see that this scaling only increases the absolute value of the threshold stopping power by 0.4 $MeV \bullet cm^2/mg$ and has no significant effect on the other parameters.

We take the data presented in Figures 5-4 through 5-8 and summarized in Table

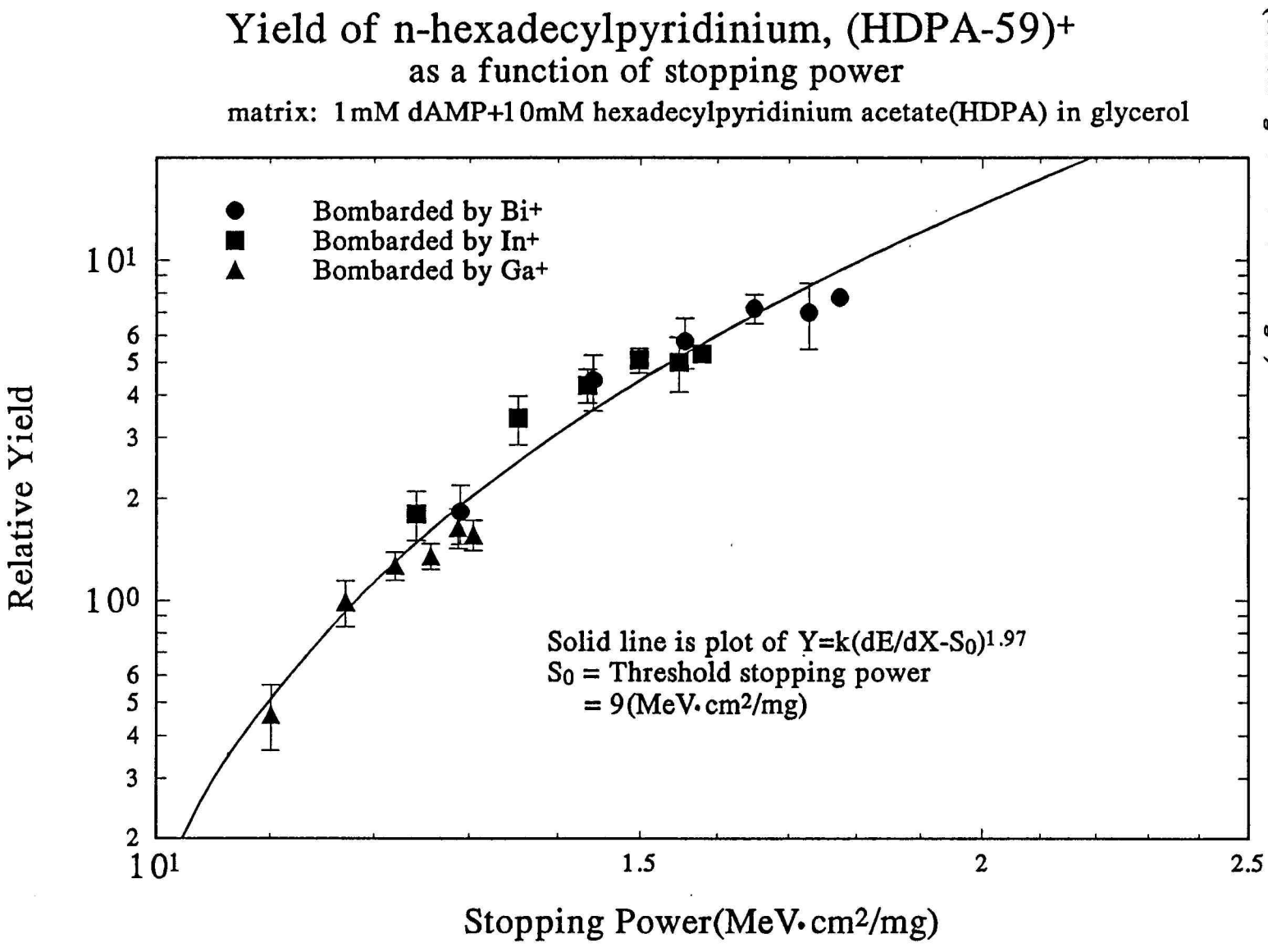

Figure 5-7: Yields of $(HDPA-59)^+$ as a function of stopping power of glycerol (correcting for incidence angle) for monoatomic ions

Figure 5-8: Yields of $(HDPA-59)^+$ as a function of stopping power of HDPA for monoatomic ions

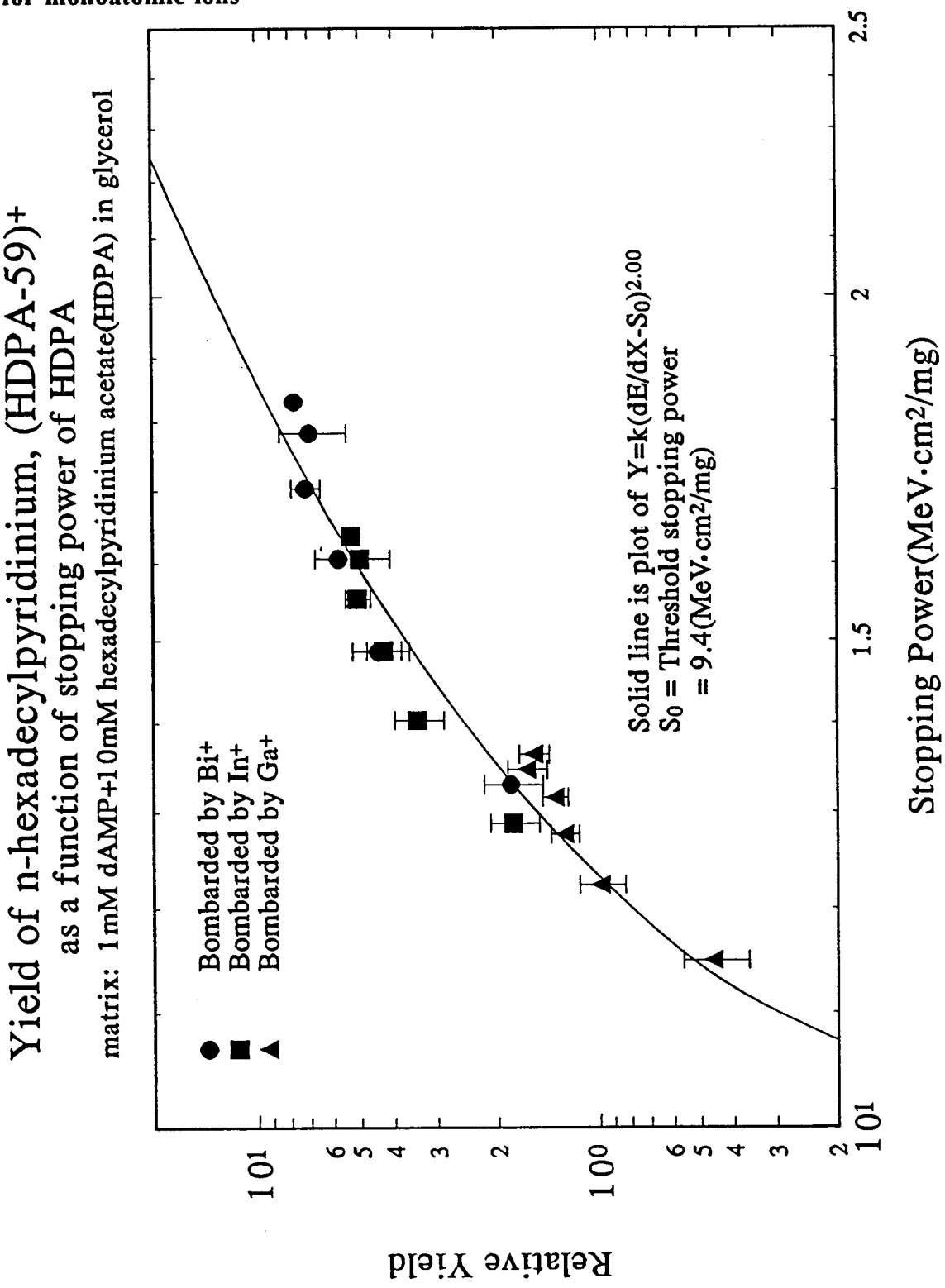

2 to indicate that sputtering from liquid organic matrices occurs primarily from the surface and models such as the cylindrical thermal spike model, that predict surface sputtering with a threshold stopping cross section are consistent with our measurements.

In order to account for secondary ion emission based on a model, such as the cylindrical thermal spike model, assumes that preexisting ions bound on the surface of the target are desorbed following simple bond breaking processes activated by particle bombardment. This almost certainly oversimplifies the actual bonding state of a preexisting ion on the surface of a target medium. However, Lucchese[90] has described a thermal spike model for heavy ion induced desorption from a surface based on this idea that the desorption of a molecule is the result of a serial sequence of bond breaking steps; he concluded that there is no significant difference between breaking a single bond and breaking 5-10 bonds. According to this result, it is reasonable to model the desorption of a molecule as a single bond breaking process.

All the results and conclusions presented in the proceeding paragraph are for bombardment by monoatomic primary ions. The relative intensities of deprotonated dAMP and deprotonated dGMP generated by bombardment with polyatomic primary ions (Bi_3^{+2}, Bi_2^+, Au_2^+, Au_3^+) were also presented in Chapter 4 (Figures 4-27).

For a linear system, we would expect the secondary ion yield generated by bombardment with a cluster ion to be equal to the sum the yield produced by a

monoatomic primary ion multiplied by the number of atoms in the cluster ion. This is expressed by the following linear yield relation for a homonuclear cluster:

$$Y_n(E) = n\,Y(E/n) \qquad (5\text{-}11)$$

where $Y_n(E)$ is the secondary ion yield generated by bombardment with a cluster ion composed of n atoms, E is the total energy of the cluster ion, and $Y(E/n)$ is the secondary ion yield generated by bombardment with a monoatomic ion of energy E/n. Figures 5-9 and 5-10 show the polyatomic and monoatomic bombardment data for dAMP and dGMP, respectively, corrected for primary ion incidence angle and replotted as a function of primary ion velocity squared (keV/amu). Table 3 summaries the results of the yields of deprotonated dAMP and deprotonated dGMP generated by bombardment with polyatomic ions and monoatomic ions with a nearly the same primary ion velocity. The yields of both deprotonated dAMP and deprotonated dGMP generated by bombardment with diatomic or triatomic ions (Bi_3^{+2}, Bi_2^+, Au_2^+) are about 5-20 times larger than those generated by bombardment with monoatomic ions (Au^+, Bi^+) at the same velocity. We have managed to make measurements for the monoatomic ions and the polyatomic ions over a portion of the velocity range studied. This allow us to compare the difference in the secondary yields generated in these two cases when each component atom in a cluster ion has exactly the same energy as its monoatomic counter part.

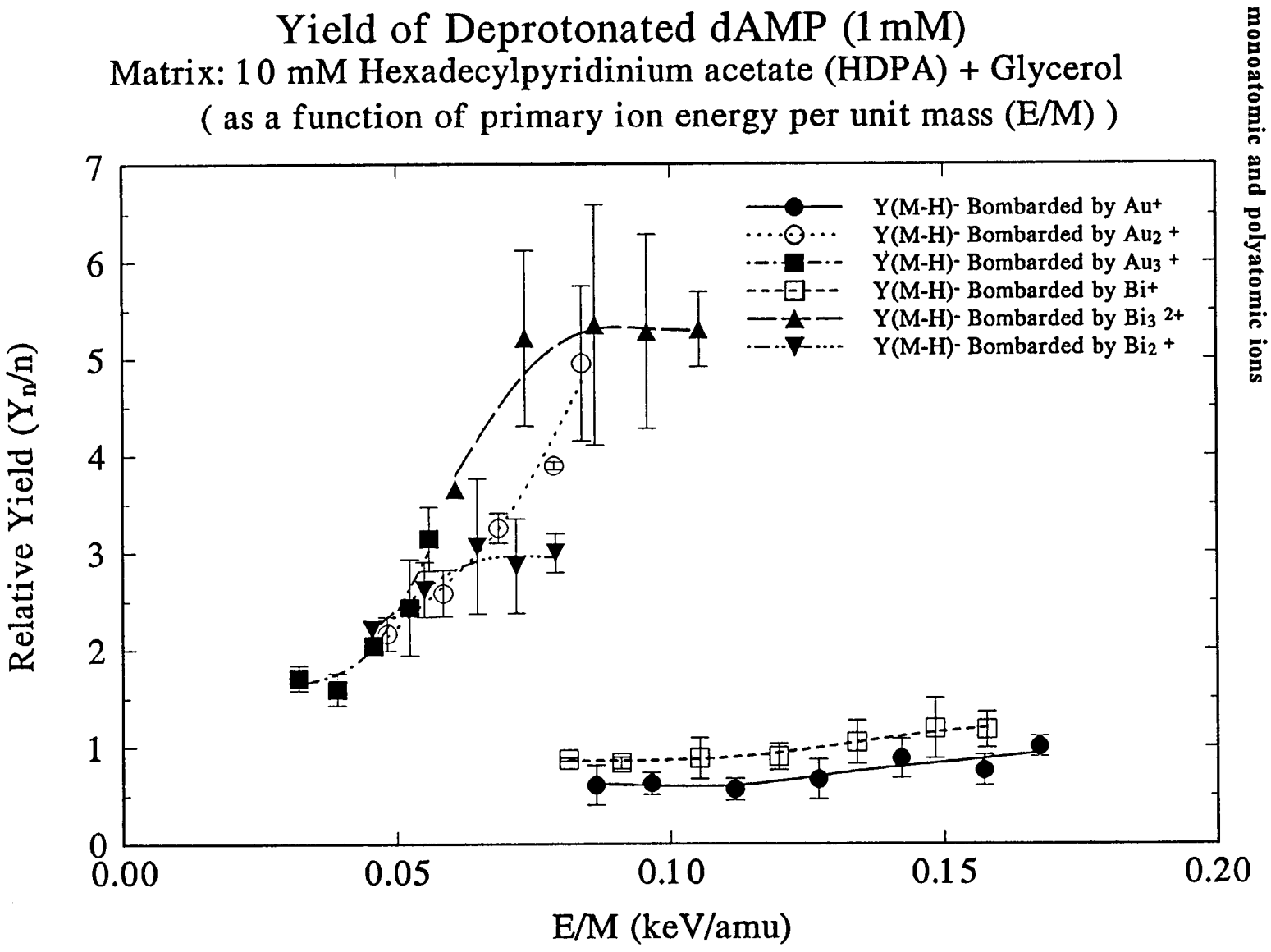

Figure 5-9: Yield of dAMP as a function of primary ion energy for monoatomic and polyatomic ions

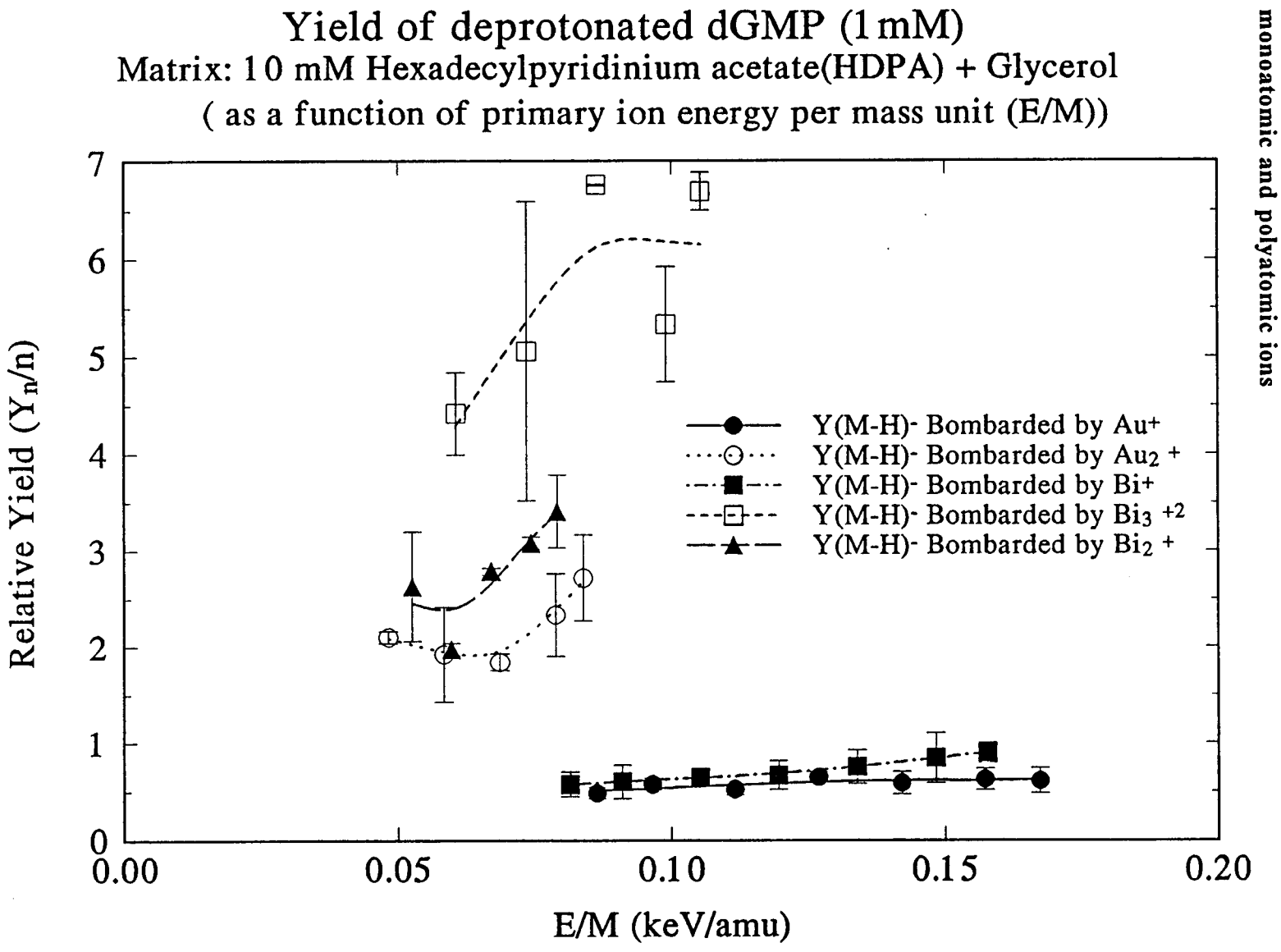

Figure 5-10: Yield of dGMP as a function of primary ion energy for monoatomic and polyatomic ions

Table 2: Yields of deprotonated dAMP and deprotonated dGMP bombarded by monoatomic ions (Au^+, Bi^+) and polyatomic ions (Au_2^+, Bi_3^{+2}, Bi_2^+).

Yield of deprotonated dAMP(Y_n, Y)

primary ion	velocity (10^7 cm/s)	yield(Y_n, Y)	Y_n/Y	Y_n/nY
Bi_2^+	1.23	5.99±0.4	6.9	3.5
Bi^+	1.25	0.87±0.1		
Bi_3^{+2}	1.42	15.9±1.16	18.1	6
Bi^+	1.42	0.88±0.21		
Au_2^+	1.27	9.90±1.60	16.2	8.1
Au^+	1.29	0.61±0.21		

Yield of deprotonated dGMP(Y_n, Y)

primary ion	velocity (10^7 cm/s)	yield(Y_n, Y)	Y_n/Y	Y_n/nY
Bi_2^+	1.23	6.81±0.75	11.9	6
Bi^+	1.25	0.57±0.13		
Bi_3^{+2}	1.42	20.09±0.59	30.9	10.3
Bi^+	1.42	0.65±0.09		
Au_2^+	1.27	5.44±0.9	11.3	5.7
Au^+	1.29	0.48±0.06		

Obviously, the results in Figures 5-9 and 5-10 do not indicate linear sputtering process expressed in equation 5-11 because $Y_n(E) > nY(E/n)$.

The next question is whether the nonlinear enhancement in the yield of deprotonated dAMP and deprotonated dGMP produced by bombardment with cluster ions can be explained in terms of a surface ejection model, such as the cylindrical thermal spike model. The thermal spike model is based on the assumption that the energy deposited is proportional to the stopping power of the target medium for the incident primary ion. In the case of monoatomic ion bombardment, the calculation of the stopping power is straight forward, but the calculation of the stopping power under polyatomic ion bombardment is more complicate.

Shulga et al.[87], Yammamura[88], and Sigmund[89] have all used molecular dynamics simulations to examine the sputtering of neutral particles by polyatomic primary ions from condensed state targets (metals and semiconductors). These simulations indicate that for a keV incident cluster ion containing a large number of atoms (>10) and for $M_1 > M_2$, where M_1 and M_2 are the masses of an atom in the incident ion and the target atom respectively, the stopping power (nuclear stopping) per atom of the cluster ion is smaller than the stopping power of a corresponding monoatomic ion. On the other hand, Salehpour et al.[35] observed a nonlinear enhancement in the yield of deprotonated valine generated by bombardment with heteronuclear cluster ions (CH_3^+, CO_2^+, CF^+, CF_3^+, and $C_3F_5^+$) and with homonuclear cluster ions (C_2^+, and O_2^+) in the energy range 600keV-

3.7MeV for which they reported that the stopping power (electronic) per atom in a cluster ion was greater than the stopping power of corresponding monoatomic ion.

Figures 5-11 and 5-12 show plots of the monoatomic data for dAMP and dGMP, respectively, expanded to include the results from polyatomic ion bombardment. In order to make these plots we have assumed that the stopping power for the cluster ion is equal to the sum of the stopping powers for the individual atoms in the cluster. The solid curves are not refits to the new larger data set, but are simply extrapolations of the fitted curves in Figure 5-4 and 5-5 respectively. The yields of deprotonated dAMP and dGMP generated by bombardment with polyatomic ions clearly fit well to the extensions of the curves generated by bombardment with monoatomic ions. Hence, it seems that the assumption of additive stopping powers for the constituent atoms in a cluster and of surface sputtering models, such as the cylindrical thermal spike model, that predict sputtering yield in accordance with equation 5-10 are self consistent, at least in case of intact, molecular ions.

Not all of the ion yields from the same analyte/matrix system show a quadratic dependence on stopping power. Figure 5-13 shows the ion yields of deprotonated dAMP and of H^- as a function of stopping power, and Figure 5-14 shows the ion yields of deprotonated dGMP and of H^- as a function of stopping power. In the both cases, the yield of hydride ion $(H)^-$ shows a nearly linear dependence on the stopping power with essentially no threshold. Figure 5-15 and 5-16 show that yields of H^-, generated

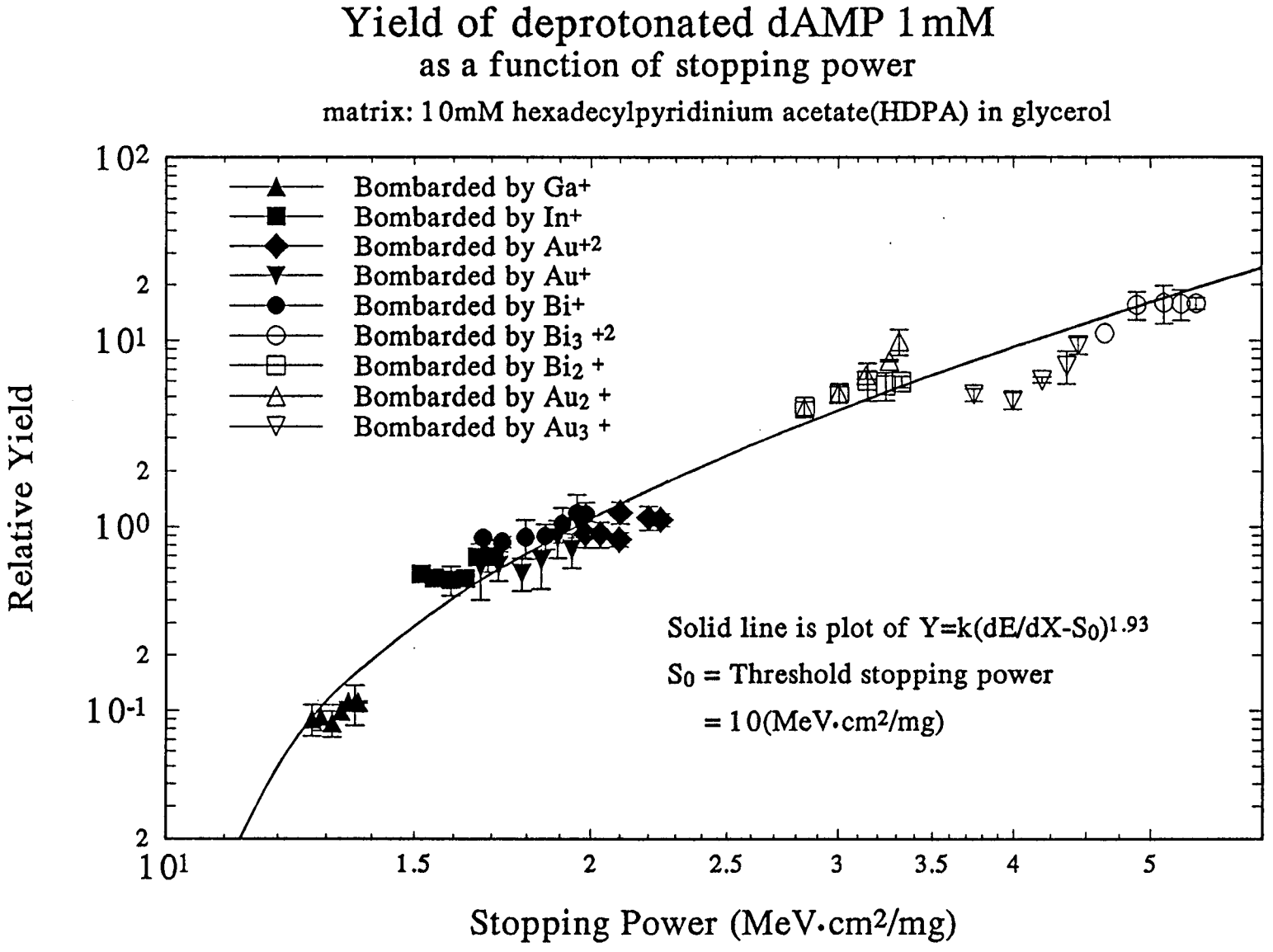

Figure 5-11: Yield of dAMP as a function of stopping power for monoatomic and polyatomic ions

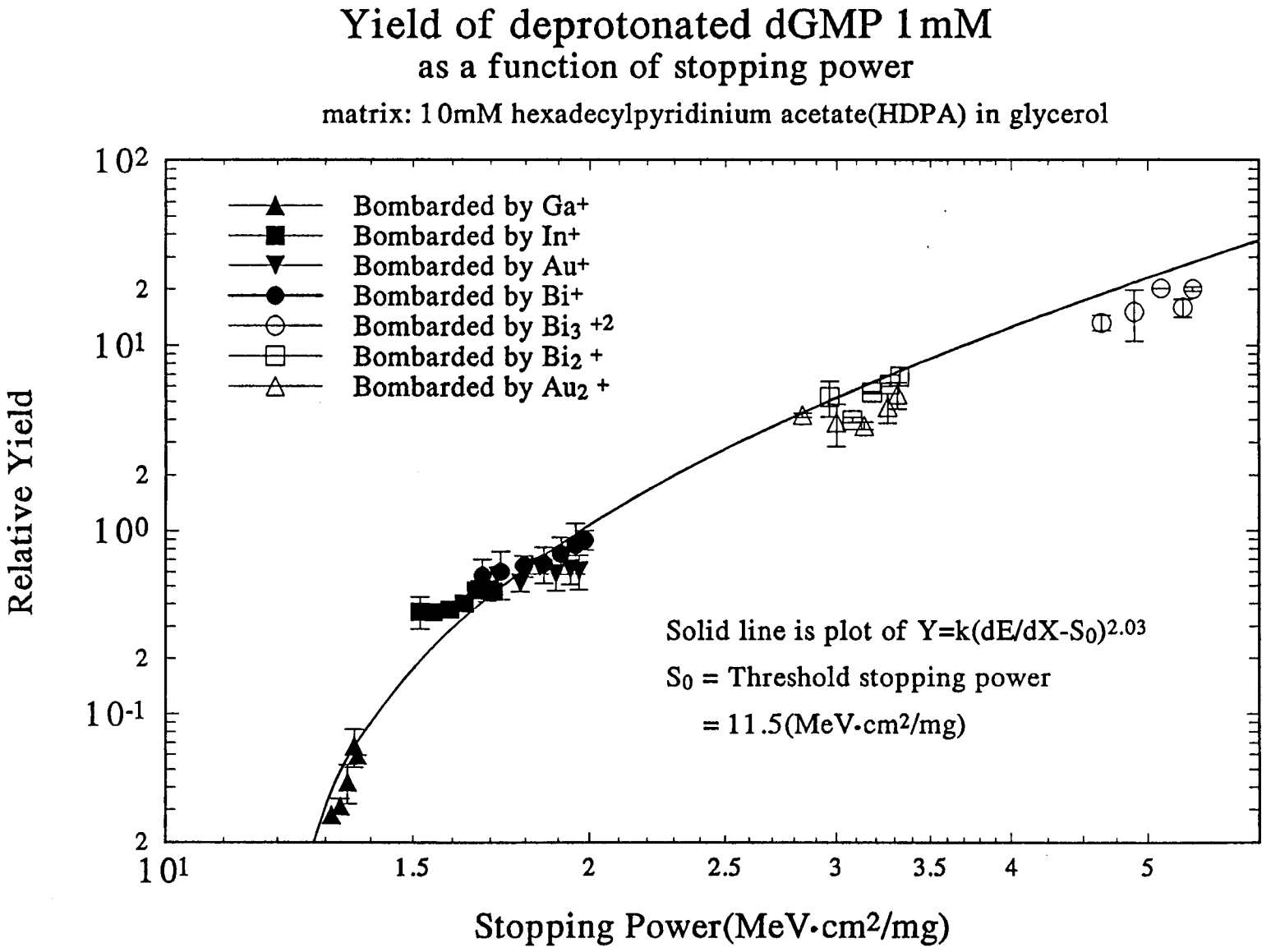

Figure 5-12: Yield of dGMP as a function of stopping power for monoatomic and polyatomic ions

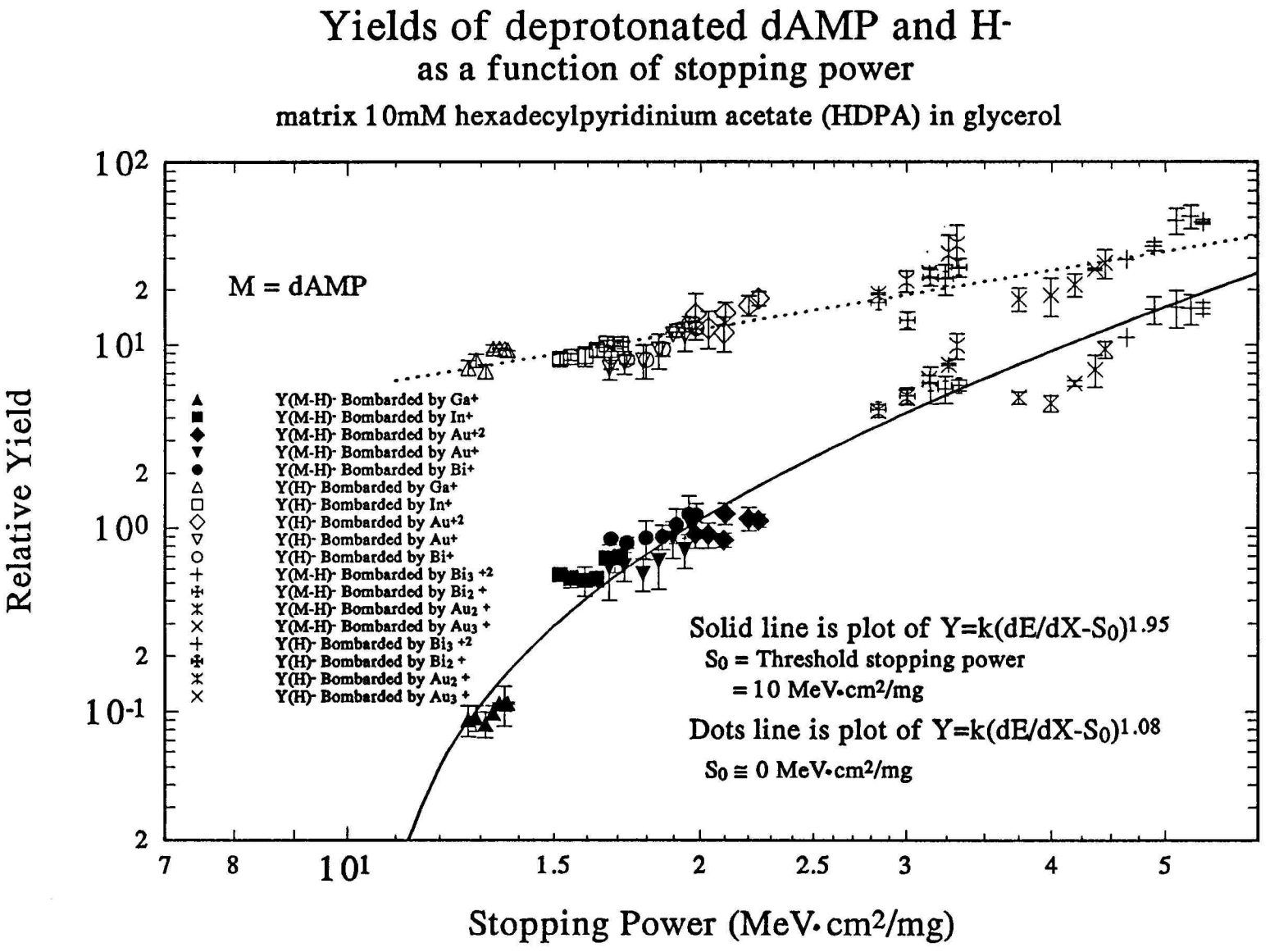

Figure 5-13: Yields of dAMP and H⁻ as a function of stopping power for monoatomic and polyatomic ions

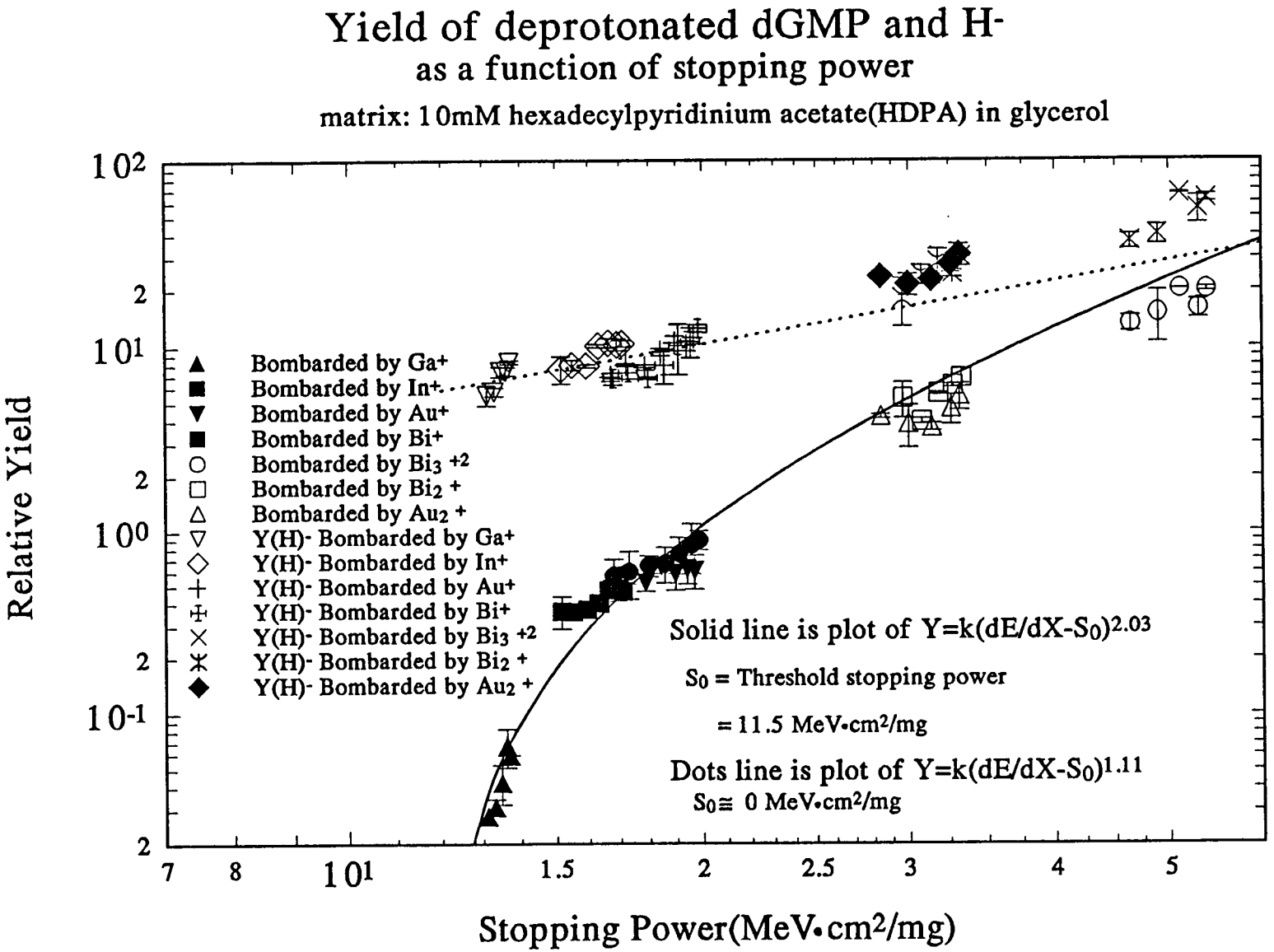

Figure 5-14: Yields of dGMP and H⁻ as a function of stopping power for monoatomic and polyatomic ions

Figure 5-15: Yield of H^- from dAMP in HDPA/glycerol matrix as a function of primary ion energy for monoatomic and polyatomic ions

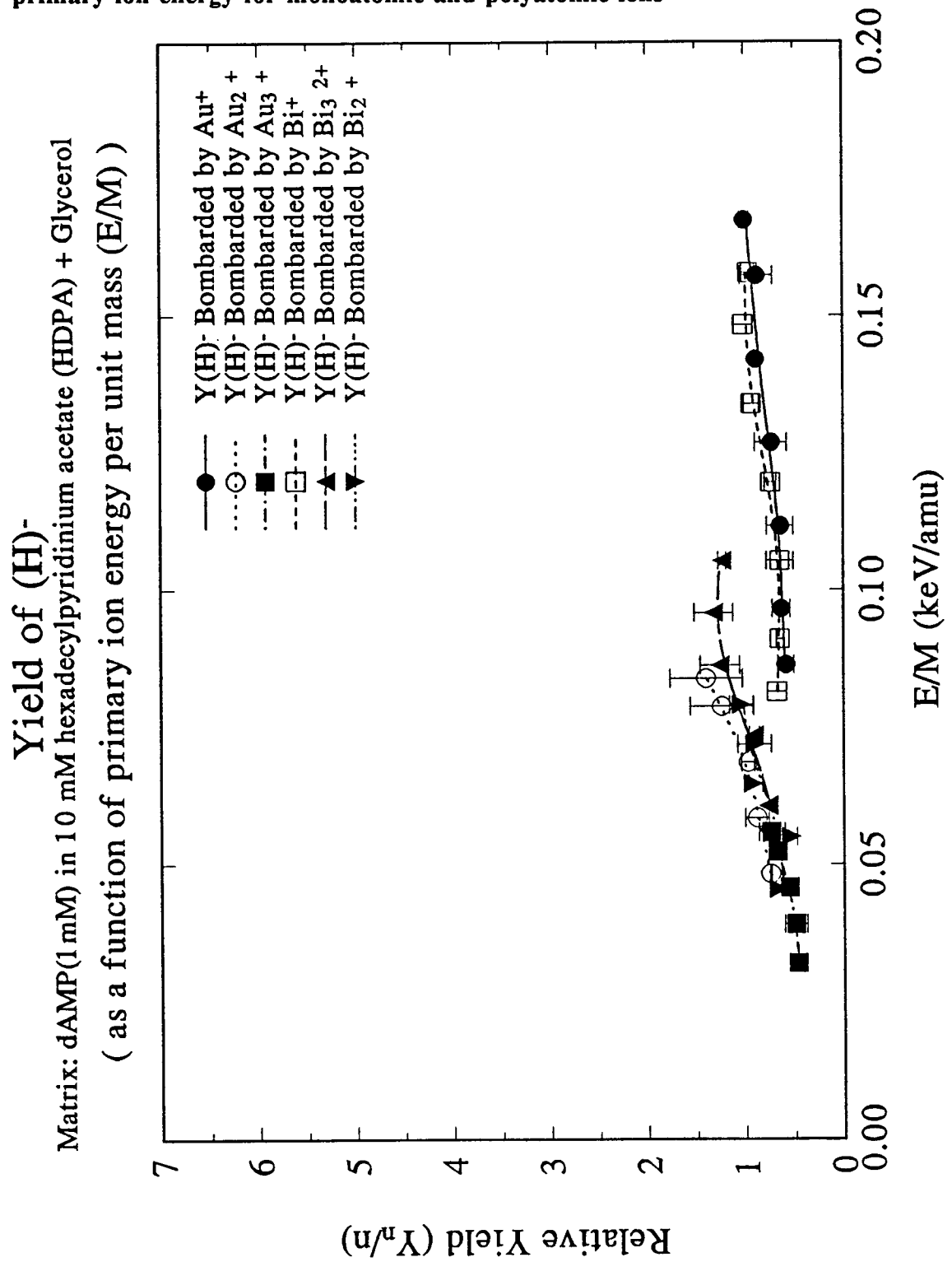

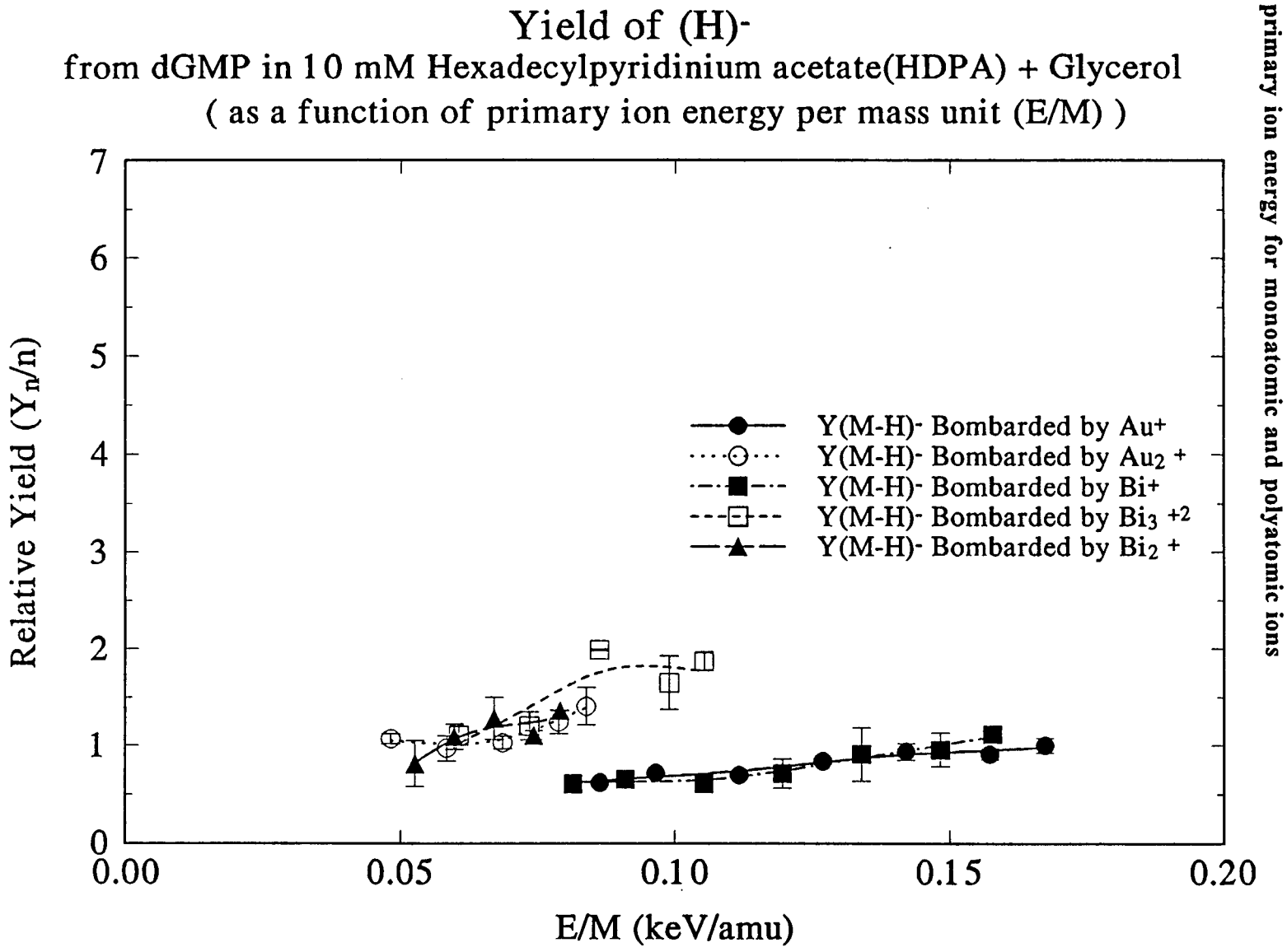

Figure 5-16: Yield of H^- from dGMP in HDPA/glycerol matrix as a function of primary ion energy for monoatomic and polyatomic ions

by bombardment with monoatomic (Au^+, Bi^+) and polyatomic ions (Bi_3^{+2}, Bi_2^+, Au_2^+, Au_3^+), from dAMP/matrix and from dGMP/matrix respectively, as a function of E/M (keV/amu). The pronounced nonlinear enhancement observed in the yields of deprotonated dAMP and deprotonated dGMP when polyatomic primary ions are used (Figures 5-9 and 5-10) are clearly not observed in the case of H^-.

5-4. Conclusions

The disappearance or damage cross section for an analyte from a liquid organic matrix was shown in Figures 4-34 and 4-35 to be significantly smaller than from a solid substrate. From the onset of the use of organic liquids as matrices in mass spectrometry, it has been generally accepted that liquids repair radiation damage to their surface by replacing damaged material with undamaged material via surface or bulk transport processes. Our measurements are the first to give a quantitative determination of the damage cross section for any liquid organic system. It is not clear at this point how general our results might be.

The yield of deprotonated mononucleotides from a matrix of HDPA in glycerol can be explained by a surface sputtering models such as the cylindrical thermal spike model, that predicts yield in accordance with equation 5-10. Providing stopping power per atom in a cluster of atoms is the same as the stopping power of an individual atom, the nonlinear enhancement of the yields of deprotonated mononucleotides generated by

bombardment with diatomic and triatomic ions are also well fitted by a surface sputtering model. Alternatively, if we accept the surface sputtering picture that there is no pronounced increase or decrease in the stopping power per atom in a cluster ion over the stopping power of a monoatomic ion. Given the unique features of our experiments system, we propose that our results should be generally valid for sputtering from liquid organic matrices.

There remain numerous unanswered questions concerning the mechanism of sputtering from organic liquids. For example, we cannot quantitatively assign a value to the surface bonding potential of the analyte, nor can we experimentally determine the fraction of the stopping power that contributes to the bond breaking processes. Perhaps even more fundamental, is the question of the relationship between ion sputtering and total sputtering in general, i.e. how representative ion sputtering is of the overall process. It would be helpful for understanding the mechanism of sputtering from organic liquids in general and secondary ion emission in particular if we can expand the energy range of our measurements up to the hundred keV range in order to distinguish the processes of energy deposition contributed by nuclear stopping power or by electronic stopping in dielectric target medium. Other experiments that would contribute to our understanding of the processes involved would include measurements of axial, radial and internal energy distributions of secondary ions. Finally, it would also be important for practical purposes to study the chemical interaction between surfactants and analytes in order to make the analytical application of particle induced sputtering from organic

liquids more generally applicable to the analysis of organic molecules, especially biomolecules.

Bibliography

1. J. J. Thomson, Philos. Mag. **20**, 752(1910).

2. R. F. K. Herzog and F. Viehboeck, Phys. Rev. **76**, 855(1949).

3. D. F. Torgerson, R. P. Skowronski, R. D. Macfarlane; Biochem. Biophys. Res. Commun. **60**, 616(1974).

4. A. Benninghoven, D. Jaspers, and W. Sichtermann, Appl. Phys. **11**, 35(1976).

5. M. Barber, R. S. Bordoli, R. D. Sedgwick, A. N. Tayler, J. Chem. Soc. Chem. Commun., 325(1981).

6. W. Alerth, K. M. Strauts, A. L. Burlingame, Anal. Chem. **54**, 2089(1982).

7. L. R. Schrok, and R. J. Cotter, J. Biomed. Environ. Mass Spectrom. **13**, 395(1986).

8. C. J. McNeal, R. D. Macfarlane and E. L. Thurnston, Anal. Chem. **59**, 2036(1979).

9. G. Säve, P. Håkansson, B. U. R. Sundqvist, U. Jönsson, G. Olofson, M. Malmquist, Anal. Chem. **59**, 2059(1987).

10. W. Lange, D. Holtkamp, M. Jirikowsky, and A. Benninghoven, in "Ion Formation from Organic Solids", A. Benninghoven(Ed.), Springer Series in Chemical Physics, 25, Springer-Verlag, p.124, 1983.

11. B. U. R. Sundqvist, in "Sputtering by Particle Bombardment III", R. Behrisch and K. Wittmack (Eds.), Topics in applied physics volume 64, Spring-Verlag, p.257,1991.

12. E. A. Jordan, R. D. Macfarlane, C. R. Martin, C. J. McNeal, Int. J. Mass Spectrom. Ion. Phys. **53**, 345(1983).

13. R. D. Macfarlane, J. Trace, Micropr. Techn. **2**, 267(1984).

14. G. Jonsson, P. Håkansson, B. U. R. Sundqvist, P. Roepstorff, P. Carlsen, K. E. Johansson, I. Kamensky, M. Lindberg, Anal. Chem. **58**, 1084(1986).

15. D. Holtkamp, M. Kempken, P. Klüsener, and A. Benninghoven, J. Vac. Sci. Technol. **A5**, 2912(1987).

16.W. Lange, M. Jirikowsky and A. Benninghoven, Surf. Sci. **136**, 419(1984).

17. K. D. Cook, D. J. Todd, D. H. Friar, Biomed. Mass Spectrom. **18**, 492(1989).

18. O. Becker, S. Della-Negra, Y. LeBeyec, and K. Wien, Nucl. Instrum. and Meth. **B16**, 321(1986).

19. M. Salehpour, J. E. Hunt, D. L. Fishel and J. C. Tou, Int. J. Mass Spectrom. and Ion Processes **88**, 211(1989).

20. P. Håkansson, and B. U. R. Sundqvist, Rad. Eff. **61**, 179(1982).

21. A. Albers, K. Wien, P. Dück, W. Trea, H. Voit, Nucl. Instrum. and Meth. **198**, 69(1982).

22. J. E. Hunt, M. Salehpour, D. L. Fishel, and J. C. Tou, J. De physique (Paris), **C2**, 27(1989).

23. D. Brandl, Ch. Schoppmann, R. Schmidt, B. Nees, A. Ostrowski and H. Voit, Phys. Rev. **B43**, 5253(1991).

24. P. Håkansson, I. Kamensky, M. Salehpour, B. sundqvist, and S. Widdiyasekerra, Radiation Effects **80**, 141(1984).

24a. C.V. Barros Leite, E. F. da Silveira, J. M. F. Jeronymo, R. R. Pinho, G. B. Baptista, E. A. schweikert, and M. A. Park, Phys. Rev. **B45**, 12218(1992).

25. E. W. Ens, Ph.D. Thesis, University of Monitoba, Canada, Chapter 5, 1984.

26. M. C. Blain, S. Della-Negra, H. Joret, Y. LeBeyec, and E. A. Schweikert, Phys. Rev. Lett. **63**, 15, 1625(1989).

27. P. Sigmund, Phys. Rev. **184**, 383(1969).

28. D. F. Barofsky, E. Barofsky, in "Ion Formation from Organic Solids (IFOS III)", Springer Proceedings in Physics 9, Spring-Verlag, p.86, 1986.

29. D. F. Barofsky, L. F. Jiang, and T. Y. Yen, in "Methods and Mechanisms for Producing Ions for Large Molecules", K. G. Standing, and W. Ens (Eds.), Plenum Press, New York, p.101-115, 1990.

30. A. Hedin, P. Håkansson, M. Salehpour, and B. Sundqvist, Phys. Rev. **B35**, 7377(1987).

31. R. E. johnson, B. Sundqvist, A. Hedin, and D. Fenyö, Phys. Rev. **B40**, 49(1989).

32. S. Della-Negra, J. Depauw, H. Joret, Y. LeBeyec, I. S. Bitensky, G. Bolbach, R. Galera, and K. Wien, Nucl. Instrum. and Meth. **B52**, 121(1990).

33. A. Brunelle, S. Della-Negra, J. Depauw, Y. LeBeyec, and K. Wien, Nucl. Instrum. and Meth. **B43**, 484(1989).

34. S. S. Johar, and D. A. Thompson, Surf. Sci. **90**, 319(1979).

35. M. Salehpour, D. L. Fishel, and J. E. Hunt, Phys. Rev. **B38**, 12320(1988).

36. E. A. Schweikert, M. G. Blain, M. A. Park, and E. F. DaSilveira, Nucl. Instrum. and Meth. **B50**, 307(1990).

37. A. Brunelle, M. Benguerba, S. Della-Negra, J. Depauw, H. Joret, Y. LeBeyec, P. Sunraud, G. BenAssayag, M. Blain, and E. A. Schweikert, the 38th ASMS Conference on Mass Spectrom. and Allied Topics, 1990, p.447.

38. S. Della-Negra, Y. LeBeyec, B. Monart, K. Standing, and K. Wien, Nucl. Instrum. and Meth. **B32**, 360(1988).

39. K. M. Gibbs, W. L. Brown, and R. E. Johnson, Phys. Rev. **B38**, 11001(1988).

40. A. Eicke, and A. Benninghoven, in "Ion Formation from Organic Solids (IFOS III)", spinger Proceedings in Physics 9, A. Benninghoven (Ed.), Springer-Verlag, 1986, p.56.

41. A. Eicke, and A. Benninghoven, in "Secondary Ion Mass Spectrometry (SIMS VI)", A. Benninghoven, A. M. Huber, and H. W. Werner (Eds.) John Wiley & Son, 1988, p.675.

42. P. Roepstorff, P. F. nielsen, B. Sundqvist, P. Håkansson, and G. Jonsson, Int. J. Mass Spectrom. and Ion Processes **78**, 229(1987).

43. D. van Leyen, D. Greifendorf, A. Benninghoven, in "Secondary Ion Mass Spectrometry (SIMS VI)", A. Benninghoven, A. M. Huber, and H. W. Werner (Eds.), John Wiley & Son, 1988, p.679. 44. P. Sigmund, in "Inelastic Ion-Surface Collision", N. H. Tolk, J. C. Tully, W. Heiland, and C. W. White (Eds.), Academic Press, Inc., 1977, p.121.

45. R. Schmit, Ch Schoppman, D. Brandl, A. Ostrowski, H. Voit, D. Johannsmann, and W. Knoll, Phys. Rev. **B44**, 560(1991).

46. C. Fenselau, and R. J. Cotter, Chem. Rev. **87**, 501(1987).

47. A. Benninghoven, in "Ion Formation from Organic Solids (IFOS II)", A. Benninghoven (Ed.), Springer Series in Chemical Physics 25, 1983, p.64.

48. W. V. Ligon and S. B. Dorn, Fresenius Z Anal. Chem. **325**, 626(1986).

49. J. Lindhard: "Thomas-Fermi Approach and Similarity in Atomic Collisions", NAS-NRC publ. 1133, 1(1964).

50. J. Lindhard, Vibeke Nielsen, and M. Scharff, Det Kongelige Danske Videnskabernes Selskab Matematisk-fysiske Meddelelser **36**, 10(1968).

51. W. D. Wilson, L. G. Haggmark, and J. P. Biersack, Phys, Rev. **B15**, 2458(1977).

52. J. F. Ziegler, in "Ion Implantation: Science and Technology", J. F. Ziegler (Ed.), Academic Press Inc., 1984, p.51.

53. for example: E. A. Desloge, in "Classical Mechanics" V2, John Wiley & Son, 1982, Chapter 60.

54. J. F. Ziegler, in "Handbook of Stopping Cross-Section for Energetic Ions in all Elements", V5, Pregamono Press, 1980.

55. J. Lindhard, and M. Scharff, Phys. Rev. **124**, 128(1961).

56. W. H. Bragg and R. Kleeman, Philos. Mag. **10**, 318(1905).

57. D. I. Thwaites, Nucl. Instrum. and Meth. in Phys. Research, **B27**, 293(1987).

58. F. Hillenkamp, in "Ion Formation from Organic Solids (IFOS II)", A. Benninghoven (Ed.), Springer Series in Chemical Physics 25, 1983, p.190.

59. R. E. Johnson, Int. J. Mass Spectrom. Ion Processes **78**, 357(1987).

60. R. E. Johnson, and B. Sundqvist, Int. J. Mass Spectrom. Ion Processes **53**, 337(1983).

61. P. K. Haff, Appl. Phys. Lett. **29**, 473(1976).

62. P. Williams and B. Sundqvist, Phys. Rev. Lett. **58**, 1031(1987).

63. P. Sigmund, Nucl. Instrum. Meth. **B27**, 1(1987).

64. D. A. Thompson, Radiat. Eff. **56**, 105(1981).

65. Y. Kitazoe, N. Hiraoka, and Y. Yamamura, Surf. Sci. **111**, 381(1981).

66. I. S. Bitensky and E. S. Parilis, Nucl. Instrum. Meth. **B21**, 26(1987).

67. G. H. Vineyard, Radiat. Eff. **29**, 245(1976).

68. R. Kelly, Surf. Sci. **90**, 280(1979).

69. R. E. Johnson, and R. Evatt, Radiat. Eff. **52**, 187(1981).

70. P. Sigmund, and C. Claussen, J. Appl. Phys. **52**, 990(1981).

71. FEI Company, 19500 N.W. Gibbs Drive Suite 100, Beaverton, OR 97006-6907, Tel: (503) 690-1500.

72. All the liquid metal ion gun emitters are made by Mrs. E. Barofsky, Department of Agricultural Chemistry, Oregon State University, Corvallis, OR 97331-6502, Tel: (503) 737-1770.

73. Colutron Research Corporation, 2321 Yarmouth Ave. Boulder, CO. 80301, Tel: (303) 443-5211.

74. X. Tang, R. Beavis, W. Ens, R. Lafortune, B. Schueler, and K. G. Standing, Int. J. Mass Spectrom. Ion Processes **85**, 43(1988).

75. D. F. Barofsky, L. F. Jiang, and T. Y. Yen, in "Ion Formation from Organic Solids (IFOS V)", A. Hedin, B. Sundqvist, and A. Benninghoven (Ed.), John Wiley & Son, 1990, p.87.

76. A. Benninghoven, J. Vac. Sci. Technol. **3**, 451(1985).

77. M. Salehpour, P. Håkansson, and B. Sundqvist, Nucl. Instrum. Meth. **B2**, 752(1984).

78. Joseph Ladislas Wiza, Nucl. Instrum. Meth. **162**, 587(1979).

79. B. J. Beuhler, and L. Friedman, Nucl. Instrum. Meth. **170**, 309(1980).

80. Dr. E. W. Ens, Physics Department, University of Manitoba, Winnipeg, Man. R3T2N2, Canada.

81. O. B. Firsov, Sov. Phys.-JETP **5**, 1192(1957); **7**, 308(1958).

82. P. Loftager, F. Besenbacher, O. S. Jensen, and V. S. Sørensen, Phys. Rev. **A20**, 1443(1979).

83. W. V. Ligon and S. B. Dorn, Int. J. Mass Spectrom. Ion Processes **63**, 315(1985).

84. W. V. Ligon and S. B. Dorn, Int. J. Mass Spectrom. Ion Processes **68**, 337(1986).

85. W. V. Ligon, in " Biological Mass Spectrometry ", A. L. Burlingame and J. A. McCloskey (Eds.), p61-75, 1990, Elsevier Science Publishers B. V., Amsterdam.

86. P .Dück, Ph.D. thesis, University Erlangen-Nürnberg, German, 1981.

87. V. I. Shulga, and P. Sigmund, Nucl. Instrum. Meth. **B47**, 236(1990).

88. Y. Yamamura, Nucl. Instrum. Meth. **B33,** 493(1988).

89. P. Sigmund, J. De Physique **C2**, 175(1989).

90. R. R. Lucchese, J. Chem. Phys. **86**, 443(1987).

91. J. G. Pavlovich, Ph.D. Thesis, (in preparation) Oregon State University.

92. M. Benguerba, A. Brunelle, S. Della-Negra, J. Depauw, H. Joret, Y. LeBeyec, M. G. Blain, E.A. Schweikert, G. BenAssayag and P. Sudraud, Nucl. Instrum. and Meth. **B62**, 8 (1991).

APPENDIX

Vita

Ten-Yang Yen was born in Taipei, Taiwan on September 10, 1958. He began college studies at Fu Jen Catholic University, Taipei, Taiwan in 1978 and graduated in 1982 with a B.S. degree in physics. Before graduate studies, he served two years military obligation as a Second Lieutenant Army Reserve Officer in Taiwan. After military service, he worked as a research assistant in the Institute of Physics, Academia Sinica, Taiwan from 1984 to 1986.

The author started graduate school at Oregon State University, Corvallis, Oregon in September 1986. He began work with Dr. Douglas Barofsky in 1987 and began on his research of this thesis in 1988. In October 1992, author defended his dissertation.

The author has accepted a post-doctoral position (to begin October 21, 1992) in Department of Environmental Sciences and Engineering, University of North Carolina, Chapel Hill, North Carolina.